

3-18-2019

# Infrared Laser Ablation for Biomolecule Sampling

Kelin Wang

Louisiana State University and Agricultural and Mechanical College, kelin.wang641@gmail.com

Follow this and additional works at: [https://digitalcommons.lsu.edu/gradschool\\_dissertations](https://digitalcommons.lsu.edu/gradschool_dissertations)



Part of the [Analytical Chemistry Commons](#)

---

## Recommended Citation

Wang, Kelin, "Infrared Laser Ablation for Biomolecule Sampling" (2019). *LSU Doctoral Dissertations*. 4876.  
[https://digitalcommons.lsu.edu/gradschool\\_dissertations/4876](https://digitalcommons.lsu.edu/gradschool_dissertations/4876)

This Dissertation is brought to you for free and open access by the Graduate School at LSU Digital Commons. It has been accepted for inclusion in LSU Doctoral Dissertations by an authorized graduate school editor of LSU Digital Commons. For more information, please contact [gradetd@lsu.edu](mailto:gradetd@lsu.edu).

# INFRARED LASER ABLATION FOR BIOMOLECULE SAMPLING

A Dissertation

Submitted to the Graduate Faculty of the  
Louisiana State University and  
Agricultural and Mechanical College  
in partial fulfillment of the  
requirements for the degree of  
Doctor of Philosophy

in

The Department of Chemistry

by

Kelin Wang

B.S., Liaoning University of Petroleum and Chemical Technology, 2009

M.S., Western Kentucky University, 2012

May 2019

*To my loving parents*

## ACKNOWLEDGEMENTS

The most important person I must thank first is my major advisor, Dr. Kermit K. Murray, my committee chair, major advisor and doctoral mentor, for his wisdom, caring, and support during this endeavor. The constant encouragement he awarded me to build up confidence in myself and independent thinking skills on research problems. His sharp mind usually helps me through obstacles and hard time. It is impossible for me to finish this dissertation without his unwavering guidance and persistent help.

I greatly appreciate the remaining members of my committee, Dr. Megan A. Macnaughtan and Dr. John A. Pojman for the time and valuable advice they provided generously and also for the good questions which incited me to widen my research from various perspective.

Thanks to Dr. Fabrizio Donnarumma for valuable insights and help on biomolecular analysis, without which this work would be lacking and for which I am deeply thankful. Thanks to Dr. Scott W. Herke for the countless time assisting of genomic analysis.

I would also like to express my gratitude to all the faculty and staff in LSU chemistry department, especially to Ms. Connie David and Dr. Jeonghoon Lee from LSU mass spectrometry facility, as well as Dr. Clayton Loehn from LSU shared instrument facility.

Acknowledgements are also given to my colleagues, Fan Cao, Bijay Banstola, Chao Dong, Remi Lawal, Deenamulla Kankanamalage Achala Priyadarashani and Jamira Stephenson. Thanks for their assistance and help in my research work.

Special thanks to Dr. Boliang Zhang, for all the precious encouragement and help during hard times, as well as all the good memories and happiness during these five years.

This dissertation is dedicated to my parents and grandparents in China for their unconditional love and unbelievable support.

# TABLE OF CONTENTS

ACKNOWLEDGEMENTS .....	iii
LIST OF TABLES .....	vii
LIST OF FIGURES .....	viii
LIST OF ABBREVIATIONS AND SYMBOLS .....	xi
ABSTRACT .....	xiv
CHAPTER 1 INTRODUCTION.....	1
1.1. LOCALIZED SAMPLING METHODS.....	3
1.2. BIOMOLECULE ANALYSIS .....	11
1.3. OBJECTIVE.....	21
CHAPTER 2 INSTRUMENTATION.....	22
2.1. INFRARED OPTICAL PARAMETRIC OSCILLATOR LASER.....	23
2.2. IR LASER ABLATION AND TRANSFER.....	24
2.3. ABLATION CONTROL SOFTWARE.....	26
2.4. LASER ABLATION WORKFLOW .....	27
2.5 MALDI TOF/TOF MS.....	28
2.6 UPLC-HDMS <sup>E</sup> .....	28
2.7 SANGER SEQUENCING .....	28
2.8 BIOANALYZER .....	29
2.9 PCR .....	30
2.10 QUBIT.....	31
2.11 FLUORESCENCE READER.....	31
2.12 TISSUE SAMPLES PREPARATION.....	31
2.13 CHEMICAL AND MATERIALS .....	32
CHAPTER 3 MALDI DIRECTED LASER ABLATION TISSUE MICROSAMPLING WITH DIA MASS SPECTROMETRY .....	35
3.1. INTRODUCTION.....	35
3.2. EXPERIMENTAL .....	37
3.3. RESULTS AND DISCUSSION .....	39

3.4. SUMMARY .....	48
CHAPTER 4 INFRARED LASER ABLATION AND CAPTURE OF ENZYMES WITH CONSERVED ACTIVITY.....	50
4.1. INTRODUCTION.....	50
4.2. EXPERIMENTAL .....	53
4.3. RESULTS AND DISCUSSION .....	57
4.4. SUMMARY .....	63
CHAPTER 5 INFRARED LASER ABLATION SAMPLE TRANSFER OF TISSUE DNA FOR GENOMIC ANALYSIS .....	65
5.1. INTRODUCTION.....	66
5.2. EXPERIMENTAL .....	68
5.3. RESULTS AND DISCUSSION .....	69
5.4. SUMMARY .....	77
CHAPTER 6 RNA SAMPLING FROM TISSUE SECTIONS USING IR LASER ABLATION FOR QUANTITATIVE PCR .....	79
6.1. INTRODUCTION.....	79
6.2. EXPERIMENTAL .....	82
6.3. RESULTS.....	84
6.4. SUMMARY .....	91
CHAPTER 7: CONCLUSIONS AND FUTURE DIRECTIONS .....	93
REFERENCES .....	96
APPENDIX. LETTERS OF PERMISSION.....	123
VITA.....	125

## LIST OF TABLES

Table 2.1 Sources for laboratory supplies.....	34
Table 3.1 Summary of peptides and proteins identification in three tissue sections. ....	45
Table 3.2 Summary of all MALDI peaks assigned based on LC-MS/MS analysis of the laser ablated extracts including MW of the identified proteins, MW difference ( $\Delta M$ ) between MALDI peaks and MW of identified proteins, Uniprot accession number and protein names .....	46
Table 3.3 Full names of the proteins in Figure 3.5. ....	48
Table 5.1 Primer information. CYP11b2 indicates gene <i>Rattus norvegicus</i> hydroxysteroid 11-beta dehydrogenase 2 gene; Snn1g indicates gene amiloride-sensitive sodium channel subunit gamma gene. ....	69
Table 6.1 Primer information.....	84
Table 6.2 RNA recovery as a function of laser fluence .....	87

## LIST OF FIGURES

Figure 1.1 Schematic of an off-line liquid extraction system.....	4
Figure 1.2 Schematic of LMJ-SSP.....	5
Figure 1.3 Schematic of IR-LCM.....	7
Figure 1.4 Schematic of UV-LCM.....	8
Figure 1.5 Schematic of laser ablation.....	9
Figure 1.6 Schematic of MALDI.....	12
Figure 1.7 Schematic of ESI.....	14
Figure 1.8 Schematic of PCR.....	17
Figure 1.9 Schematic of qPCR.....	18
Figure 1.10 Schematic of Sanger sequencing.....	19
Figure 1.11 Schematic of NGS.....	20
Figure 2.1 Schematic of the laser ablation and transfer system: a) overview; b) detail of capture tube; c) tissue section after a single shot viewed from above the microcentrifuge tube. ....	25
Figure 2.2 Photograph of laser ablation (a) and capture system (b). ....	25
Figure 2.3 Screenshot of laser ablation control software.....	27
Figure 2.4 Sample electropherogram detailing the regions that are indicative of RNA quality...	30
Figure 3.1 Representative MALDI image of rat brain tissue sections showing the distribution of signals of (a) 8569, (b) 14,041, (c) 14,122, (d) 14,132, (e) 14,192, (f) 14,211, (g) 15,193, (h) 15,845, (i) 17,139, (j) 17,737, (k)18,401, (i) 21,912, (m) 22,902, and (n) 28,217 <i>m/z</i> .....	40
Figure 3.2 Contour maps obtained from MALDI MSI with color shade indicating the three levels: light shade is upper 80% quantile, mid-color intensity indicates mean, and dark indicates lower 80% quantile. ....	41
Figure 3.3 (a) Contour of MALDI MSI at 14,122 <i>m/z</i> ; (b) bright-field microscope image of laser ablated rat brain tissue. location 1, corpus callosum (7 mm <sup>2</sup> ); location 2, hypothalamus (4 mm <sup>2</sup> square).....	42
Figure 3.4 Representative UPLC-HDMSE mass spectra from analysis of an ROI 1 tissue section. a) MS of the MBP unique peptide YLATASTMDHAR; b) MS/MS spectrum of the triply charged peptide.....	43

Figure 3.5 KEGG pathway of Alzheimer's disease using proteins identified in (a) ROI 1 and (b) ROI 2 (c) ROI 1 and ROI 2.....	47
Figure 4.1 Calibration curve for the trypsin transfer efficiency test.....	54
Figure 4.2 Calibration curve for the catalase transfer efficiency test .....	55
Figure 4.3 Calibration curve for the trypsin activity test .....	55
Figure 4.4 Calibration curve for the catalase activity test .....	56
Figure 4.5 MALDI mass spectra of BSA tryptic peptides (red circles) obtained from (a) trypsin control and (b) laser ablation transferred trypsin.....	58
Figure 4.6 Transfer efficiency and activity of enzyme ablated at laser fluences of 10, 18, 26 kJ/m <sup>2</sup> : (a) enzyme transfer efficiency; (b) Enzyme activity. Dark gray indicates trypsin; light gray indicates catalase.....	60
Figure 4.7 (a) Bright-field microscope image of laser ablation sampled rat brain tissue (1) frontal cortex and (2) cerebellum and (b) catalase activity from a fluorescence assay frontal cortex (gray) and cerebellum (light gray) at 30 and 45 min.....	62
Figure 5.1 Segments of Sanger sequencing chromatograms of pGEM plasmid: a) 1 to 40 bp; b) 570 to 610 bp; c) 750 to 790 bp. Control indicates DNA without the laser ablation. Dark blue indicates QV < 20, blue indicates 20 < QV < 40 and light blue indicates QV > 40.....	71
Figure 5.2 Agarose gel electrophoresis image of digested DNA template samples obtained from three different laser fluences and control. All samples were double-digested into three fragments: 379 bp, 1150 bp and 1668 bp.....	72
Figure 5.3 Agarose gel image of PCR products from rat brain tissue sections. Four primers: a) CYP 11b2 (376 bp); b) Snn1g 1 (298 bp); c) Snn1g 3 (281 bp); d) Snn1g 2 (168 bp). Numbers 1-10 indicate samples; P indicates PCR Molecular Ruler; N indicates negative control. ....	74
Figure 5.4 DNA recovered with the Quick Universal Miniprep kit. Top insert is an image of the rat kidney section after laser ablation. Positions 16 to 20 were used for the multiple kit evaluation experiments.....	76
Figure 5.5 Agarose gel image of PCR products from rat kidney sections. Lane pairs 1-4 indicate samples. The left lane indicates sample without extraction and the right lane indicates sample with extraction. P indicates PCR Molecular Ruler; N indicates negative control. ....	77
Figure 6.1 Agilent Bioanalyzer electropherograms of purified human kidney total RNA comparing RNA integrity number (RIN) values for a positive control (a) with RNA collected by infrared laser ablation at five different fluences (b-f: 3, 5, 7, 9, & 11 kJ/m <sup>2</sup> ).....	85
Figure 6.2 Representative electropherograms of RNA from 20-mm <sup>2</sup> regions of paired consecutive 50 μm tissue sections. (a) Positive control (RIN 7.4±0.3): purified RNA was diluted ~15-fold. (b) Infrared laser ablation (RIN 6.8±0.3): purified RNA was diluted ~8-fold.....	89

Figure 6.3 Analysis by qPCR of RNA derived from two locations (a, insert): Location 1, two 4-mm<sup>2</sup> crescents; Location 2, 3-mm<sup>2</sup> circle. a – amplification curves; b – melt curves for two genes (MBP; GPDH). ..... 91

## LIST OF ABBREVIATIONS AND SYMBOLS

AD	Alzheimer's disease
BSA	Bovine serum albumin
cDNA	Complementary DNA
CHCA	$\alpha$ -cyano-4-hydroxycinnamic acid
CCD	Charge-coupled device
CID	Collision-induced dissociation
DDA	Data dependent acquisition
DNA	Deoxyribonucleic acid
DIA	Data independent acquisition
ddNTPs	Dideoxynucleotides
dNTPs	deoxyribonucleotide triphosphate
ECD	Electron capture dissociation
EI	Electron ionization
ESI	Electrospray ionization
ETD	Electron transfer dissociation
FTICR	Fourier transform ion cyclotron resonance

HPLC	High performance liquid chromatography
ICP	Inductively coupled plasma
IM	Ion mobility
IR	Infrared
ITO	Indium tin oxide
LCM	Laser capture microdissection
LMJ/SSP	Liquid micro-junction surface probe
MALDI	Matrix assisted laser desorption/ionization
MS	Mass spectrometry
MS/MS	Tandem mass spectrometry
MSI	Mass spectrometry imaging
MRI	Magnetic resonance imaging
NGS	Next generation sequencing
PAM	Parafilm assisted microdissection
PEN	Polyethylene naphthalate
PET	Polyethylene terephthalate
PET	Positron emission tomography

PCR	Polymerase chain reaction
RNA	Ribonucleic acid
RIN	RNA integrity number
ROI	Region of interest
qPCR	Quantitative PCR
SA	Sinapic acid
SDS	Sodium dodecyl sulfate
TOF	Time of flight
UPLC	Ultra performance liquid chromatography
UV	Ultraviolet

## ABSTRACT

In this research, an infrared laser at a wavelength of 3  $\mu\text{m}$  was used to ablate material from tissue sections for biomolecule analysis. Pulsed infrared (IR) irradiation of tissue with a focused laser beam efficiently removed biomolecules, such as proteins, enzymes, DNA, and RNA from tissue sections for further analysis. In a proteomics project, matrix-assisted laser desorption/ionization mass spectrometry imaging (MALDI-MSI) was used to determine regions of interest (ROI) for laser ablation. The matrix was then washed off. By overlaying the MSI generated heat-map, the section was sampled using IR laser ablation and custom stage-control software. Two ROI were selected and ablated from the same tissue section after MALDI-MSI. More than 700 proteins were identified in each region. A comparison of molecular localization and activity of identified proteins from two regions was performed. IR laser ablation was used to transfer enzymes while retaining their enzymatic activity. Three different laser fluences were used for ablating two enzymes: trypsin and catalase. Approximately 75% of the enzyme was transferred for all the fluences tested. According to fluorescence quantification, around 35% of the captured trypsin and 51% of the captured catalase were active after laser ablation. Regions were ablated and captured from frontal cortex and cerebellum of rat brain tissue sections and catalase activity was measured from the ablated material without further sample preparation. The catalase activity in the two regions was consistent with previously published data, demonstrating transfer of active enzymes from tissue. IR-laser ablation was used for sampling DNA and RNA. To test ablation transfer of large DNA, a 3200 base pair plasmid was used and evaluation of DNA quality after laser ablation was accomplished by comparing the sequencing performance of samples obtained from laser ablation and a control plasmid. Consistent results for intact DNA were obtained when

the laser fluence was below 24 kJ/m<sup>2</sup>. Regions 1 and 4 mm<sup>2</sup> square were ablated from rat brain and kidney tissue sections. Ablated material was amplified using polymerase chain reaction (PCR) with four primers from two genes. For RNA sampling, human kidney total RNA was used. The integrity of the RNA after laser ablation was monitored by gel electrophoresis. Low and high energy thresholds were determined, indicating the range in which intact RNA transfer could be achieved at the highest efficiency. Areas 2 mm<sup>2</sup> square were ablated from the rat brain tissue. After RNA purification and reverse transcription, mRNA was amplified and quantified using quantitative PCR with two genes.

## CHAPTER 1 INTRODUCTION

Identification and quantification of biomolecules, such as proteins, metabolites, DNA, and RNA in tissue is necessary for disease diagnosis, prognosis and drug development.<sup>1-6</sup> Biomolecule analysis generally starts with tissue homogenization and cell lysis. For example, tissue may be snap-frozen, pulverized into powder, and extracted with solvent targeting the biomolecule of interest.<sup>7</sup> Alternatively, tissue can be immersed in a lysis buffer and homogenized by vortexing or bead-beating and the biomolecules extracted and purified using in-house developed protocols or commercial extraction kits.<sup>8-10</sup> These methods are challenging due to a sampling mixture of both healthy and diseased cells, which leads to dilution of information from heterogeneous samples.<sup>11-12</sup> Homogenization of bulk tissue leads to loss of localization information from the heterogeneous microenvironment of biomolecules in tissue.<sup>13-16</sup>

Biological imaging methods, such as *in vivo* and *in vitro* techniques, can identify biomolecules while maintaining localization information.<sup>17-31</sup> *In vivo* imaging does not require dissection, but often provides limited chemical information. For example, X-ray scans use electromagnetic radiation to produce images of bones and dense material inside the body.<sup>18</sup> Magnetic resonance imaging (MRI) is based on sensitivity to the presence and properties of water in a magnetic field.<sup>21</sup> A positron emission tomography (PET) scan detects radioactive chemical injected into the blood.<sup>19</sup>

*In vitro* imaging is usually performed in tissue sections dissected from the organ of interest. Most *in vitro* imaging uses detection probes and requires prior knowledge of the targets to design the probes. These methods typically measure specific molecules such as proteins, DNA, or RNA,

thus limiting broad analysis.<sup>32</sup> For example, immunostaining can provide localization and relative concentration information for on order ten targets per tissue section, such as DNA and proteins.<sup>33</sup> An *in situ* hybridization of RNA usually can visualize fewer than ten transcripts simultaneously in the same tissue sample.<sup>34-35</sup> High throughput untargeted biomolecule imaging can be achieved by mass spectrometry imaging (MSI). MSI can analyze thousands of molecules, such as lipids, metabolites, peptides, and proteins in the same tissue section simultaneously.<sup>36-37</sup> However, detection of low and medium abundant species from tissue is challenging<sup>38</sup> and biological imaging is typically semi-quantitative rather than quantitative.<sup>39</sup>

Localized biomolecule analysis can be achieved after sampling populations of targets cells from tissue sections using various localized sampling methods. The sampling of material allows further processing prior to analysis, such as separation, purification, and digestion. The collected material is ready for proteomics, lipidomic, metabolomic, and genomic analysis.<sup>40-41</sup> Localized sampling avoids loss of information from localized biomolecules in heterogeneous samples.

The goal of the research described in this dissertation is to develop methods to collect biomolecules from regions of interest (ROI) in tissue sections for analysis by various analysis techniques. The sampling method developed is based on infrared (IR) laser ablation and capture. In this chapter, localized sampling techniques are discussed, such as liquid extraction, manual microdissection, laser capture microdissection, and laser ablation. The biomolecule analysis methods mass spectrometry, gel electrophoresis, polymerase chain reaction, and genomic sequencing, and the coupling of localized sampling with these methods is also discussed.

## 1.1. LOCALIZED SAMPLING METHODS

### Liquid Surface Extraction

Liquid surface extraction indicates techniques where a solvent is delivered to the surface of a tissue section. The solvent can be manually deposited with a micropipette or capillary or with an automated system. The extraction process requires different volumes of solvent and extraction time depending on the analyte of interest. The solvent can either be deposited on the surface for the desired amount of time or it can be continuously delivered and removed. In the first case, once the extraction is complete the solvent and extracted material is collected for off-line analysis.<sup>42</sup> In the second case, continuous delivery allows on-line analysis of the extracted material.<sup>43-44</sup> Liquid surface extraction has been used to extract proteins, lipids, and drugs from tissue sections for analysis.<sup>45-47</sup>

A schematic of a typical off-line system is shown in Figure 1.1. The extraction solvent can be delivered using a pipette or automated system. A volume of several  $\mu\text{l}$  extraction solution is placed on the tissue surface. After extraction on the tissue section for several seconds, the droplet is pipetted in and out of the tip several times. The pipette tip is in contact with the tissue surface during the extraction process.<sup>42</sup> Off-line collection can also be performed by automated systems such as a robotic actuator with appropriate pipette tips.<sup>45, 47-50</sup> The robotic arm picks up a pipette tip and moves it to a 96-well plate containing the extraction solvent. Extraction buffer is loaded into the pipette tip. The arm then moves the tip to the tissue surface. Less than 1  $\mu\text{l}$  extraction solvent is dispensed on the tissue. After extraction, the solution is aspirated back into the tip and it is ready for biomolecule analysis. Low volumes ( $<1 \mu\text{l}$ ) of extraction solvent are used in the automated system, which leads to smaller extraction spots (0.5 mm in diameter) than that from

manual disposition (1-2 mm in diameter).<sup>47</sup> Automated systems are able to keep the liquid on the tissue surface as long as 30 s, which may lead to more efficient extraction.<sup>47</sup> Using this technique, hundreds of unknown proteins can be identified in tissue sections.<sup>51</sup>

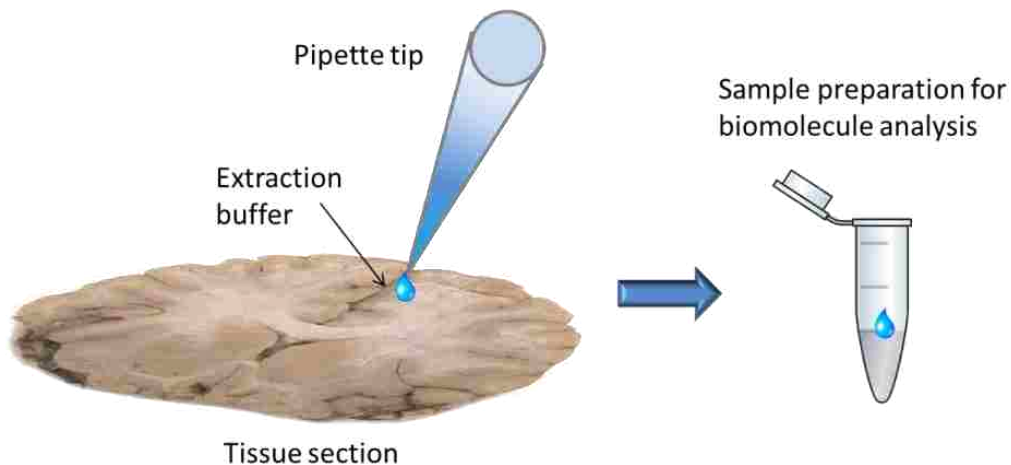


Figure 1.1 Schematic of an off-line liquid extraction system

Liquid surface extraction also can be performed on-line.<sup>43, 52</sup> In this case, the extraction solvent is continuously delivered and the solvent and extracted material removed. Figure 1.2 shows a schematic of a liquid micro-junction surface sampling probe (LMJ-SSP).<sup>46, 53</sup> The LMJ-SSP has two coaxial tubes with the extraction solvent is delivered to the tissue through the coaxial tubes and forms a micro-junction between the probe and sample surface. Continuously, the extraction solvent with samples is removed through the inner tube and delivered to the downstream instrumentation for analysis. The sampling spot size of LMJ-SSP is approximately 0.6 mm.

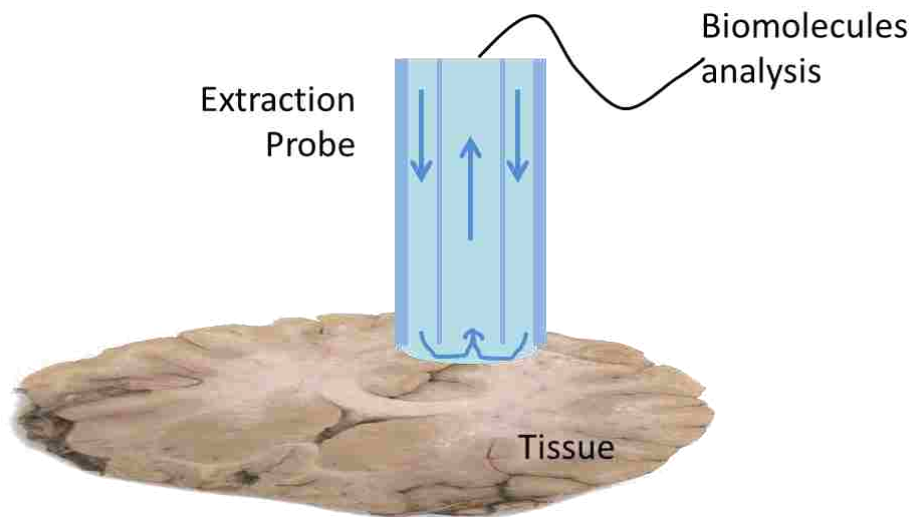


Figure 1.2 Schematic of LMJ-SSP

### Manual Microdissection

Manual microdissection is the extraction of tissue material using a needle or a scalpel under an optical microscope.<sup>54</sup> A thin plastic film such as Parafilm can be used to assist the cutting and selection of the tissue pieces.<sup>55</sup>

Manual microdissection is often guided by a defined shape or an ROI determined by pathology or histology using immunochemistry imaging under a stereomicroscope.<sup>54</sup> Manual microdissection can be performed with a sharp implement, such as an injection needle.<sup>56</sup>

Recently, an automated manual microdissection system was developed which included a camera to guide the dissection process.<sup>57</sup> The cutting device comprises a blade and a pressure controller, which allows precise cutting of the tissue. Extraction solvent is supplied at the blade-tissue interface and aspirated to collect the material for analysis.<sup>58</sup>

Parafilm assisted microdissection (PAM) was developed to improve the efficiency of manual microdissection.<sup>55</sup> PAM employs a Parafilm layer deposited on a microscope slide before mounting the tissue section. The Parafilm serves as a support to prevent the tissue from contacting the glass surface, which facilitates removal of the tissue sections after cutting.<sup>55, 59-60</sup> A grid with 1 mm squares is used as guide to locate ROI and assist microdissection.<sup>61</sup> PAM was used to collect material from benign and tumor regions of tissue sections and proteins were identified in these regions.<sup>60</sup>

For many biomolecule analysis methods, sufficiently pure populations of cells can be provided by manual microdissection;<sup>54-55, 59-60, 62-63</sup> In a study comparing liquid extraction to manual microdissection, 2-5 times more proteins were identified in the latter.<sup>64</sup> However, the technique is labor intensive and often has limited reproducibility.<sup>54, 62</sup>

### **Laser Capture Microdissection**

Laser capture microdissection (LCM) is a method for small-scale tissue sampling for extraction of homogeneous cell populations from tissue samples.<sup>65-70</sup> The first LCM technique to be developed uses an infrared laser and thermoplastic to select tissue regions.<sup>71</sup> The tissue section on a microscope slide is covered by a plastic cap with a thin thermoplastic film (Figure 1.3a & b). An IR laser is focused on the film to melt and fuse with the tissue in selected regions. The melted film adheres to the tissue (Figure 1.3c). When the cap is removed from the tissue section, the selected region is peeled off with it, as shown in Figure 1.3d.

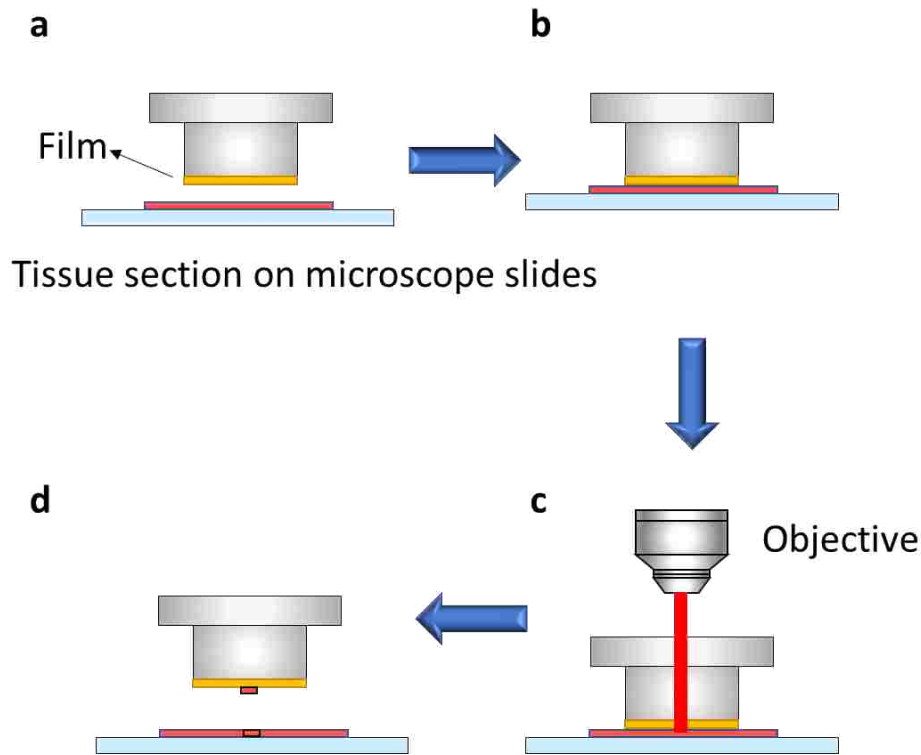


Figure 1.3 Schematic of IR-LCM

The second LCM technique to be developed uses a highly focused UV laser (UV-LCM) to cut the boundary of a tissue region. The laser beam irradiates the back of the microscope slide in transmission geometry mode. In one UV-LCM configuration, the sample faces upwards with which allows cutting and subsequent catapulting of the sample into a collector cap, which may contain a liquid or an adhesive substrate (Figure 1.4a).<sup>72</sup> Alternatively, the tissue can face downwards with the laser irradiating from the top (Figure 1.4b), which allows gravity to help detach the microdissected ROI.<sup>73</sup> In either case, detachment can be accomplished by irradiating the tissue with an unfocused beam, which produces a force that may free the cut region (laser pressure catapulting).<sup>74</sup> UV-LCM requires the tissue to be mounted on polyethylene naphthalate (PEN) or polyethylene terephthalate (PET) membrane microscope slides with tissue thickness below 15  $\mu\text{m}$ .<sup>75-82</sup>

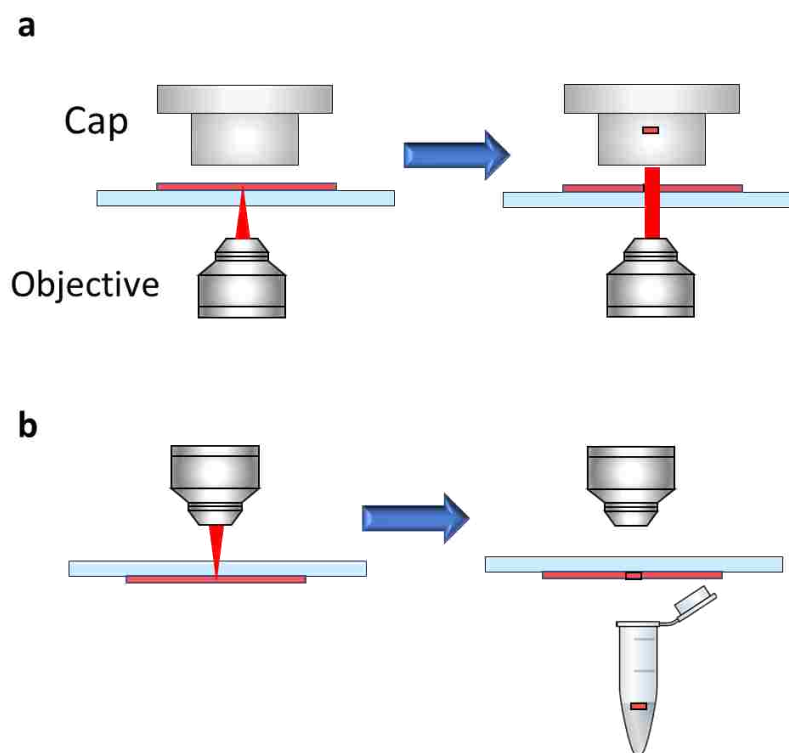


Figure 1.4 Schematic of UV-LCM

Both IR- and UV-LCM have been widely used to collect material from tissue sections for protein and metabolite identification and quantification and for genomic sequencing and expression.<sup>83-86</sup> LCM has a spatial resolution of hundreds nanometers range and can extract as little as a few cells from a tissue section.<sup>67, 87-88</sup> It is thus possible to perform analysis on single cells.<sup>67</sup>

Sampling time for LCM varies from 20 minutes to one hour, depending on the number of cells, tissue type, and type of microscope slide used.<sup>41, 67, 89-90</sup> A common difficulty is the inability to completely remove the selected cells from the tissue section<sup>91</sup> which may result from improper slides<sup>75</sup> or incomplete dehydration.<sup>77</sup> LCM dissected material often requires cell lysing for subsequent analysis.<sup>41, 67, 89-90</sup>

## Laser Ablation

Laser ablation is a laser micro-sampling technique which uses a pulsed UV,<sup>92-93</sup> visible,<sup>94</sup> or IR<sup>95-102</sup> laser to irradiate the regions of tissue section in transmission (Figure 1.5a)<sup>41</sup> or reflection geometry (Figure 1.5b),<sup>96</sup> which can be used to remove the material for on-line and off-line biomolecule analysis. Here, the ROI are converted to small particles that are ejected from the slide into a plume directly into a capture system or analysis system.

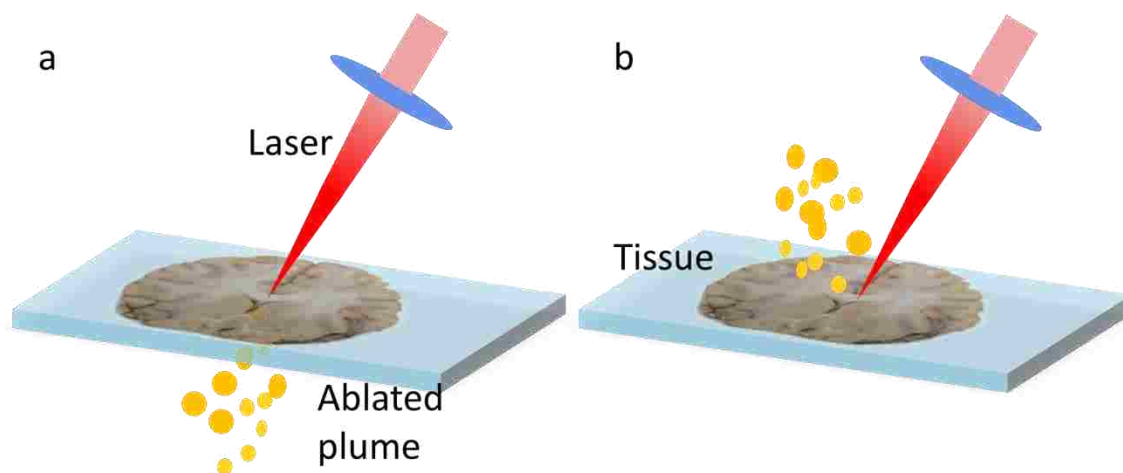


Figure 1.5 Schematic of laser ablation

Laser ablated material can be captured in a liquid droplet,<sup>97</sup> a flowing liquid bridge,<sup>101</sup> micro-junction,<sup>94</sup> liquid vortex,<sup>103</sup> filter,<sup>96</sup> or centrifuge tube with buffer solution.<sup>41</sup> Laser ablation systems can be used for either off-line or on-line analysis.

Liquid droplet capture is achieved by suspending a solvent droplet from a capillary and suspending it above the laser ablation plume. By applying an electric field between the sample and the collection droplet, the transfer efficiency of droplet capture can be as high as 50%.<sup>97</sup> The transfer efficiency of droplet capture also can be improved by aspiration, or a potential applied to the inlet of the capillary.<sup>104-105</sup>

A flowing liquid bridge can be used as a capture device,<sup>100-101, 106</sup> which can be constructed using two capillaries with narrow gap,<sup>100-101</sup> and allows on-line continuous analysis. The transfer efficiency can be 20% by applying high voltage to the capillary.<sup>106</sup>

Both liquid micro-junction capture<sup>94, 107-108</sup> and vortex sampling<sup>93, 103</sup> allow continuous on-line biomolecule analysis, which uses a LMJ-SSP probe (Figure 1.2). A wall-less liquid micro-junction is formed between the sampling end of the probe and the tissue/sample surface. Vortex sampling employs a stable vortex, or whirlpool at the sampling end of the LMJ-SSP probe to capture laser-ablated material into the inner tube. For micro-junction sampling, the laser is directed from the bottom of the sample, and the probes are used to collect ablated material from the top; whereas for vortex sampling, the laser is directed at the top of the samples, and the probes are used to collect ablated material from the bottom. The vortex sampling also uses gravity and swirling vortex to assist capturing. The reported transfer efficiency is 24%, which is double the liquid micro-junction capture efficiency.<sup>103</sup>

Laser ablation plumes also can be collected in a vacuum aspirated tube with filter.<sup>40, 96</sup> An open end of a tube with 0.2  $\mu$ l bed volume of C18 stationary phase material was mounted at the end of the tube and vacuum was applied to the other end of the tube. The transfer efficiency was  $11 \pm 8\%$  for peptides.<sup>96</sup> This technique was used to collect proteins from rat brain tissue sections.<sup>96</sup>

Unlike LCM, laser ablation does not require that tissue samples be mounted on membrane coated microscope slides.<sup>40-41</sup> Samples can be ablated using reflectron mode from different surfaces.<sup>40</sup> In addition, IR laser ablation does not require a separate cell lysis step.<sup>41</sup>

## 1.2. BIOMOLECULE ANALYSIS

Biomolecule analysis techniques refer to a set of methods, assays and procedures that enable identification and quantification of biomolecules such as proteins, lipids, metabolites, DNA, and RNA. Most of these techniques, such as mass spectrometry, fluorescence analysis, electrophoresis and genomic amplification and sequencing, can be used after localized sampling. In this section, the biomolecule analysis methods used in the subsequent chapters are described. The application of localized sampling for biomolecule analysis is discussed.

### Mass Spectrometry

Mass spectrometry (MS) is one of the most widely used techniques for identification and quantification of proteins, lipids, drugs, metabolites, and other biomolecules. In a typical MS procedure, molecules in a sample are ionized and sorted according to mass-to-charge ratio ( $m/z$ ) in mass analyzer. Finally, the ions are detected by the detector. Results are displayed as spectra of relative abundance of ions as a function of  $m/z$ . A variety of ion sources have been developed,<sup>109</sup> such as electron ionization (EI), inductively coupled plasma (ICP), matrix-assisted laser desorption/ionization (MALDI), and electrospray ionization (ESI).<sup>110-113</sup> MALDI and ESI are two widely used ionization methods for biomolecule analysis because they are capable of ionizing large biomolecules without fragmentation.<sup>110-113</sup>

There are many different mass analyzers, which employ electric and magnetic fields to separate ions. For example, a magnetic sector uses a magnetic field in a direction perpendicular to ion motion that causes the ions to travel in a circular path.<sup>114</sup> A time-of-flight (TOF) mass analyzer measures the time it takes ions with different masses but the same kinetic energy to move through a field-free region.<sup>115</sup> Trapped ion mass analyzers, such as the Paul trap, Orbitrap, or

Fourier-transform ion cyclotron resonance (FT-ICR) Penning trap, trap and separate ions by  $m/z$  using electric and magnetic fields.<sup>116-119</sup> Quadrupole mass analyzers are used as a mass filter in which ions with selected  $m/z$  can pass quadrupole rods with applied static and radio frequency potentials; quadrupole mass analyzers are often combined with other mass analyzers for ion separation.<sup>119</sup>

MALDI uses a laser to desorb and ionize compounds from a surface.<sup>120</sup> The matrix is typically a UV energy absorbing aromatic acid. A small quantity of sample and excess matrix is mixed and co-crystallized on a metal target for analysis. The matrix absorbs the pulsed laser energy which leads to desorption and ionization (Figure 1.6). MALDI allows analysis of proteins over 100,000 Da in mass.<sup>121</sup>

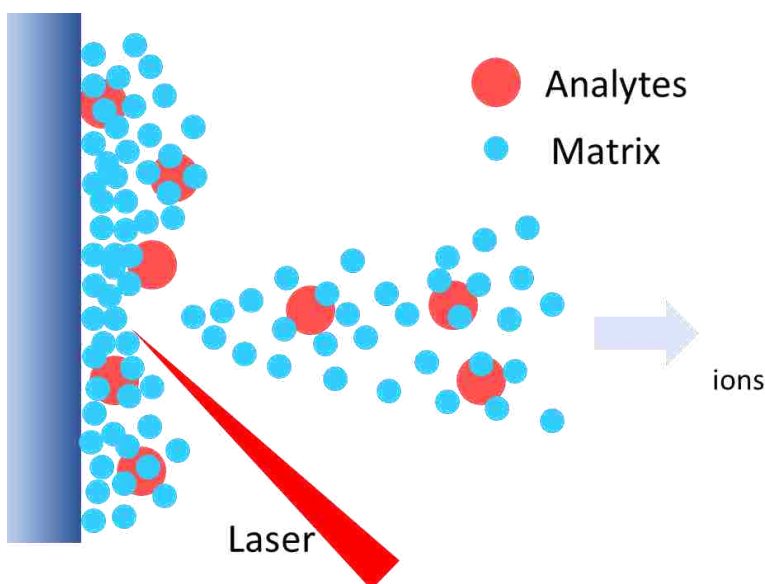


Figure 1.6 Schematic of MALDI

MALDI also can be used as an imaging technique<sup>122</sup> which shows the relative abundance of detected ions in the different location of the tissue section. The MALDI laser is raster scanned across the tissue from a regularly spaced array of positions. After that, a series of different mass

spectra are obtained from different positions of the tissue section. The molecular information of the selected  $m/z$  encoded at each location is extracted and plotted to create ion images that can be directly correlated with the location and amount of specific biological molecules. The result of a MALDI MSI experiment is represented as a 2-dimensional heat-map, where each pixel represented the signal intensity of a specific mass window extracted from all the spectra recorded. MALDI MSI allows imaging of tissue samples with a broad molecular weight range<sup>123</sup> with applications to analysis of drugs, metabolites, lipids, and proteins.<sup>36, 124-126</sup> In a MALDI MSI experiment, thin tissue section is mounted on a conductive microscope slide. MALDI matrix is sprayed on the surface of the tissue section prior to imaging. Although MALDI MSI can detect only most abundant ions and semi-quantitatively,<sup>127-128</sup> it can be used to localize ROI for localized sampling methods.<sup>55, 59, 129</sup>

ESI mass spectrometry for large molecule identification was developed in the late 1980s by Fenn and co-workers.<sup>130</sup> A solution in a narrow bore capillary or needle is raised to a few kilovolts potential. Highly charged droplets are ejected from capillary tip due to the high surface charge and the subsequent solvent evaporation results in highly charged molecules. Capillary heating and heated nitrogen gas flow assists desolvation. The multiply charged ions enter the mass spectrometer for  $m/z$  separation and detection (Figure 1.7). An advantage of ESI is the generation of multiple charged molecules, which enables analysis of large molecules in a mass spectrometer with limited  $m/z$  range.<sup>113</sup>

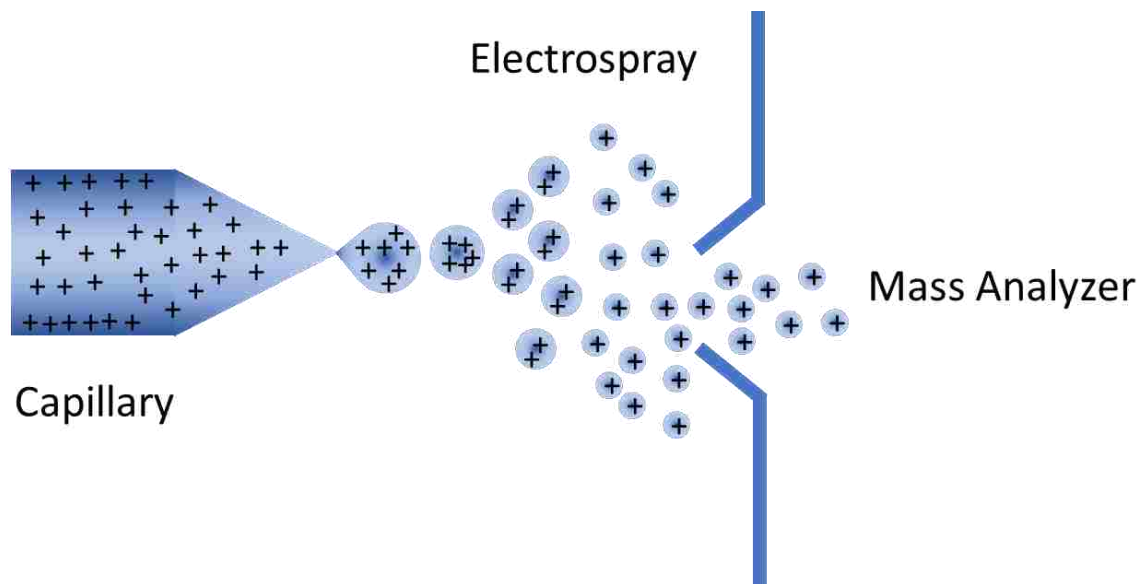


Figure 1.7 Schematic of ESI

Mass spectra (MS) only show the molecular weight of biomolecules. Tandem mass spectrometry (MS/MS) that involves multiple steps of mass spectrometry provides structural information of the analytes.<sup>131-132</sup> In tandem mass spectrometry, ions are first separated by  $m/z$  in the first stage of MS. Ions with certain  $m/z$  are selected and fragmented. Those fragments ions are then separated by  $m/z$  in the second stage of mass spectrometry. There are several fragmentation methods, such as collision-induced dissociation (CID), electron capture dissociation (ECD), and electron transfer dissociation (ETD).<sup>131</sup> Tissue samples usually contain a complex mixture of biomolecules. Separation systems, such as high-performance liquid chromatography mass spectrometry (HPLC-MS) and ion mobility (IM) mass spectrometry are able to improve biomolecule identification and quantification from tissue extracts.<sup>133-135</sup>

There are two main workflows for mass spectrometry-based proteomics: top-down and bottom-up.<sup>136-137</sup> In top-down proteomics, intact proteins are ionized and introduced into the mass spectrometer and fragmented, followed by mass measurement of the product ions. In bottom-up

proteomics, proteins are digested into peptides using proteolytic enzymes.<sup>137</sup> This can be done either before or after protein isolation. The peptides are identified and quantified using MS or MS/MS. The identified peptides are assigned to proteins through database searching.<sup>138</sup>

## **Gel Electrophoresis**

Gel electrophoresis is an analytical method that can be used for separation of DNA, RNA, proteins, and other biomolecules.<sup>139-143</sup> Gels can be made of agarose or polyacrylamide or starch. An electric potential is applied to the gel. DNA and RNA are negatively charged in solution and loaded onto the gel. The detergent SDS is mixed with proteins and applies a negative charge to each protein in proportion to its mass. Additionally, SDS is also able to denature proteins. The negatively charged and denatured proteins are loaded onto the negative end of the gel. The molecules travel through the gel at a speed that is inversely related to their size and molecular weight. Therefore, the smaller molecules travel a longer distance through the gel. After separation, the molecules with different sizes form distinct bands on the gel that can be used to determine the molecular weight and a standard ladder mixture with known molecular weights is loaded into the gel in a separate lane. The molecular weight of the samples is obtained by comparing their bands to the ladder.<sup>142</sup>

Gel electrophoresis can be used to identify proteins according to their molecular weight, but it can be challenging for analysis of larger proteins.<sup>144-145</sup> For genomic analysis, gel electrophoresis can be used to determine the integrity of DNA or RNA. In the case of DNA, samples are loaded into the gel along with positive control DNA. Assessing DNA integrity can be achieved by comparing the bands of the sample and intact DNA.<sup>146-147</sup> In the case of RNA, intact total RNA has intense bands due to the 28S and 18S ribosome RNA. A 2:1 ratio of 28S is a good

indication of intact RNA and a ratio lower than 2 indicates degradation,<sup>143, 148-149</sup> although this can be a highly variable metric.<sup>150-151</sup> The RNA integrity number (RIN) is an integrity criterion that takes into account the entire electrophoretic trace. RIN values can range from 1-10, with 1 indicating degraded RNA and 10 representing intact RNA.<sup>151</sup>

Gel electrophoresis is often used as a separation technique prior to mass spectrometry analysis: protein mixtures are separated by gel electrophoresis and proteins of interest are extracted from the gel bands.<sup>144-145</sup> However, many workflows use liquid chromatography to the exclusion of gel electrophoresis.<sup>152</sup>

### **Polymerase Chain Reaction**

Polymerase chain reaction (PCR) is used to amplify DNA.<sup>153-154</sup> PCR uses DNA primers which are short single strands of DNA (18-28 nucleotides) whose sequence matches a DNA template region. PCR uses cycles of heating and cooling and a heat-stable DNA polymerase for DNA replication (Figure 1.8). The DNA is heated to 94-98 °C, which causes the DNA strands to separate. This step is called denaturation. The temperature is cooled to 50-65 °C to enable the primers to anneal to the template DNA. After annealing, the temperature is raised to 72-80 °C and a new strand of DNA is created using free nucleotides and DNA polymerase enzymes. The procedure is repeated until the desired quantity of DNA is obtained.<sup>153</sup> The final products can be accessed by gel electrophoresis. By comparing with a DNA ladder, the size of the PCR products can be determined.

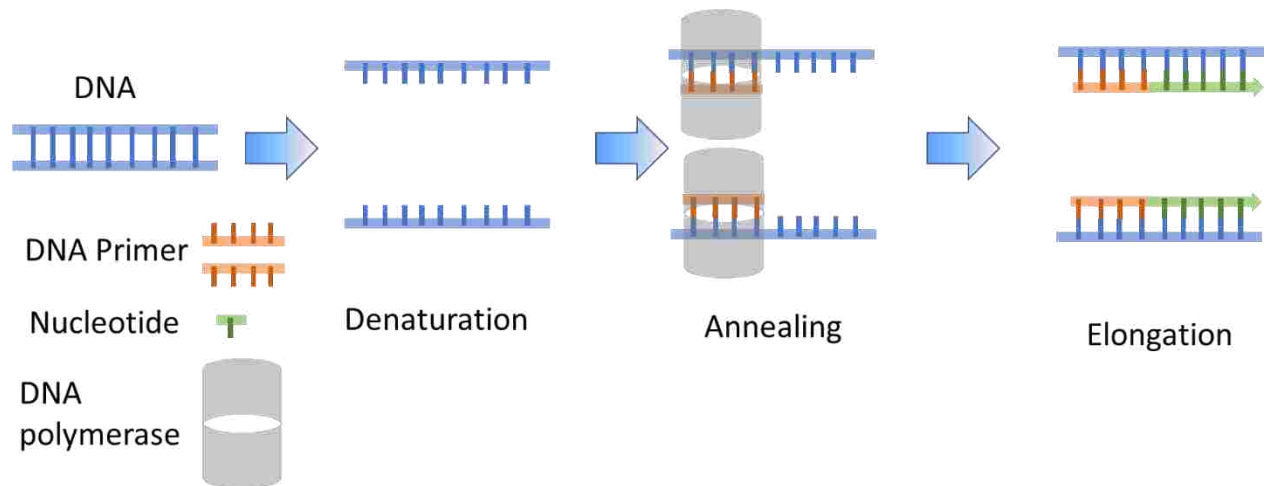


Figure 1.8 Schematic of PCR

Real-time PCR, also known as quantitative PCR (qPCR), is a technique based on PCR in which the amplification of targeted DNA is monitored during the process. Therefore, qPCR can be used to quantify DNA as well as RNA. However, RNA quantification requires reverse transcription to synthesize DNA from an mRNA template prior to quantification. The synthetic DNA is called complementary DNA (cDNA)<sup>155</sup> and can be amplified and quantified as DNA. The qPCR process uses thermal cycling and fluorescent labeling for quantification.<sup>156-159</sup> The free nucleotides do not fluoresce; fluorescence obtains on attachment to the DNA strand (Figure 1.9).<sup>160</sup> A qPCR experiment is displayed as plot of fluorescence signal as a function of amplification cycles. A cycle threshold (Ct) is the cycle number when fluorescence is detected, and a large Ct indicates a lower mRNA quantity for given number of cycles. In a qPCR experiment, reference genes are usually amplified and quantified with genes from the sample and the Ct number is normalized to the reference genes.

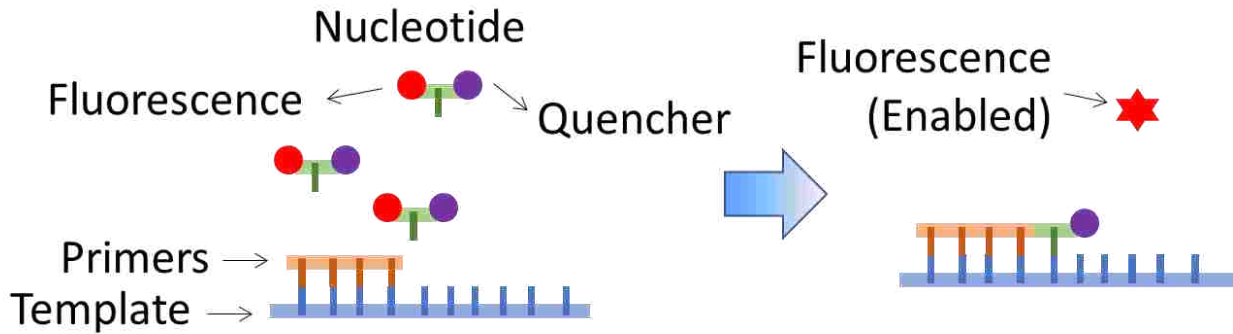


Figure 1.9 Schematic of qPCR

Sampling pure populations of cells is important for PCR analysis, because a few unwanted cells can produce interfering DNA after amplification.<sup>161</sup> For genomic analysis, PCR is usually used for amplification. For RNA transcriptomic comparison, gene expression analysis (mRNA quantification) requires separation of cell populations from healthy and diseased tissue. The quantity of mRNA can be compared and putative mRNA biomarkers can be identified.<sup>162</sup>

The quantity and integrity of RNA play a critical role in the accuracy and reproducibility of high throughput RNA analysis.<sup>163-171</sup> Manual microdissection and LCM have been used to sample tissue material for genomic analysis, but LCM has in general better precision and effectiveness. Rapid sampling of LCM increases the reproducibility due to variability of gene expression in small samples.<sup>67</sup> Protocols for qPCR from LCM samples have been reported<sup>75</sup> and high quality RNA has been obtained from LCM down to the single cell level.<sup>172-173</sup>

### Genomic Sequencing

Genomic sequencing is a process of determining the order of nucleotides in DNA or RNA.<sup>174-175</sup> There are two widely used sequencing methods: Sanger sequencing and next generation sequencing (NGS).<sup>176</sup> Sanger sequencing is a chain termination method.<sup>176</sup> In a typical

Sanger sequencing experiment (Figure 1.10), double stranded DNA to be sequenced is heated to separate it into single stranded DNA. A primer is annealed to the DNA region to be sequence. and DNA polymerase and modified chain terminating dideoxynucleotides (ddNTPs) are added. The four ddNTP (ddTTP, ddATP, ddGTP, ddCTP) lack hydroxyl groups, thus no further nucleotides can be added after them. In Fig. 10, blue indicates ddTTP; green indicates ddATP; yellow indicates ddGTP; and red indicates ddCTP. In each reaction, the dNTP is attached to the DNA by the polymerase and terminated when a ddNTP attaches. The DNA fragments are separated according to their lengths and the sequence is read from the fluorescence signal. Fluorescent ddNTP has also been used. In this case, each type of ddNTP has a different fluorescence tag; thus, only one reaction is needed.

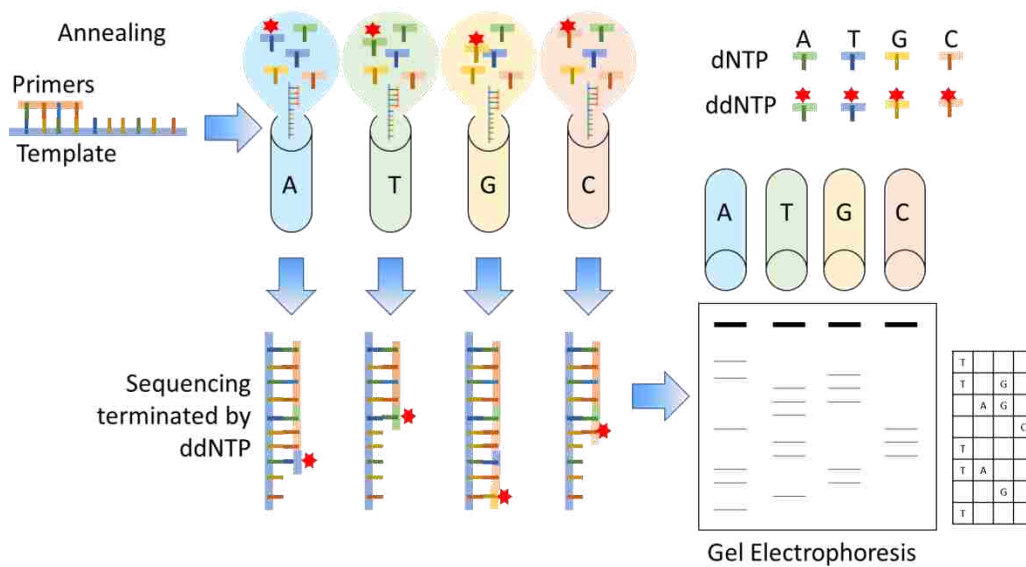


Figure 1.10 Schematic of Sanger sequencing

NGS platforms perform massively parallel sequencing, during which millions of DNA fragments are sequenced simultaneously.<sup>177-178</sup> Although there are many different NGS platforms, they all share some similar attributes (Figure 1.11).<sup>179-180</sup> The first step of NGS is library

preparation, where double stranded DNA is fragmented by an enzyme or sonication. Short, double stranded DNA adaptors are ligated to these DNA fragments. The second step is amplification, where the ligated DNA fragments are embedded on a micro-bead (emulsion PCR) or glass slide (bridge PCR), and the DNA fragments amplified by a polymerase-mediated reaction. The third step is sequencing, which varies for different platforms.<sup>181</sup> Accordingly, each NGS platform has specific biases and limitations and it is necessary to choose a platform appropriate for a specific applications.<sup>182</sup>

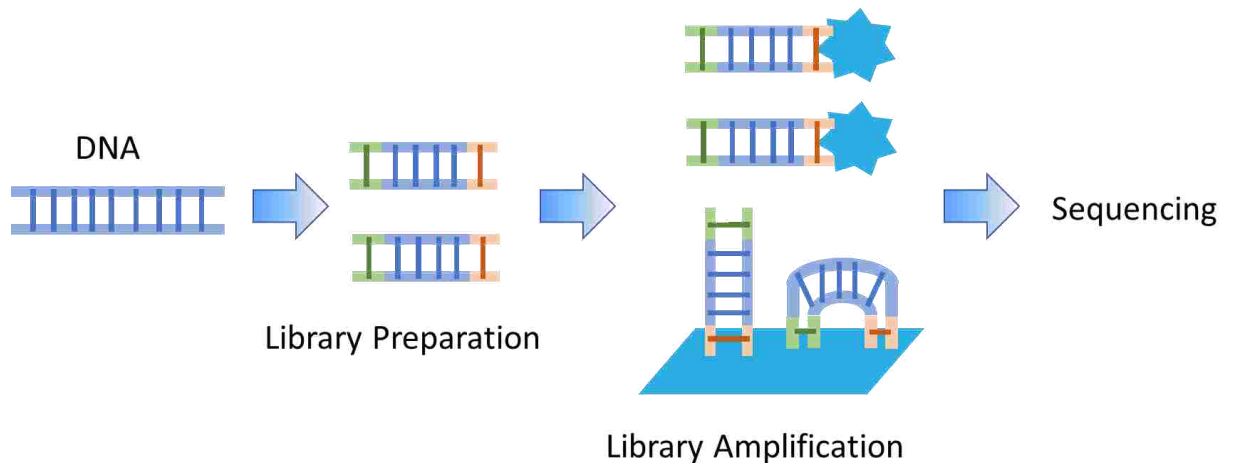


Figure 1.11 Schematic of NGS

Compared to Sanger sequencing, NGS is simpler and faster.<sup>175, 179</sup> NGS does not require knowledge of the DNA sequence. However, NGS has a shorter read length compared to Sanger sequencing, which results in higher average error rate.<sup>177, 183</sup> Even so, the combination of LCM and NGS can be used to determine the entire transcriptomes of specific tissues. For example, a protocol has been developed for transcriptomic profiling of human skin biopsies using LCM and NGS<sup>184</sup> and LCM was coupled with NGS for transcriptional profiles of brain tissue to study Alzheimer’s disease.<sup>185</sup>

### **1.3. OBJECTIVE**

The overall goal of this research was to develop an IR laser-based sampling technique for biomolecule analysis that is compatible with multiple analysis methods. The specific components of the project were to use infrared laser ablation sampling with 1) LC-MS/MS and MALDI MSI; 2) enzyme sampling; 3) DNA sequencing and PCR; and 4) RNA and qPCR. Details of the IR laser ablation system and analysis instrumentation are described in Chapter 2. The mass spectrometry study is described in Chapter 1, the enzyme in Chapter 4, the DNA study in Chapter 5, and the RNA study in Chapter 6.

## CHAPTER 2 INSTRUMENTATION

In the research described in this dissertation, IR laser ablation was used to transfer ROI from tissue sections. The wavelength was set at 2.94  $\mu\text{m}$  to overlap with the OH stretch absorption.<sup>186</sup> The laser was operated in a raster mode and ROI is converted to small particles.<sup>187-188</sup> The removal of material as particulate appears to protect fragile biomolecules from fragmentation allowing the capture of intact biomolecules.<sup>41</sup>

MALDI MSI was used for ROI selection. MALDI MSI allows imaging of tissue samples with an upper mass range limit of tens of thousands of Dalton<sup>123</sup> with applications for analysis of analytes including drugs, metabolites, lipids and proteins.<sup>36, 124-126</sup> HPLC-MS/MS was employed for proteomics analysis, providing protein identification and quantification high accuracy and reproducibility.<sup>189-191</sup> For genomic analysis, Sanger sequencing was used because it is inexpensive and has higher average error rate than next generation sequencing.<sup>177, 183</sup> Gel electrophoresis has been used to assess the integrity of DNA sampled using laser ablation.<sup>192-193</sup> The integrity of RNA obtained from manual microdissection or LCM can also be assessed using gel electrophoresis prior to further analysis.<sup>194-199</sup> In the work described in this chapter, microfluidic chip based electrophoresis was used to assess RNA integrity. Multiple regions from the electrophoretic trace were evaluated to determine an RNA integrity number (RIN). RIN values can range from 1-10, with 1 indicating highly degraded RNA and 10 representing fully intact RNA.<sup>151</sup> Quantitative PCR (qPCR) was used for mRNA quantification because qPCR is fast, sensitive, specific and easy to perform compared to other RNA quantification methods, such as northern blotting or in situ hybridization.<sup>200</sup>

This chapter contains a discussion of instruments used in this research. A detailed explanation of IR laser ablation is presented. System parameters for ablation and capture are provided.

## **2.1. INFRARED OPTICAL PARAMETRIC OSCILLATOR LASER**

A pulsed infrared optical parametric oscillator (OPO) was used in these studies as the pulsed light source for laser ablation. An OPO contains non-linear optical elements that shifts the photon energy of the input laser pulse.<sup>201</sup> A high intensity laser beam at a certain frequency is directed into a non-linear optical crystal in an optical cavity and split into two beams which are collinear with input beam. The sum of the photon energies from the two new generated beams is equal to the input beam energy. The wavelength of signal can be tuned by changing the temperature of the crystal, by applying an electrical field, or by changing the angle between crystals and the input beam (angle tuning). In this work, angle tuning was used.

In this research, an OPO from OPOTEK (Model 2731, Carlsbad, CA) was used. The wavelength of the pump laser used in this system is a 1,064 nm from a Nd:YAG laser. The non-linear crystal used in this system is potassium titanyl phosphate (KTP) and the laser wavelength can be tuned from 2.7 to 3.1  $\mu\text{m}$  by changing the crystal angle within the OPO cavity. The maximum laser repetition rate was 20 Hz with 7 ns pulse temporal width. The beam diameter is 3 mm and the beam divergence is 10 (H) x 2 (V) mrad. The maximum laser pulse energy is 2 mJ without any attenuation. Laser energy attenuation was performed either with the laser software or an external optical element. The laser energy was measured using an energy meter (Model Gentec, Markham, Ontario, Canada).

For all the experiments, the laser wavelength was set to 2.94  $\mu\text{m}$  to overlap the OH stretch absorption of water.<sup>202</sup> Proteins, which have OH and NH groups can also absorb at this wavelength.<sup>202</sup> Absorption at these wavelengths can produce ablation of proteins even in nominally dry samples.<sup>203</sup>

## **2.2. IR LASER ABLATION AND TRANSFER**

Transmission geometry, where the laser passes through the microscope slide and impinges on the tissue from underneath, was used in all the experiments in this research. Figure 2.1 shows a schematic of the laser ablation and transfer configuration and Figure 2.2 shows the photograph of the system. Samples for ablation were deposited or mounted on microscope slides that were attached to a two-axis translation stage (LTA-HS, Newport, Irvine, CA) with the samples facing downward. The laser was focused with a 50-mm focal length lens and directed through the microscope slide at a 45° angle. Visualization of samples was achieved with a video camera (DCC1645C, Thorlabs, Newton, NJ) mounted above the translation stages (Figure 2.1a). Samples were ablated into a 300  $\mu\text{l}$  microcentrifuge tube containing 200  $\mu\text{l}$  capture solution. Various capture solutions were used for the different analytes. The distance between the surface of the capture solution and the microscope slide was approximately 5 mm (Figure 2.1b). If the distance was less than 5 mm, the laser tended to ablate the capture solution and contaminate the slide. Figure 2.1c shows a tissue section above a capture tube that was irradiated by a single laser shot.

Before ablation, the laser was aligned with the center of the capture tube. The laser was stationary during laser ablation and the microscope slide was translated in a linear serpentine raster pattern with a 100  $\mu\text{m}$  line spacing. The speed of the stage was 1 mm/s.

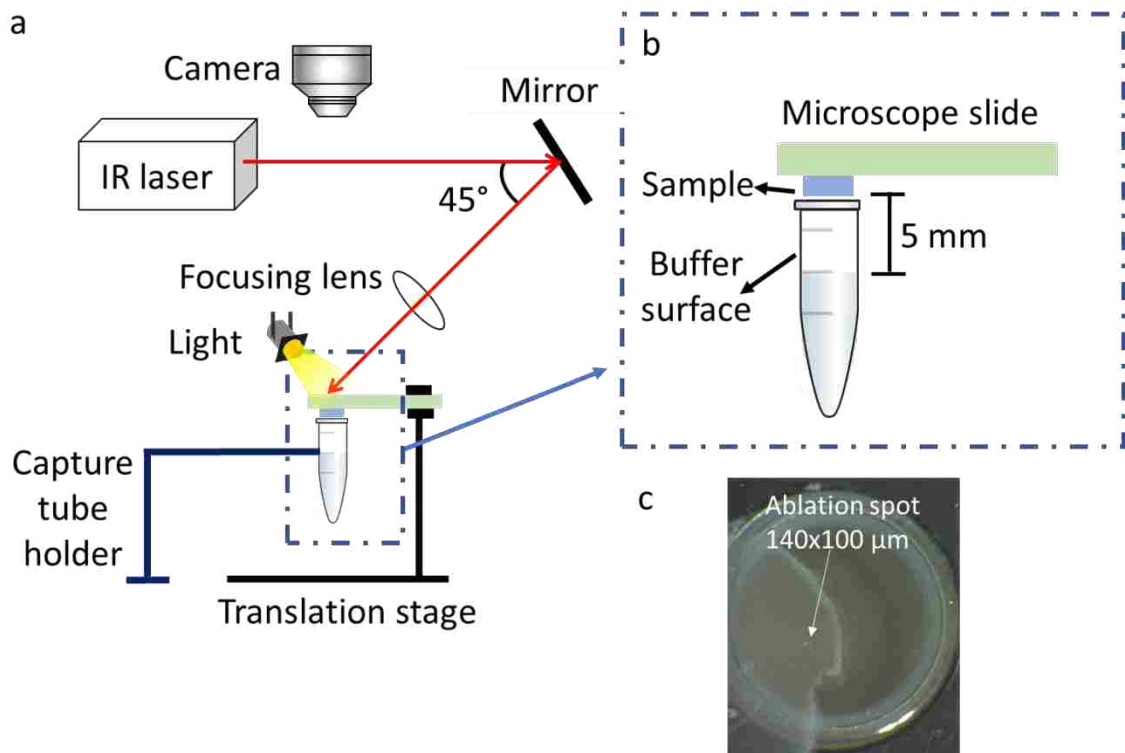


Figure 2.1 Schematic of the laser ablation and transfer system: a) overview; b) detail of capture tube; c) tissue section after a single shot viewed from above the microcentrifuge tube.

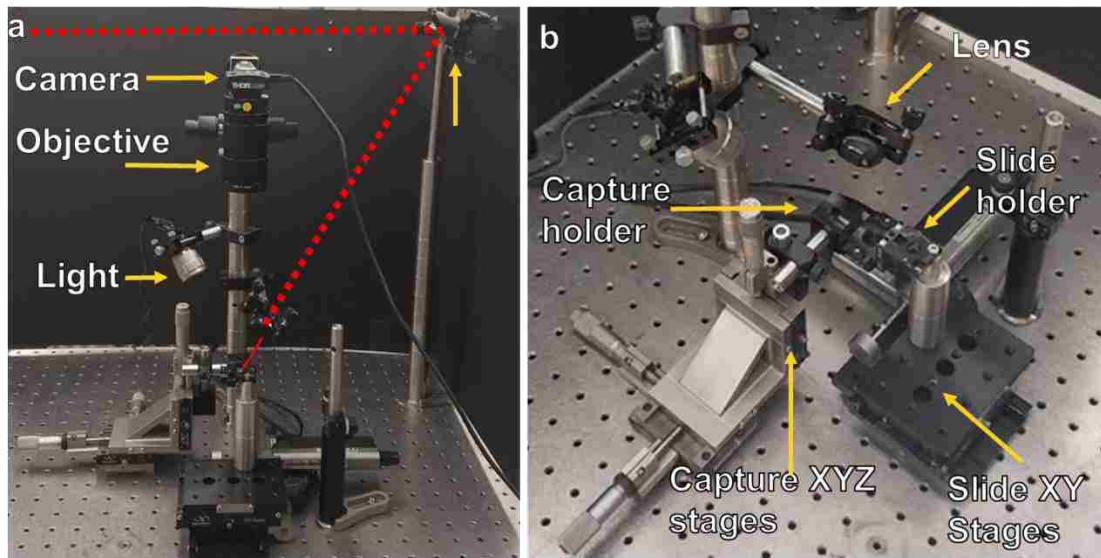


Figure 2.2 Photograph of laser ablation (a) and capture system (b).

### 2.3. ABLATION CONTROL SOFTWARE

The elements of the ablation system were controlled and monitored using LabVIEW software (National Instruments, Austin, Texas, U.S.) The virtual instrument (VI) captured an image of the sample on the stage and selection of arbitrary regions for ablation. The VI controlled the laser on/off and the translation stages.

A sample screenshot of the laser ablation control VI is shown in Figure 2.3. The four windows control the laser, translation stage, camera, and system calibration and ROI processing. The window at bottom left is the live camera and the window at bottom right is an image captured with the camera. There are three buttons in the laser control window for laser on/off, single shot, and capture ROI. The laser repetition rate can be adjusted in the laser control window. In the stage control window, the location of the tissue section with respect to the fixed laser and camera can be changed. In the camera control window, the resolution of the camera, frame rate of the video camera and exposure of the video camera can be adjusted. The top panel is used to calibrate the system and ROI processing. The system requires image registration prior to laser ablation. A single shot is made on the sample surface. The length and width of the ablated spot, as well as the location of the ablated spot (in pixels) are input into the VI for calibration. The speed of the translation stage can be varied between 100  $\mu\text{m/s}$  and 5 mm/s. In the work described below a speed of 1 mm/s was used. The divider is used to determine the spacing between the raster lines. For example, if the single shot was  $200 \times 300 \mu\text{m}$  and 2 is used as the divider, spacing between the raster lines is 150  $\mu\text{m}$ . In capture mode, the translation stage is rastered and the laser fires when it is within the boundary of the selected ROI. The precision determines the laser turn-on point. For example, if 80% precision is used, the laser is turned on when at least 80% of the laser spot is within the ROI.

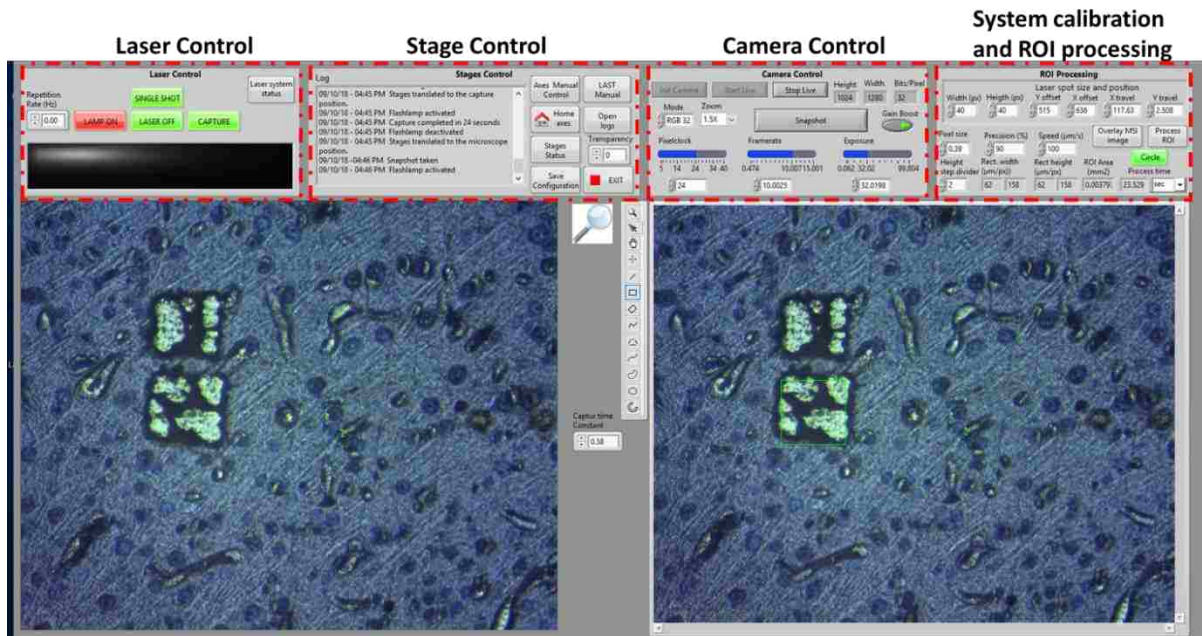


Figure 2.3 Screenshot of laser ablation control software

## 2.4. LASER ABLATION WORKFLOW

An IR laser ablation experiment can be accomplished using the following steps. The first step is sample pretreatment. Tissue samples are mounted on a microscope slide using a cryostat. Test samples in solution are deposited on the microscope slide using a pipette. Prior to laser ablation, the tissue or dried droplet samples are vacuum dried for 1-10 minutes. A 300  $\mu$ l microcentrifuge tube with capture solution is placed in a holder and the microscope slide with sample is installed on the translation stage. The tissue section is then moved into the view of the camera and an image is acquired. The ROI is selected using the drawing tool (Figure 2.3) and ROI processing can be used to determine the size of the ROI and the time required for ablation sampling. The ablation process is then initiated and after the ROI is ablated, the microcentrifuge tube is removed for further processing

## 2.5 MALDI TOF/TOF MS

A Bruker Ultraflex extreme MALDI TOF/TOF mass spectrometer was used in this work for protein identification (Chapter 1 and Chapter 4). This instrument equipped with a frequency tripled Nd:YAG 355 nm solid-state laser with a homogenized modulated beam (Smartbeam II) laser operating at 1-1000 Hz repetition rate. The laser spot size can be adjusted from 10-100  $\mu\text{m}$ . The  $m/z$  range is up to 100,000  $m/z$ . This Bruker Ultraflex extreme MALDI TOF/TOF system was used for MALDI MSI (Chapter 1).

## 2.6 UPLC-HDMS<sup>E</sup>

A hybrid ion mobility quadrupole time-of-flight hybrid mass spectrometer (SYNAPT G2-S HDMS<sup>E</sup>, Waters, Milford, MA) equipped with a nanoAcuity ultra-performance liquid chromatography (UPLC) system was used for protein identification and quantification (Chapter 1). The instrument uses travelling wave ion mobility (IM) for gas-phase size-to-charge separation.<sup>204-205</sup> The SYNAPT G2-S can acquire signal in data dependent acquisition (DDA) or data independent acquisition (DIA) modes. With DDA, the most abundant precursor ions are selected and fragmented.<sup>206</sup> With DIA, all ions within a  $m/z$  range are fragmented simultaneously.<sup>207</sup> Combined with UPLC, the SYNAPT G2-S can differentiate samples by retention time, size, and  $m/z$ .

## 2.7 SANGER SEQUENCING

The integrity of DNA templates was assessed by Sanger sequencing. Control and ablated DNA samples were processed using a sequencing kit (BigDye v3.1, Applied Biosystems, Foster City, CA), and reads were generated on an ABI 3130xl Genetic Analyzer fitted with 50-cm capillary arrays and a separation matrix POP-7 polymer. The ABI 3130xl Genetic Analyzer uses

capillary electrophoresis to separate DNA fragments which are generated from the first step of the Sanger sequencing. The system uses laser induced fluorescence detection.

Sequence data were analyzed with Sequencing Analysis Software v5.3 (Applied Biosystems) and aligned against a reference sequence. Chromatograms were viewed using Geneious software.<sup>208</sup> The quality of DNA was evaluated with regard to the base call quality value (QV) score and continuous read length (CRL) of the chromatograms.<sup>209-210</sup> The QV is defined by

$$QV = -10 \times \log_{10} P_e \quad (2-1)$$

where  $P_e$  is the probability that the base call is an error.<sup>211</sup> A QV equal to or greater than 20 (QV20+) corresponds to a 1% probability of incorrect nucleotide identification and indicates a high quality base call. The CRL represents the longest uninterrupted stretch of bases with QV higher than a specified limit (QV 20).

## **2.8 BIOANALYZER**

RNA concentration and integrity were assessed using an Agilent Bioanalyzer 2100 (Agilent, Santa Clara, CA) in Chapter 6 with an RNA 6000 Pico Kit (Agilent). This system uses microfluidic chip-based electrophoresis to separate RNA or DNA samples by molecular weight and uses laser induced fluorescence detection. The bioanalyzer is used to quantify RNA or DNA with respect to a standard RNA/DNA ladder run concurrently on the chip. In each assay (Figure 2.4), a typical trace displays the fluorescence intensity of the eluting components, with the lower marker eluting first (~22 s), followed by smaller RNA fragments collectively labeled as the 5S region (~24-28 s) and finally the peaks for the 18S (~40 s) and 28S subunits (~48 s). The software assesses features of the regions the electrophoretic trace to determine an RNA integrity number

(RIN) which can range from 1-10, with 1 indicating highly degraded RNA and 10 representing fully intact RNA.<sup>151</sup>

The commercial RNA 6000 Pico Kit is designed for low concentration RNA samples and has a quantitative range from 50 to 5000 pg/ $\mu$ L, detection limit of 200 pg/ $\mu$ L, and reproducibility of 20%. This kit is sensitive to common contaminants, such as salts, free nucleotides, solvents, detergents, DNA, or proteins, necessitating care in its use.

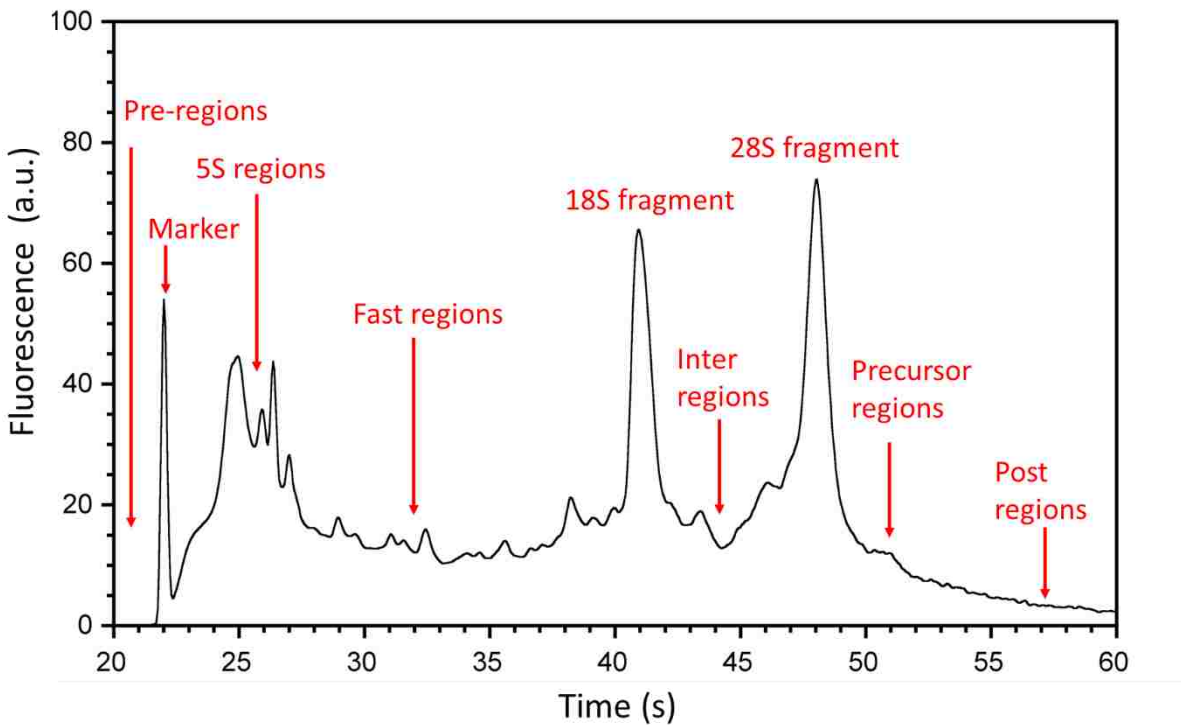


Figure 2.4 Sample electropherogram detailing the regions that are indicative of RNA quality

## 2.9 PCR

DNA was PCR-amplified with a thermal cycler (iCycler, BioRad, Hercules, CA) in 0. For qPCR, the cDNA generated using a reverse transferase reaction from the captured RNA was quantified by qPCR with a real-time PCR system (QuantStudio 6 Flex, Applied Biosystems)

(Chapter 6). The instrument collects fluorescence data following each PCR extension step. This instrument also performs a melt curve analysis to assess the qPCR final product. A single absorption peak indicates a pure final product whereas multiple peaks indicate multiple final products for a specific primer.

## **2.10 QUBIT**

DNA concentration was determined using fluorometric quantitation (Qubit 2.0, Thermo Fisher, Waltham, MA). The Qubit is a benchtop fluorometer for DNA, RNA, and protein quantification. The Qubit requires 1  $\mu$ l of sample and takes 2 minutes for DNA and RNA quantification and 15 minutes for protein quantification. A Qubit dsDNA HS Assay Kit (Thermo Fisher) was used which is selective for double stranded DNA and accurate for initial sample concentrations from 10 pg/ $\mu$ l to 100 ng/ $\mu$ l. This assay is also tolerant of common contaminants, such as salts, free nucleotides, solvents, detergents, or proteins.

## **2.11 FLUORESCENCE READER**

Enzyme activity, described in CHAPTER 4, was measured using a microplate reader (1420 Plate Reader, GMI, Perkin Elmer Wallac, Ramsey, MN) which can measure fluorescence, luminescence, and absorbance. Different microplates between 1-835 wells can be scanned. Up to 10 samples can be scanned with 1 minute.

## **2.12 TISSUE SAMPLES PREPARATION**

Rat tissue was obtained from the LSU School of Veterinary Medicine Division of Laboratory Animal Medicine in accordance with the requirements of the LSU Institutional Animal Care and Use Committee or purchased from Pel-Freez Biologicals (Rogers, AR). Rats were

exposed to carbon dioxide (5 psi) and brain or kidney were removed intact and snap-frozen in liquid nitrogen within 30 minutes. The tissue was stored at -80°C prior to sectioning.

Frozen tissue samples were sectioned at -25°C using a cryostat (CM 1850, Leica Microsystems, Wetzlar, Germany). Optimal cutting temperature solution (OCT, Sakura Finetek, Torrance, CA) was used to fix one side of the sample to the cryostat support, avoiding contact of the OCT solution with the exposed side of the tissue. For laser ablation, sections were cut at 50 µm thickness and mounted on plain microscope glass slides. For MALDI MSI experiments, frozen tissue samples were sectioned at a thickness of 10 µm and thaw-mounted on ITO coated microscope slides (University Wafer, South Boston, MA).

## **2.13 CHEMICAL AND MATERIALS**

Sequencing grade modified trypsin was purchased from Promega (Madison, WI). Reagents DL-dithiothreitol (DDT, 98%), iodoacetamide (IAA, BioUltra, 99%), α-cyano-4-hydroxycinnamic acid (CHCA), and ammonium bicarbonate (ABC, BioUltra, 99.5%) were obtained from Sigma-Aldrich (St Louis, MO). Trifluoroacetic acid (99.5%, LC-MS grade) and acetonitrile (99.9%, LC-MS grade) were obtained from Thermo Fisher Scientific. Bovine serum albumin (BSA) and glass microscope slides (25 × 75mm) were obtained from VWR (Radnor, PA). BSA from VWR was used as substrate for trypsin digestion. Ultrapure water (18 MΩ) was produced in house with a Barnstead nanopure diamond lab water system (Thermo Fisher Scientific). The ABC buffer was prepared at a concentration of 10 mM and corrected to a pH of 7.4. Tissue-Tek OCT Compound (Catalog 4583) was purchased from Skura Finetek.

A Bradford assay kit (Coomassie Plus, Thermo Fisher Scientific), which included Coomassie dye and BSA protein standard, was used to build calibration curves for protein

quantification. A fluorescent protease assay kit (Pierce, Thermo Fisher Scientific) included L-(tosylamido-2-phenyl) ethyl chloromethyl ketone (TPCK) treated trypsin, fluorescein isothiocyanate (FTIC) labelled casein, and tris buffered saline (TBS; 25 mM tris; pH 7.2, 150 mM NaCl). An Amplex red catalase assay kit (Life Technologies, Grand Island, NY) included Amplex red reagent, dimethylsulfoxide (DMSO), horseradish peroxidase, hydrogen peroxide, reaction buffer, and catalase. Sinapic acid (SA, Sigma-Aldrich, St. Louis, MO) matrix was prepared at a concentration of 10 mg/ml in 70:30 methanol with 0.1% TFA. TVLE buffer (10 mM Tris, 0.05 mM EDTA) was made using 1 M Tris (pH 9) from Amresco (Solon, OH) and 500 mM EDTA and nuclease-free water from Ambion (ThermoFisher, Waltham, MA). Reagent suppliers for genomics analysis were listed in Table 2.1.

Table 2.1 Sources for laboratory supplies

Company	Location	Item	Catalog Number
ThermoFisher Scientific	Waltham, MA	Human Kidney Total RNA	AM7976
		RNA Storage Solution (stabilizes purified RNA)	AM7000
		Water (nuclease-free)	10977023
		SuperScript III reverse transcriptase	18080085
		RNaseOUT recombinant ribonuclease inhibitor	10777019
		Random primers	48190011
		Oligo (dt) primers	12577011
		dNTP mix	18427013
		qPCR primers	10336022
		SYBR Select Master Mix	4472908
		MicroAmp 96-well plates	N801-0560
		MicroAmp Optical adhesive film	4360954
		Plasmid pGEM-3Zf(+) Control DNA template	P2411
		Amplitaq Gold PCR reagents	4398881
		BigDye sequencing reagent	
Corning	Corning, NY	Axygen Maxymum Recovery 0.2-ml tubes	PCR-02-L-C
		Axygen Maxymum Recovery 0.5-ml tubes	PCR-05-L-C
Eppendorf	Hauppauge, NY	DNA LoBind 1.5-ml tubes	022431021
		DNA LoBind 2.0-ml tubes	022431048
Zymo Research	Irvine, CA	Direct-zol RNA MicroPrep kit with TRI-Reagent	R2060
		ZR BashingBead Lysis Tubes	S6003-50
		DNA/RNA Shield (sample preservation solution)	R1100-50
Agilent Technologies	Santa Clara, CA	RNA 6000 Pico kit	5067-1513
Sakura Finetek	Torrance, CA	Tissue-Tek O.C.T. Compound	4583
Promega	Madison, WI	Plasmid pGEM-3Zf(+) control DNA template	P2411

## CHAPTER 3 MALDI DIRECTED LASER ABLATION TISSUE MICROSAMPLING WITH DIA MASS SPECTROMETRY

A multi-modal workflow for mass spectrometry imaging was developed that combines MALDI imaging with protein identification and quantification by liquid chromatography tandem mass spectrometry (LC-MS/MS). Thin tissue sections were analyzed by MALDI imaging and the regions of interest (ROI) were identified using a specially-designed selections algorithm. A mid-infrared laser at 3  $\mu\text{m}$  wavelength was used to remove the ROI from the tissue section after MALDI imaging. The captured material was processed using a single-pot solid-phase-enhanced sample preparation (SP3) method and analyzed by LC-MS/MS using DIA-MS to identify and quantify proteins; more than 600 proteins were identified. Using the post-translational modifications chain, isoform, loss of the initial methionine, and acetylation, fourteen MALDI MSI peaks were identified. Comparison of the Kyoto Encyclopedia of Genes and Genomes (KEGG) pathways of the identified proteins was achieved through an evolutionary relationships classification system.

### 3.1. INTRODUCTION

Matrix-assisted laser desorption/ionization mass spectrometry imaging (MALDI-MSI) is a powerful tool to visualize the spatial distribution of a wide range of molecules in tissue sections.<sup>125, 212-216</sup> MALDI MSI has been used as a complementary tool to histology,<sup>36</sup> and applications include biomarker discovery,<sup>217</sup> disease classification, tumor heterogeneity,<sup>215, 218</sup> and monitoring of distribution of drug and drug metabolites in tissue to assess different stages of the drug discovery and development.<sup>219</sup> One of the major challenges of MALDI-MSI is in identifying compounds because many compounds tissue lead to ion suppression that can obscure signal from low abundant proteins.<sup>38, 216</sup>

Liquid chromatography coupled with tandem mass spectrometry (LC-MS/MS) is able to provide identification and quantification of a large number of biomolecules from tissue extracts but it can be difficult to preserve the localization information. Coupling MALDI MSI and LC-MS/MS in a single workflow has the potential to broaden the capabilities of mass spectrometry imaging.<sup>36, 213, 215, 217, 220</sup> In this workflow, MALDI MSI can be used to locate ROI and LC-MS/MS can identify and quantify biomolecules.<sup>221</sup>

Technologies that are capable of extracting discrete amounts of material from a tissue section are required to bridge MALDI MSI and LC-MS. As described in Chapter 1, liquid extraction is one of the techniques that can sample proteins from tissue section ROI.<sup>50, 222</sup> Localized sampling also can be achieved by manual microdissection, where a small portion of the tissue section is removed using pipette or needles under microscope.<sup>54, 56</sup> Manual microdissection can be performed on a tissue section which is mounted on a microscope slide covered by a parafilm layer (parafilm assisted microdissection).<sup>55</sup> An alternative to manual microdissection is laser capture microdissection (LCM), which employs a focused UV laser to cut the boundary of the ROI from a tissue section.<sup>67, 223-224</sup> Laser ablation and capture is another laser assisted technique that can be used to collect small regions from tissue section, where ROI are irradiated using a focused pulsed laser.<sup>100, 225</sup>

In the work described below, a workflow was developed using MALDI MSI coupled with laser ablation sampling with UPLC-HDMS<sup>E</sup> MS/MS for protein identification and quantification. Here, image contours generated from MALDI MSI were used to define ROI. Following that, laser ablation was used to ablate and capture ROI from the same tissue section after MALDI MSI. Bottom up protein identification and label-free quantification were achieved using data

independent and data dependent acquisition tandem mass spectrometry. The list of identified proteins was used for identification of MALDI MSI peaks.

### 3.2. EXPERIMENTAL

Prior to MALDI MSI, tissue sections were vacuum dried for 10 min and washed with 70% ethanol for 45 s and 95% ethanol for 45 s to remove lipids and salts. After washing, the tissue sections were vacuum dried for another 10 min before matrix application. Sinapic acid was sprayed on tissue section using in-house built nebulizer that has been described previously.<sup>226</sup>

The MALDI images of selected  $m/z$  values were normalized to the total ion current (TIC) and created using FlexImaging software. Firstly, the MALDI images were smoothed with Gaussian blur using Adobe Photoshop cs6 and contour filters were selected according to mean ( $\mu$ ) and standard deviation ( $\sigma$ ) of the image histogram. Protein quantification using MALDI MSI was achieved by ImageJ (National Institutes of Health, Bethesda, Maryland, U.S.).

Single-pot solid-phase-enhanced sample preparation (SP3) was used for tissue digestion .<sup>227</sup> Magnetic carboxylate modified particles (SpeedBeads, GE Life Sciences, Chicago, IL) and carboxylate-modified magnetic particles (Sera-Mag, GE Life Sciences) were mixed in a ratio of 1:1 (v/v), washed with water three times, and reconstituted in water at a concentration of 20  $\mu\text{g}/\mu\text{l}$ . Protein disulfide bond reduction was achieved by adding DL-dithiothreitol (DTT, Sigma-Aldrich) to each sample tube to a final concentration of 10 mM followed by incubation at 100 °C for 45 min and cooling at room temperature for 15 min. Alkylation was performed by adding iodoacetamide (IAA, Sigma-Aldrich) to each sample to a final concentration of 20 mM followed by incubation in the dark for 30 min. After reduction and alkylation, 2  $\mu\text{l}$  of the bead solution was added to each sample. ACN was added immediately after to a final concentration of 60% (v/v).

Afterwards, the samples were incubated at room temperature for 20 min, and then incubated on a magnetic rack for 2-5 min until the beads settled at the magnets. Protein clean-up was achieved by adding 70% ethanol, incubating for 5 min off the magnetic rack, and then incubating on the magnetic rack for another 2 min. This procedure was repeated twice with 70% ethanol and once with ACN and samples were finally dried at 37 °C. Samples were re-suspended in 10 µl ammonium bicarbonate buffer and sonicated for 5 min prior to trypsin digestion.

Trypsin (Promega, Madison, WI) digestion was performed with an enzyme to protein ratio of 1:20 (v/v). Samples were incubated at 37 °C overnight and shaken at 300 rpm with a thermal mixer. After that, the same clean-up steps performed earlier for the proteins were repeated before recovering the peptides. Peptide recovery was achieved by adding 10 µl 0.1% formic acid followed by sonication for 5 min. Afterwards, the samples were incubated on the magnetic rack for 2-5 minutes and the supernatant was collected, avoiding aspiration of any beads. Tryptic peptides obtained from SP3 were vacuum dried and stored at -20 °C prior to analysis.

Rat brain digests were analyzed with the LC-MS/MS. ProteinLynx Global Server (PLGS Ver. 2.5.2; Waters) was used for peptide identification with the following parameters: UniprotKB/Swiss-Prot *Rattus norvegicus* proteome database; maximum number of missed cleavages: 2; precursor mass tolerance: 5 ppm; fragment mass tolerance: 5 ppm; Minimum fragment ion matches per peptide: 3; fixed modification: carbamidomethyl C; variable modification: oxidation M; false positive rate: 5. Identified peptides with at least 5 amino acid length were used for blast analysis using an in-house software<sup>228</sup> and UniprotKB/Swiss-Prot *Rattus norvegicus* proteome database. The database was modified using PIT in order to include single protein entries with the following post translational modification: chain, initiator methionine,

signal peptide and transit peptide. Proteins with at least two matched peptides were considered as identified proteins.

Functional annotation was performed using Database for Annotation, Visualization and Integrated Discovery (DAVID) 6.8 bioinformatics resource.<sup>229-230</sup> The Kyoto Encyclopedia of Genes and Genomes (KEGG) database was used for pathway analysis. KEGG pathways with at least 5 proteins and p-value < 0.05 were considered. Proteins in the same pathway were output into the Search Tool for Recurring Instances of Neighboring Genes (STRING) version 10.5 to generate protein-protein interaction networks.<sup>231</sup> The interaction includes physical and functional associations; only the interactions among identified proteins were considered. The minimum required interaction score was set at 0.4 (medium confidence). Label-free protein quantification of UPLC-HDMS<sup>E</sup> results was performed by summing of the signal from the three most abundant unique peptides.

### **3.3. RESULTS AND DISCUSSION**

Three tissue sections from the same rat were used to obtain MALDI images. Two of the sections were consecutive and mounted on the same ITO slide and imaged sequentially. The third tissue section was not consecutive and was mounted on a separate ITO slide. Over 30 MALDI MSI peaks in the range from 3,000  $m/z$  to 30,000  $m/z$  were observed in each rat tissue section mass spectrum.

Figure 3.1 shows 14 representative MALDI images. The images can be sorted into three general types: homogeneous signal throughout, signal most intense in the corpus callosum and hippocampus, and signal least intense in the corpus callosum and hippocampus. For example, homogeneous images (blue) were generated from 8,569, 14,041 and 17,139  $m/z$ . Images at 14,122,

14,132, 14,192, 14,211, 18,401, and 28,217  $m/z$  (green) showed intense signal over the corpus callosum and hippocampus regions whereas images at 15,193, 15,845, 17,737, 21,912 and 22,092  $m/z$  (magenta) had relatively low signal over the corpus callosum and hippocampus regions.

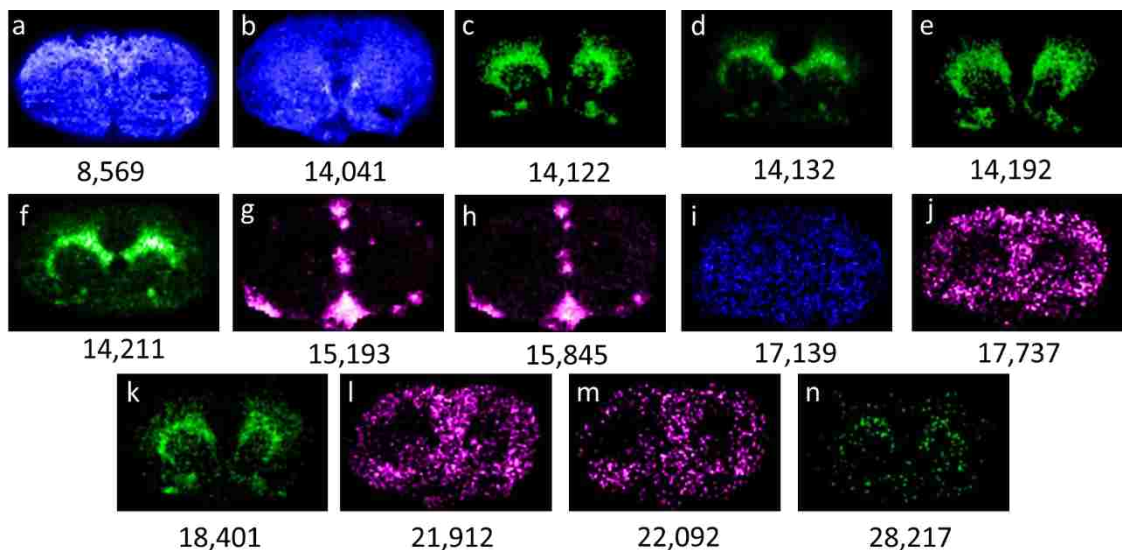


Figure 3.1 Representative MALDI image of rat brain tissue sections showing the distribution of signals of (a) 8569, (b) 14,041, (c) 14,122, (d) 14,132, (e) 14,192, (f) 14,211, (g) 15,193, (h) 15,845, (i) 17,139, (j) 17,737, (k) 18,401, (l) 21,912, (m) 22,092, and (n) 28,217  $m/z$ .

Figure 3.2 shows MALDI MSI ROI contours generated from the images in Fig. 1. The images were smoothed by Gaussian blur. Radius 10 was used, which equals a Gaussian blur kernel with 21 \* 21 pixels corresponding to 4.2 mm \* 4.2 mm. This radius gave the best smoothing effect for MALDI images obtained in this experiment. Contour filters were drawn according to mean ( $\mu$ ) and standard deviation ( $\sigma$ ). Three levels were drawn:  $\mu - 1.28\sigma$  (lower 80% quantile),  $\mu$  (mean) and  $\mu + 1.28\sigma$  (upper 80% quantile). The homogeneous (blue) images at 8,569, 14,041 and 17,139  $m/z$  have corresponding homogeneous contours that largely span the entire brain. The intense corpus callosum/hippocampus images (green) produced ROI centered on those regions, whereas the weak

signal corpus callosum/hippocampus images (magenta) produced ROI excluding those regions. The corpus callosum and hippocampus region ROI were used to guide laser ablation sampling.

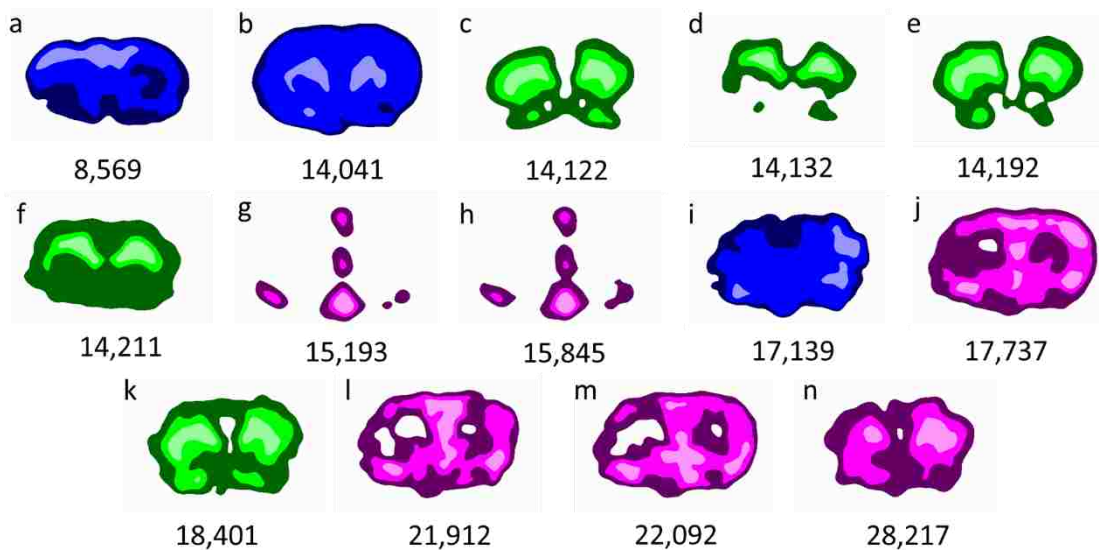


Figure 3.2 Contour maps obtained from MALDI MSI with color shade indicating the three levels: light shade is upper 80% quantile, mid-color intensity indicates mean, and dark indicates lower 80% quantile.

For all three tissue sections, the ROI were selected using the 14,122  $m/z$  (Figure 3.2c and Figure 3.3a) image which corresponds to myelin basic protein isoform 4 (MBP, Uniprot: P02688).<sup>226, 232-233</sup> The upper 80% quantile (light green) was used as a guide for ROI selection. Fig. 3b shows an optical microscope image of a tissue section after laser ablation. Three contiguous areas were ablated and captured from each tissue section at a laser fluence of 20  $\text{kJ}/\text{m}^2$ . Two of those areas encompassed the *corpus callosum* and *hippocampus* region in a 7  $\text{mm}^2$  total area and were collected in one tube as ROI 1. The third region covered a 4  $\text{mm}^2$  mid-brain region of low signal and was collected in a separate tube as ROI 2. The ROI 1 and ROI 2 samples were digested using the SP3 method described above and analyzed using UPLC-HDMS<sup>E</sup>.

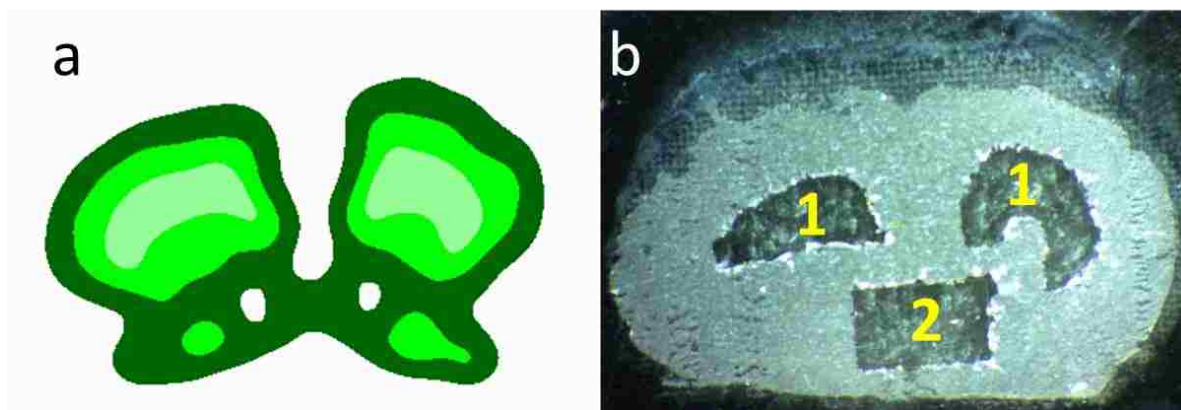


Figure 3.3 (a) Contour of MALDI MSI at 14,122  $m/z$ ; (b) bright-field microscope image of laser ablated rat brain tissue. location 1, corpus callosum (7  $\text{mm}^2$ ); location 2, hypothalamus (4  $\text{mm}^2$  square).

Figure 3.4 shows representative MS and MS/MS spectra from ROI 1. Product ions were correlated with their corresponding precursor ion with PLGS using the LC retention time and IM drift time. Fig. 3-4b shows a tandem MS spectrum that corresponds to the triply-charged precursor ion at 446  $m/z$  (Fig.4a),  $[M+3H]^{3+}$ . A series of immonium ions and consecutive singly/doubly charged y-series ions was observed from  $y_5$  to  $y_{11}$  corresponding to the peptide YLATASTMDHAR. This peptide is unique to the myelin basic protein family (all MBP isoforms).

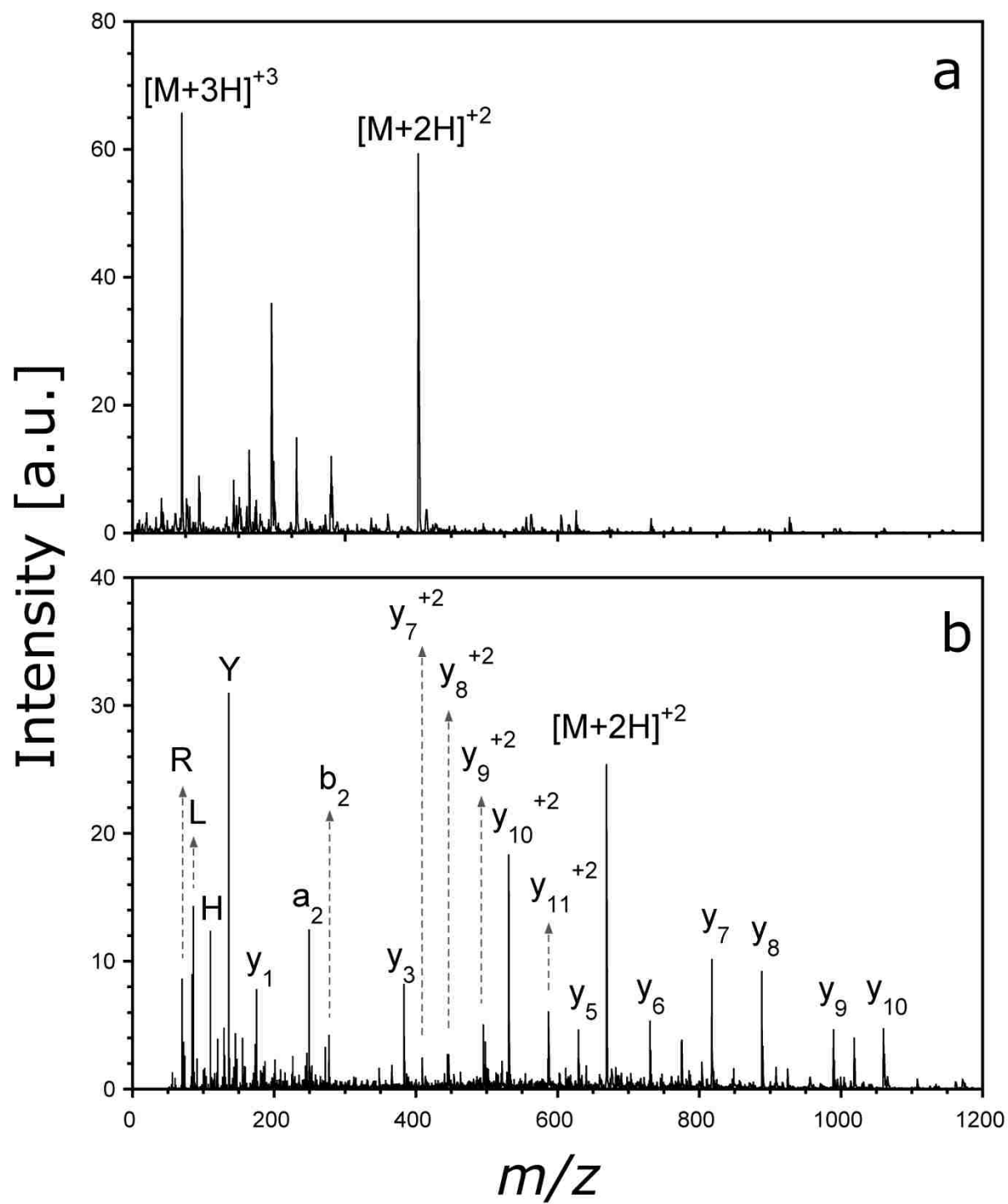


Figure 3.4 Representative UPLC-HDMSE mass spectra from analysis of an ROI 1 tissue section. a) MS of the MBP unique peptide YLATASTMDHAR; b) MS/MS spectrum of the triply charged peptide.

Peptides and proteins identified in ROI 1 and ROI 2 in three replicate tissue sections are summarized in Table 3.1. An average of 398 proteins were identified in the 7 mm<sup>2</sup> ROI 1 and an average of 268 proteins were identified in the 4 mm<sup>2</sup> ROI 2. A total of 3024 peptides were identified, about 7% of which were found in all samples. A total of 636 proteins were identified, a third of which were found in all samples. Unique peptides and proteins were also identified in each sample. About 45% of the identified peptides and 31% of the identified proteins were found in only 1 of the 6 samples. Some peptides and proteins were common to multiple sampling sections and positions. For example, hemoglobin, actins and tubulins were found in all regions and sections, most likely because they are highly expressed and relatively ubiquitous in tissue. The number of proteins identified is lower than that reported previously for infrared laser ablation and capture from brain tissue using five times more starting material as in this work.<sup>228</sup>

Protein quantification can be achieved by UPLC-HDMS<sup>E</sup> and MALDI MSI. Laser ablation sampling and UPLC-HDMS<sup>E</sup> allows precise relative quantification<sup>234</sup> of MBP protein family (all MBP isoforms) in the selected region. MBP quantification using MALDI MSI was achieved by summing the pixel intensity of the 14,122 *m/z* signal (MBP-4) within each ROI. The quantities of MBP in ROI 2 are 13 ± 4% in ROI 1 from UPLC-HDMS<sup>E</sup>. For UPLC-HDMS<sup>E</sup>, no identified peptides were unique to MBP-4 since four isoforms of MBP share around 80% identical sequence. Therefore, MBP quantification using UPLC-HDMS<sup>E</sup> was performed by summing the three most intense peaks that are unique to the MBP family instead of MBP-4. The quantities of MBP in ROI 2 are 60 ± 5% of that found in ROI 1 from UPLC-HDMS<sup>E</sup>.

Table 3.1 Summary of peptides and proteins identification in three tissue sections.

Peptides					
Tissue	ROI 1	ROI 2	ROI 1 and ROI 2	ROI 1 Only	ROI 2 Only
Section a	720	668	339	381	329
Section b	1312	637	412	900	225
Section c	2021	1002	598	1423	404
Tissue	ROI 1		ROI 2		
Section a Only	176		668		
Section b Only	774		637		
Section c Only	1481		1002		
Common to three tissue sections	1481		1002		
Proteins					
Tissue	ROI 1	ROI 2	ROI 1 and ROI 2	ROI 1 Only	ROI 2 Only
Section a	277	232	194	83	38
Section b	384	256	230	154	26
Section c	533	315	283	250	32
Tissue sections	ROI 1		ROI 2		
Section a Only	40		50		
Section b Only	147		74		
Section c Only	296		133		
Common to three tissue sections	237		182		

Molecular weights (MW) from proteins identified with UPLC-HDMS<sup>E</sup> were used for MALDI MSI peak identification. The MALDI MSI  $m/z$  peaks were compared against the list of protein molecular weights and a peak was considered to be a potential hit if it was within 500 ppm of a protein mass. Only singly charged protonated molecules were considered in this search. Seven MALDI MSI peaks have been identified. With consideration of PTMs, such as chain, isoforms, loss of the initial methionine and acylation, 14 MALDI MSI peaks were identified in total. Potential assignments of MALDI MSI peaks are summarized in the Table 3.2.

Table 3.2 Summary of all MALDI peaks assigned based on LC-MS/MS analysis of the laser ablated extracts including MW of the identified proteins, MW difference ( $\Delta M$ ) between MALDI peaks and MW of identified proteins, Uniprot accession number and protein names

Fig.1	MALDI MSI	MW (Da)	$\Delta M$ (ppm)	Accession No. (Uniprot)	Protein	ROI 1	ROI 2
a	8569	8565	350	P62982	Ubiquitin-40S ribosomal protein S27a	X	
a	8569	8565	350	Q63429	Polyubiquitin-C	X	
a	8569	8565	350	P0CG51	Polyubiquitin-B	X	
b	14,041	14,044	285	Q64598	Histone H2A type 1-F-Chain (2-130)	X	
b	14,041	14,045	356	A9UMV8	Histone H2A.J	X	
d	14,132	14,135	283	Q00729	Histone H2B type 1-A-Chain (2-127) <sup>b</sup>	X	X
d	14132	14138	495	P0CC09	Histone H2A type 2-A <sup>b</sup>	X	
e	14,192	14,194	211	Q00728	Histone H2A type 4 <sup>ab</sup>	X	
c	14,122	14,121	0	P02688-4	Myelin basic protein isoform 4 <sup>ab</sup>	X	X
f	14,211	14,211	70	P02688-4	Myelin basic protein isoform 4	X	X
i	17,139	17,136	117	P02688-3	Myelin basic protein isoform 3 <sup>ab</sup>	X	X
k	18,401	18,398	109	P02688-2	Myelin basic protein isoform 2	X	X
k	18,401	18,401	54	P45592	Cofilin-1-Chain (2-166)	X	
g	15,193	15,197	329	P01946	Hemoglobin subunit alpha-1/2-Chain (2-142)	X	X
h	15,845	15,847	189	P02091	Hemoglobin subunit beta-1 <sup>a</sup>	X	X
j	17,737	17,743	395	P10111	Peptidyl-prolyl cis-trans isomerase A-Chain (2-164)	X	
l	21,912	21,914	137	Q99P82	Claudin-11 <sup>a</sup>	X	
m	22,092	22,089	91	Q99P82	Claudin-11 <sup>b</sup>	X	X
n	28,217	28,213	106	P68511	14-3-3 protein eta	X	X
n	28,217	28,213	106	P61983	14-3-3 protein gamma <sup>ab</sup>	X	X

<sup>a</sup>loss of initial methionine; <sup>b</sup>acetylation;

In addition, five MALDI imaging peaks were identified by more than one protein. This may be due to isobaric species and low mass resolution, which was previously reported in MSI experiments.<sup>235</sup> This situation has consequences with regard to the identification of MALDI MSI peaks as well as cross-correlation of quantitative data between imaging and LC-MS/MS. High resolution instruments may be able to separate isobaric species.

Localized sampling of tissue proteins may provide additional information about the protein-protein interactions within specific pathways. To demonstrate this, a pathway analysis of the combined protein lists of the three tissue sections was performed using the DAVID

bioinformatics resource and STRING. MBP is associated with Alzheimer's disease (AD).<sup>236-238</sup> Therefore a pathway analysis using this protein is a good illustration. Figure 3.5 shows the network of protein-protein interaction pathways in ROI 1 (a) and ROI 2 (b) related to AD (KEGG ID: 05010). The full names of the proteins are listed in Table 3.3. Six of the proteins were only identified in ROI 1. The protein *ndufs1* is deficient in patients with AD.<sup>239</sup> Three proteins were identified in ROI 2. The protein *Mapk1* is also implicated in AD.<sup>240</sup> An additional pathway analysis was performed using a protein list obtained by merging the proteins identified in ROI 1 and ROI 2; the resulting network plot is displayed in Figure 3.5c. This combined region plot is similar to what would be expected from an analysis of the entire rat brain section without regard to the different concentrations of proteins in the different parts of the brain.

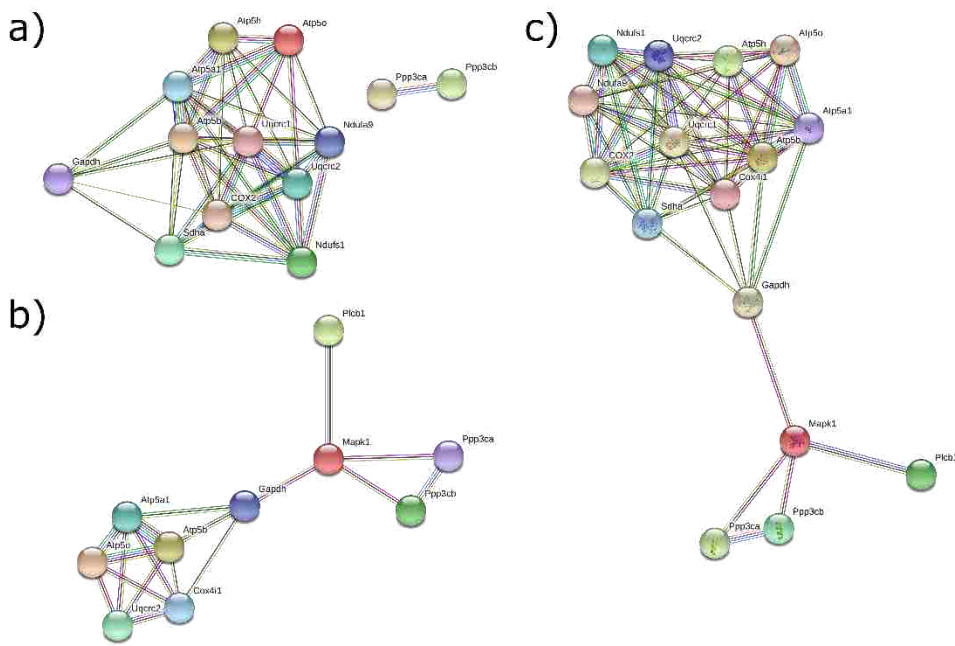


Figure 3.5 KEGG pathway of Alzheimer's disease using proteins identified in (a) ROI 1 and (b) ROI 2 (c) ROI 1 and ROI 2

Table 3.3 Full names of the proteins in Figure 3.5.

Abbreviation	Uniprot Accession	Protein Name
Atp5o	Q06647	ATP synthase subunit O, mitochondrial
Atp5a1	P15999	ATP synthase subunit alpha, mitochondrial
Atp5b	P10719	ATP synthase subunit beta, mitochondrial
Atp5h	P31399	ATP synthase subunit d, mitochondrial
Cox2	P00406	Cytochrome c oxidase subunit 2
Ndufs 1	Q66HF1	NADH-ubiquinone oxidoreductase 75 kDa subunit, mitochondrial
Ndufs 9	Q5BK63	NADH dehydrogenase [ubiquinone] 1 alpha subcomplex subunit 9, mitochondrial
Gapdh	P04797	Glyceraldehyde-3-phosphate dehydrogenase
Ppp3ca	P63329	Serine/threonine-protein phosphatase 2B catalytic subunit alpha isoform
Ppp3cb	P20651	Serine/threonine-protein phosphatase 2B catalytic subunit beta isoform
Sdha	Q920L2	Succinate dehydrogenase [ubiquinone] flavoprotein subunit, mitochondrial
Uqcrc 2	P32551	Cytochrome b-c1 complex subunit 2, mitochondrial
Uqcrc 1	Q68FY0	Cytochrome b-c1 complex subunit 1, mitochondrial
Cox4i1	P10888	Cytochrome c oxidase subunit 4 isoform 1, mitochondrial
Mapk1	P63086	Mitogen-activated protein kinase 1
Plcb1	P10687	1-phosphatidylinositol 4,5-bisphosphate phosphodiesterase beta-1

### 3.4. SUMMARY

MALDI imaging directed mid IR laser ablation was used for protein identification and quantification from rat brain tissue sections. Tissue sections were imaged using MALDI and ROI were located from Gaussian smoothing and contour tracing. The upper 80% quantile of the MALDI image from MBP-4 was used as the guide for ROI selection: A 7 mm<sup>2</sup> area of the corpus callosum and hippocampus region and a 4 mm<sup>2</sup> from mid-brain were ablated and transferred. For MALDI imaging quantification, the amount of MBP-4 in ROI2 was 87± 4% lower compared to that in ROI1. For LC-MS/MS quantification, the amount of MBP (all isoforms) in ROI2 was 34± 5% lower compared to that in ROI1. More than 600 proteins were identified. Molecular weights of these proteins and selected post-translationally modified proteins were used to identify MALDI

MSI peaks. Chain, isoform, loss of the initial methionine, and acetylation PTMs were included, resulting in 14 MALDI MSI peaks identified out of 30 peaks. KEGG pathways of the identified proteins were identified to demonstrate localized protein-protein network interactions. MALDI MSI directed laser ablation coupled with LC-MS/MS may be used to further investigate protein-protein networks by linking protein interactions to their localization in tissue.

## CHAPTER 4 INFRARED LASER ABLATION AND CAPTURE OF ENZYMES WITH CONSERVED ACTIVITY\*

This chapter describes the use of IR laser ablation at 3  $\mu\text{m}$  wavelength to extract enzymes from tissue section and quantitatively determine their activity. Experiments were conducted with trypsin, which was ablated, captured and then used to digest bovine serum albumin (BSA). BSA digests were evaluated using matrix-assisted laser desorption ionization (MALDI) mass spectrometry (MS) and sequence coverage of 59% was achieved. Quantification was performed using trypsin and catalase standards and rat brain tissue by fluorescence spectroscopy. Both enzymes were reproducibly transferred with an efficiency of  $75\pm 8\%$  at laser fluences between 10 and 30  $\text{kJ}/\text{m}^2$ . Trypsin retained  $37\pm 2\%$  of its activity and catalase retained  $50\pm 7\%$ . The activity of catalase from tissue was tested using three consecutive 50  $\mu\text{m}$  thick rat brain sections. Two 4  $\text{mm}^2$  regions were ablated and captured from the cortex and cerebellum regions. The absolute catalase concentration in the two regions was consistent with previously published data, demonstrating transfer of intact enzymes from tissue.

### 4.1. INTRODUCTION

Enzyme histochemistry combines the measurement of enzyme activity with localization information and serves as a link between biochemistry and morphology.<sup>241</sup> Enzyme histochemistry is used in diagnostic pathology and pathobiology, as well as in experimental pathology.<sup>242</sup> The activity of an enzyme is regulated at different levels from mRNA to post translational

---

\* Some portions of the work reported in this chapter previously appeared as Wang, K., Donnarumma, F., Baldone, M. D., & Murray, K. K. (2018). Infrared laser ablation and capture of enzymes with conserved activity. *Analytica chimica acta*.<sup>337</sup> Reprinted by permission of Elsevier.

modifications<sup>243-244</sup> and from molecular interactions between the cytoplasm and organelles to other regulation mechanisms in the extracellular matrix.<sup>245</sup> Accordingly, the full picture of enzyme activity cannot be determined simply by total protein or mRNA quantification.

Imaging of fresh frozen tissue sections and biopsies using methods such as fluorescent probes, chromogenic probes, and *in situ* zymography<sup>30-31</sup> allows measurement of enzyme activity with localization information. In the case of fluorescent or chromogenic agents, probes can be sprayed on the tissue section before measuring the localized signal.<sup>246-247</sup> After enzyme reaction on the surface of the tissue section, the localized indicator is activated based on enzyme activity.<sup>246-248</sup> Similarly, *in situ* zymography is an electrophoretic technique that uses fluorescent or chromogenic reactions.<sup>249</sup> There are two general zymography methods:<sup>30, 250</sup> tissue sections can be mounted on a glass slide coated with a fluorescent substrate, or first mounted on a slide, then immersed in a solution containing fluorescent substrate. Unlike fluorescent or chromogenic probes that are able to detect various enzymes,<sup>246-247, 251-252</sup> the substrates used for zymography are typically protein based,<sup>253-254</sup> such as gelatin or collagen, which make *in situ* zymography well suited for proteases.<sup>255</sup> Imaging based methods require special probes, the design of which can be challenging due to time consuming steps and high costs<sup>256</sup> and their potential for non-specific binding.<sup>257</sup>

Extraction of enzymes from small regions of tissue sections allows the measurement of localized enzyme activity.<sup>258-259</sup> Regions of interest containing enzymes can be isolated via manual microdissection followed by extraction and analysis. Extraction from microdissected tissue allows measurement of isolated cell populations in solution rather than on the tissue section surface. This enables more flexibility in adjustment of reaction conditions such as temperature and pH, which

can play an important role on reproducibility of enzyme assay.<sup>260</sup> In addition, extraction of enzymes can facilitate absolute quantification of their activity, whereas imaging techniques are often limited to relative quantification.<sup>261-263</sup> Although regions of interest (ROI) can be isolated by manual microdissection, where the material is removed under an optical microscope,<sup>259, 264</sup> this technique is somewhat labor intensive and has limited reproducibility.<sup>265</sup>

An alternative dissection technique is laser capture microdissection (LCM),<sup>67</sup> which has been discussed in detail in Chapter 1. An alternative to LCM is laser ablation and capture, where the region of interest is removed with a pulsed infrared laser<sup>41, 266</sup> The ejected material is collected and biomolecules can be extracted without the need of cell lysis or addition of detergents.<sup>41, 266-267</sup> The main absorber of infrared laser radiation in tissue is water, which has an absorption maximum at 2.94  $\mu\text{m}$ .<sup>186</sup> The optical penetration depth is approximately 1  $\mu\text{m}$  at room temperature, but increases with temperature, facilitating greater material removal at higher pulse energies.<sup>268</sup> Another tissue absorber is protein, which has OH and NH stretch absorbers at 3  $\mu\text{m}$  and CH stretch absorbers at 3.4  $\mu\text{m}$ . Absorption at these wavelengths can produce ablation of proteins even in nominally dry samples.<sup>203</sup> Absorption of pulsed nanosecond mid-IR laser light is sufficiently rapid to produce a volumetric phase change and explosive boiling of the irradiated volume.<sup>269-270</sup> The recoil stress of the phase explosion leads to the ejection of particulates with size distributions that vary with laser energy and the mechanical strength of the tissue.<sup>269, 271</sup> The removal of material as particulates appears to protect fragile biomolecules from fragmentation allowing the capture of intact peptides, proteins,<sup>41</sup> and DNA<sup>267</sup> from tissue using a nanosecond laser. Near-IR and mid-IR picosecond lasers can even more efficiently produce explosive boiling in tissue and were used to ablate and capture cells, virus and proteins with conserved function and activity.<sup>272-274</sup>

In the work described below, enzymes from thin films as well as from tissue sections were ablated and captured using a nanosecond mid-IR laser, and their activity quantitatively assessed. Trypsin and catalase enzyme standards were laser ablated using a 3  $\mu\text{m}$  wavelength laser and the transfer efficiency was measured using Bradford assay whereas the activity of trypsin was qualitatively assessed by using it to digest bovine serum albumin (BSA) before analysis by MALDI mass spectrometry. Quantitative assessment of the activity of trypsin and catalase standards after laser ablation was measured using fluorescence assays and the activity of catalase ablated and captured from rat brain tissue sections was determined.

## **4.2. EXPERIMENTAL**

Enzymes were reconstituted in TBS or fluorescence reaction buffers and BSA was dissolved in 10 mM ABC buffer (pH 7.4) at a concentration of 0.5 mg/ml. Aliquots of the enzyme solutions were deposited on a plain microscope slide (cleaned with ethanol) and dried for 2 min under vacuum before ablation.

For the trypsin experiment, control trypsin and trypsin obtained from laser ablation was used to digest BSA. Four aliquots of 50  $\mu\text{l}$  BSA at a concentration of 0.4 mg/mL were used as the substrate for trypsin digestion. Disulfide bond reduction was achieved by adding DTT to each tube to a final concentration of 10 mM, and samples were incubated at 80  $^{\circ}\text{C}$  for 45 min. Alkylation was performed by adding IAA to a final concentration of 20 mM with incubation in the dark for 30 min. Laser ablated and captured trypsin was vacuum dried and re-suspended in 2  $\mu\text{L}$  of ABC buffer, and compared to control samples of trypsin without laser ablation. Samples were incubated in a 37  $^{\circ}\text{C}$  shaker at 600 rpm overnight. Mass spectra of the tryptic peptides were acquired using the Bruker Ultraflexextreme mass spectrometer operated in reflectron mode. Each spectrum was

produced by summing 500 individual spectra obtained at 1000 Hz repetition rate in partial sample random walk mode. Raw data were processed with FlexAnalysis 3.3 (Bruker). A tryptic peptide peak list was generated with maximum two missed cleavages, cysteine carbamidomethylation, and methionine oxidation. A mass tolerance of 250 ppm was used.

Enzyme and protein concentrations were measured with a Bradford colorimetric assay.<sup>275</sup> Calibration curves for enzyme concentration were obtained in triplicate using control aliquots of the target enzyme (Figure 4.1 and Figure 4.2). Calibration curves for the ablated proteins were obtained in triplicate using BSA standards from the Bradford colorimetric assay.

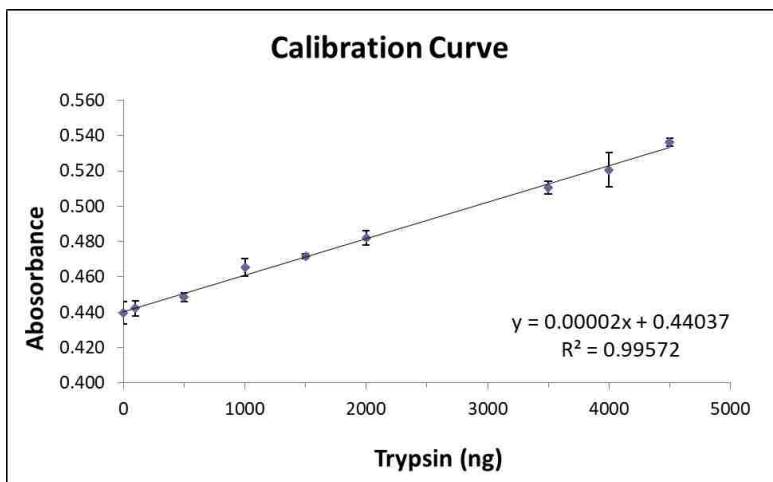


Figure 4.1 Calibration curve for the trypsin transfer efficiency test

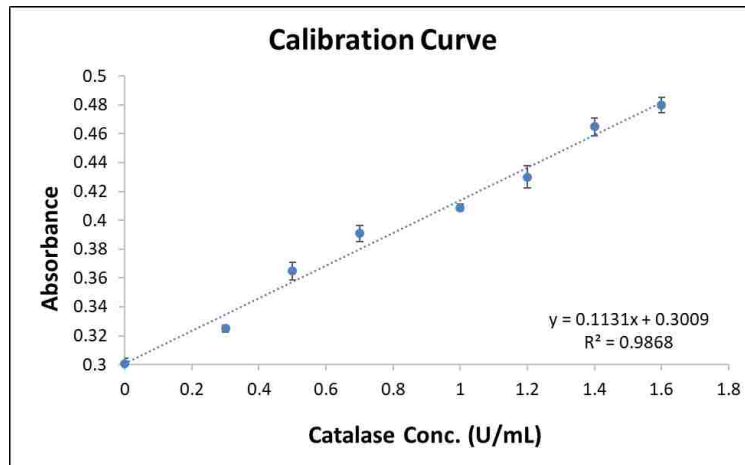


Figure 4.2 Calibration curve for the catalase transfer efficiency test

Trypsin activity was measured using the fluorescent protease assay kit according to the manufacturer’s protocol. Briefly, trypsin at a range of concentrations up to 5 mg/L was mixed with 100 µL of fluorescein isothiocyanate (FTIC) labelled casein (100 mg/L in TBS) and incubated at room temperature. Fluorescence was measured after 60 min incubation using a microplate reader at excitation and emission wavelengths of 435 and 538 nm, respectively, and expressed as relative fluorescence units (RFU; Figure 4.3 and Figure 4.4).

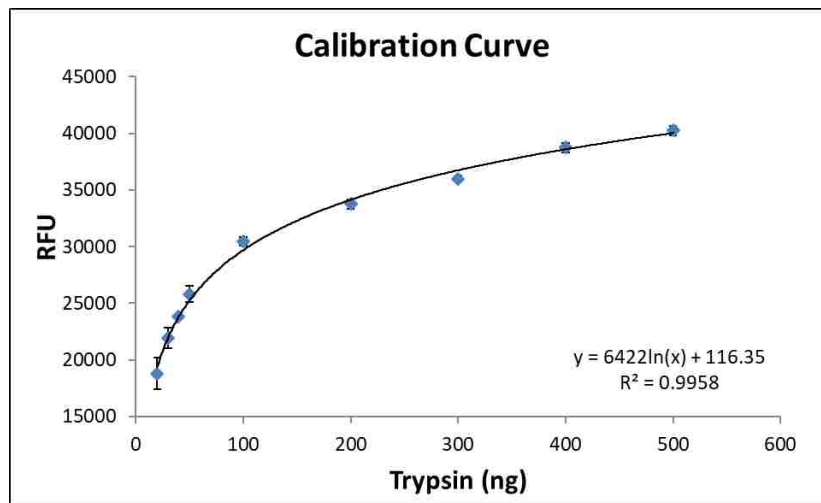


Figure 4.3 Calibration curve for the trypsin activity test

Catalase activity analysis was performed using the Amplex Red assay kit following the manufacturer's protocol. Briefly, calibration curves were generated using catalase at concentrations ranging from 0 to 1 unit/mL (U/mL), where 1 unit is defined as the amount of enzyme that will decompose 1.0  $\mu\text{mole}$  of  $\text{H}_2\text{O}_2$  per minute at pH 7.0 at 25°C. Samples and calibrants were incubated with 40  $\mu\text{M}$   $\text{H}_2\text{O}_2$  for 30 min at room temperature in the dark and then mixed with 100  $\mu\text{M}$  Amplex Red reagent at 37 °C. Fluorescence emission was measured after incubation for 30 min and 45 min using a microplate reader (Wallac 1420 Victor 2; PerkinElmer, Waltham, MA). Excitation and emission wavelengths of 571 nm and 585 nm were used (Figure 4.4). Background fluorescence was obtained from buffer-containing sample wells and subtracted from all data points.

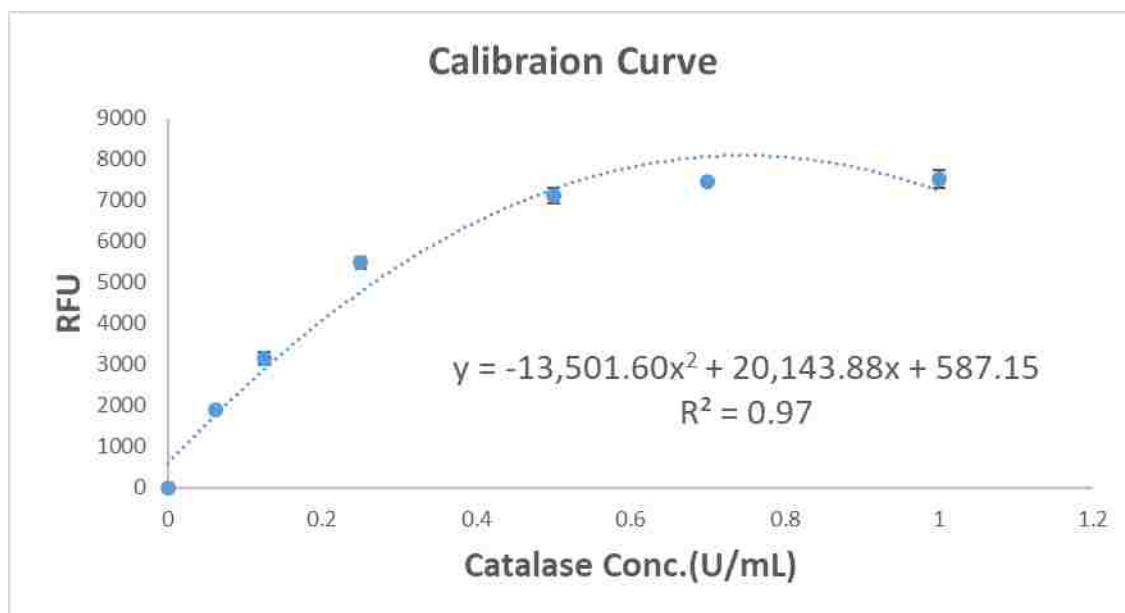


Figure 4.4 Calibration curve for the catalase activity test

### 4.3. RESULTS AND DISCUSSION

Initial experiments were directed at qualitatively assessing the presence of enzymatic activity after IR laser ablation. These experiments were aimed at assessing the effect of laser sampling on enzymes in absence of the tissue matrix. Trypsin (2  $\mu$ L, ~1000 ng) was deposited on a microscope slide, vacuum-dried, and the thin film was completely ablated at a laser fluence of 18 kJ/m<sup>2</sup> and collected in a 200  $\mu$ l volume of ABC buffer. Aliquots of BSA were either digested with the ablated and captured trypsin or with a control solution containing the same amount of enzyme deposited on the slide before ablation. BSA digests were analyzed by MALDI mass spectrometry. Figure 4.5 shows representative mass spectra of BSA tryptic peptides obtained using ablation capture and control trypsin. The peaks corresponding to protonated tryptic peptides with the intensity > 1,000 are indicated with red circles. The laser ablated trypsin yielded a similar spectrum compared to the control with respect to the number and  $m/z$  of the peaks, although the intensity was about half as large. A total of 42 tryptic peptides, corresponding to 61% sequence coverage, were identified for the control, whereas 44 peptides, corresponding to 59% sequence coverage, were identified with the ablated trypsin. The signal intensity and lower sequence coverage may result from either low efficiency of trypsin ablation and capture or from loss of enzyme activity of the ablated and captured trypsin.

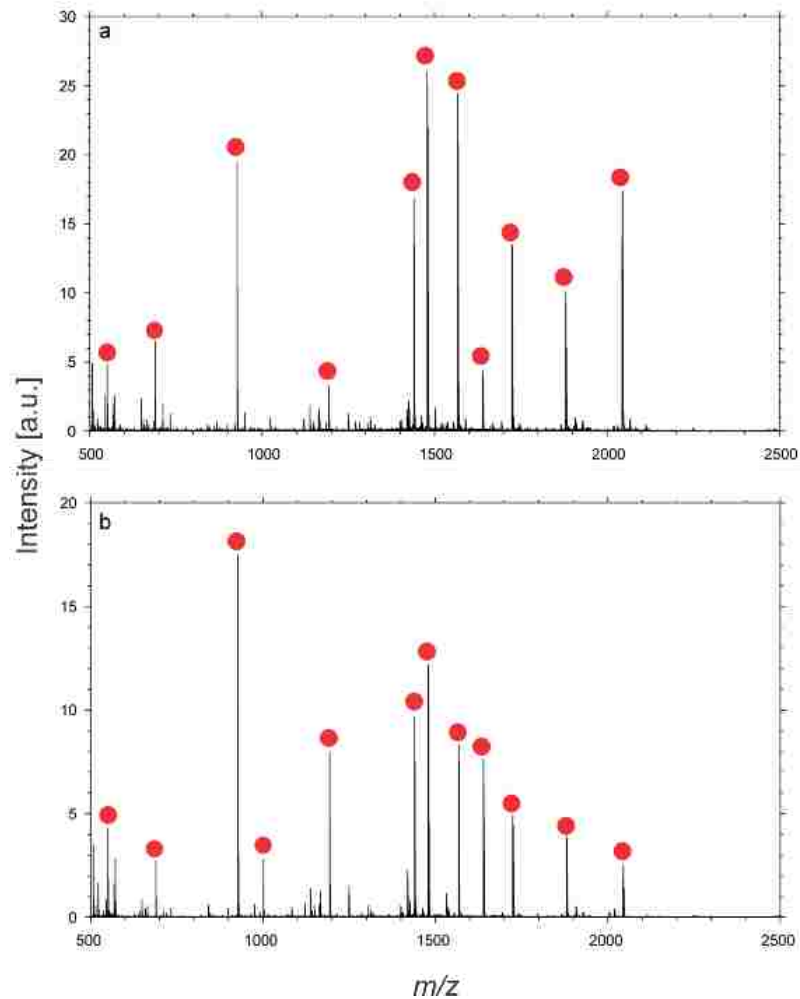


Figure 4.5 MALDI mass spectra of BSA tryptic peptides (red circles) obtained from (a) trypsin control and (b) laser ablation transferred trypsin.

The ablation and capture transfer efficiency can be defined as the ratio of the captured enzyme (both active and inactive) to the quantity of material ablated. To determine the capture efficiency, thin films of trypsin and catalase were ablated at various laser energies and the total protein was determined by Bradford assay. Dried sample deposits containing 4  $\mu\text{g}$  of trypsin were ablated at laser fluences of 10, 18, and 26  $\text{kJ}/\text{m}^2$  and the enzyme was captured in TBS buffer. A Bradford assay was used to measure the trypsin concentration from 3 replicate samples at each laser energy and from control samples. Figure 4.6a shows the transfer efficiency of trypsin (Dark gray) and

catalase (light gray). The resulting transfer efficiency was approximately  $73 \pm 9\%$  at all fluences:  $74 \pm 8\%$  at  $10 \text{ kJ/m}^2$ ,  $71 \pm 6\%$  at  $18 \text{ kJ/m}^2$ , and  $74 \pm 13\%$  at  $26 \text{ kJ/m}^2$ . The transfer efficiency for catalase was measured in a similar manner. Sample deposits containing 0.5-unit catalase were ablated and captured in buffer and analyzed by Bradford assay. The measured transfer efficiency was similar to that recorded for trypsin:  $73 \pm 7\%$  at  $10 \text{ kJ/m}^2$ ,  $79 \pm 5\%$  at  $18 \text{ kJ/m}^2$ , and  $75 \pm 7\%$  at  $26 \text{ kJ/m}^2$ .

Experiments were performed to determine the activity of the laser ablation transferred enzymes using a protease fluorescence assay. Sample deposits containing  $4 \mu\text{g}$  trypsin were ablated and captured at laser fluences of 10, 18, and  $26 \text{ kJ/m}^2$  and captured in TBS buffer. Figure 2b shows the trypsin activity (dark gray) obtained with the fluorescence assay:  $44 \pm 1\%$  at  $10 \text{ kJ/m}^2$ ,  $35 \pm 2\%$  at  $18 \text{ kJ/m}^2$ , and  $32 \pm 2\%$  at  $26 \text{ kJ/m}^2$  compared to the activity of the control. To determine the activity of the laser ablation captured catalase, samples containing 0.5 U catalase were ablated and captured in the assay kit buffer solution. Figure 4.6b shows the activity of the catalase (light gray) determined by fluorescence assay:  $57 \pm 7\%$  at  $10 \text{ kJ/m}^2$ ,  $54 \pm 7\%$  at  $18 \text{ kJ/m}^2$ , and  $40 \pm 7\%$  at  $26 \text{ kJ/m}^2$ . These results indicate that approximately  $37 \pm 2\%$  of the transferred trypsin is active and approximately  $50 \pm 7\%$  of the transferred catalase is active and the activity is approximately one third lower at the highest laser energy. The loss of activity may result from heating and denaturation of the enzyme during laser ablation. Although infrared laser ablation has previously been shown to transfer proteins and DNA intact,<sup>266-267</sup> the heating may be great enough to denature a fraction of the enzyme molecules.

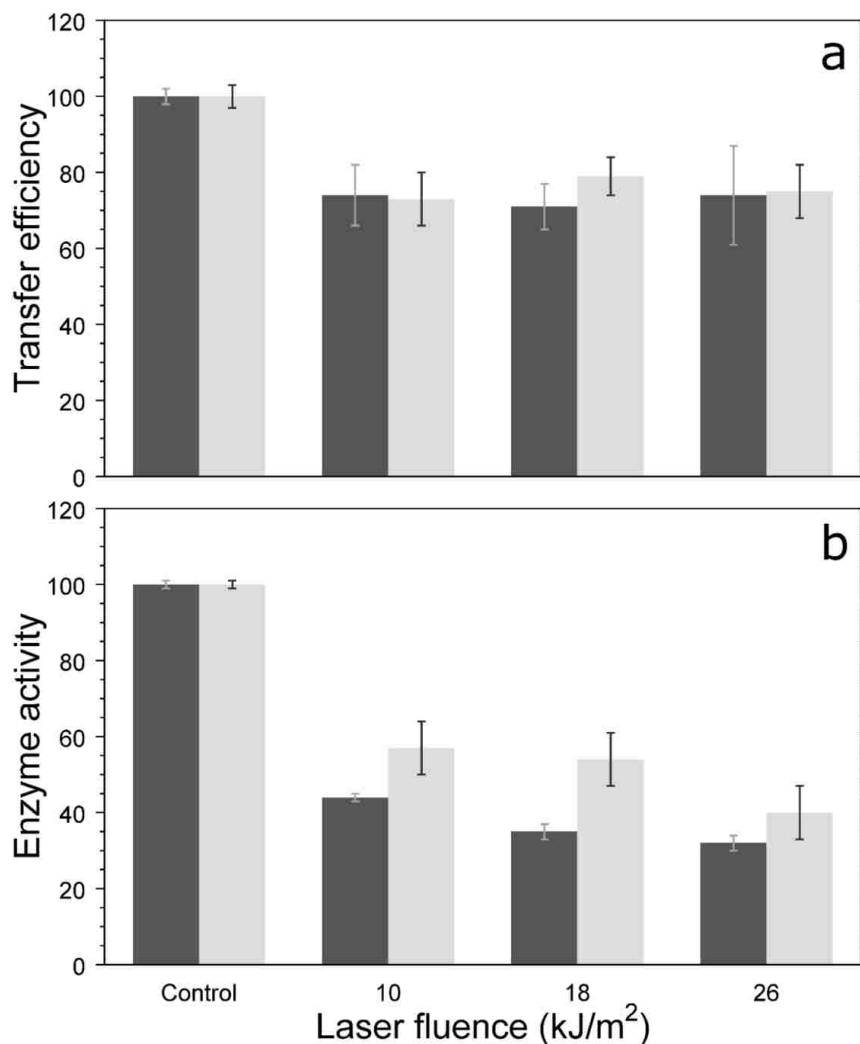


Figure 4.6 Transfer efficiency and activity of enzyme ablated at laser fluences of 10, 18, 26 kJ/m<sup>2</sup>: (a) enzyme transfer efficiency; (b) Enzyme activity. Dark gray indicates trypsin; light gray indicates catalase.

The trypsin activity results described in Figure 4.6b are consistent with previous studies using picosecond mid-infrared laser ablation of protein with conserved activity.<sup>276-277</sup> The study using picosecond laser also demonstrated that the enzymes in human plasma ablated with a picosecond laser are still active. The 70% transfer efficiency of protein material reported in our research is similar to that previously observed for mid-IR picosecond laser ablation capture of intact bacterial cells that subsequently were used to grow bacterial colonies.<sup>273</sup>

The effect of laser ablation on the activity of enzymes captured from tissue was studied using thin tissue sections. Here, the IR laser system was used to ablate material from sections of rat brain tissue mounted on microscope slides. Rat brain tissue sections 50  $\mu\text{m}$  thick were used. This allowed retrieval of more material per unit area compared to thinner samples. It was found that a fluence of 10  $\text{kJ}/\text{m}^2$  was not sufficient to completely ablate the tissue, therefore a fluence of 18  $\text{kJ}/\text{m}^2$  was used for these studies. Two spots of 4  $\text{mm}^2$  area from each tissue section (three tissue sections in total) were ablated and captured in 100  $\mu\text{l}$  of reaction buffer. The captured material was divided into a 50  $\mu\text{l}$  aliquot for total protein analysis by Bradford assay and a 25  $\mu\text{l}$  aliquot for catalase activity determination. Figure 4.7a shows a bright-field microscope image of a sagittal tissue section with the ablated areas, corresponding to the frontal cortex (Section 1) and the cerebellum (Section 2). The samples obtained from the cerebellum and frontal cortex yielded  $2.7 \pm 0.1 \mu\text{g}$  and  $2.5 \pm 0.1 \mu\text{g}$  total protein, respectively. According to manufacturer's protocol, the catalase activity of the ablated and collected tissue was measured after 30 and 45 min. At 30 min, the catalase activity obtained from the cerebellum region was  $11.2 \pm 0.7 \text{ mU}/\text{mm}^2$  from the frontal cortex  $8.0 \pm 0.7 \text{ mU}/\text{mm}^2$ . At 45 min, the activity was  $10.7 \pm 0.7 \text{ mU}/\text{mm}^2$  from the cerebellum and  $7.5 \pm 0.7 \text{ mU}/\text{mm}^2$  from the frontal cortex (Figure 4.7b). The catalase activity was normalized to the total protein in the captured sample to allow quantitative comparison of the activity in the different brain regions. The cerebellum catalase activity was  $16.3 \pm 0.3$  and  $16.0 \pm 0.2 \text{ U}/\text{mg}$  for 30 and 45 min, respectively, whereas the frontal cortex activity was  $12.5 \pm 0.3$  and  $12.0 \pm 0.3 \text{ U}/\text{mg}$ .

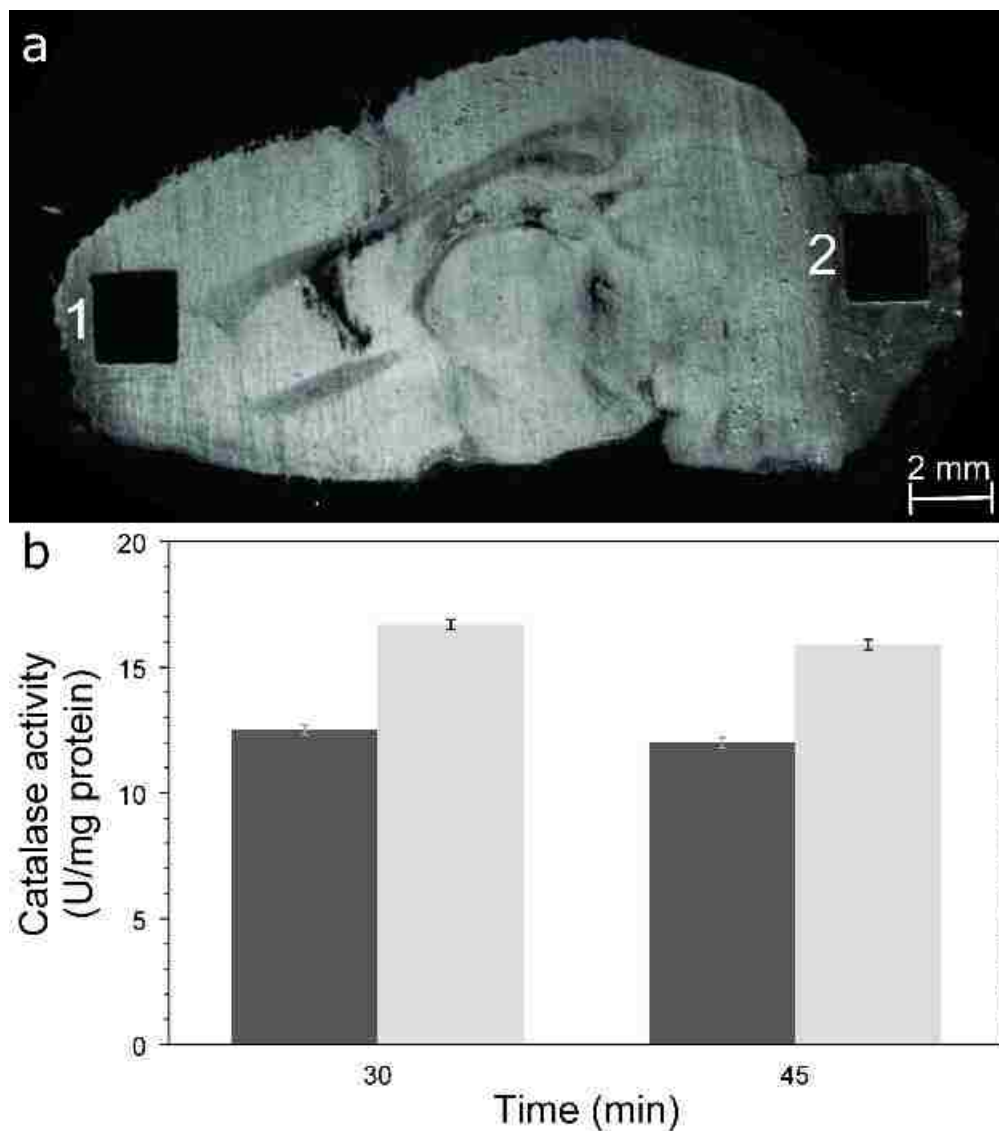


Figure 4.7 (a) Bright-field microscope image of laser ablation sampled rat brain tissue (1) frontal cortex and (2) cerebellum and (b) catalase activity from a fluorescence assay frontal cortex (gray) and cerebellum (light gray) at 30 and 45 min.

Taking into consideration the inhomogeneous water content of tissue samples<sup>278</sup> and the mechanical strength of the tissue matrix,<sup>269</sup> tissue samples may not be ablated as efficiently as pure enzymes. Nonetheless, the quantity of catalase captured from tissue is generally consistent with previously reported results, suggesting that the efficiency of transfer of active enzyme from tissue is comparable to that from dried-droplet samples. However, it must be noted that measuring

catalase activity in tissue poses several challenges. For example, the absolute activity in several brain compartments can vary as a function of rat age.<sup>279</sup> For this reason, the variation in catalase activity reported in various studies can be significant. The catalase activity in male albino Wistar rats was reported by Homi et al. to be 1.9 U/mg in the cortex and 3 U/mg in the cerebellum<sup>280</sup> and Jayaraman et al. reported values of 3 U/mg in the cortex and 4 U/mg in the cerebellum.<sup>281</sup> Siqueira *et al.* reported catalase activity equal to 0.4 U/mg in the cortex and 0.8 U/mg in the cerebellum of male Wistar rats.<sup>279</sup> Kazi et al. reported 1 U/mg in the cortex and 1.5 U/mg in the cerebellum of female Wistar rats.<sup>282</sup> Compared to the data above, Fortunato et al. reported lower absolute values of catalase in Wistar rat cortex and cerebellum. Using 6 animals in each control group, they reported values for the cortex differing over 5 times from each other, with numbers ranging from 0.0002 to 0.001 U/mg. In the cerebellum, they reported values differing over 20 times from each other, with values ranging from 0.0002 to 0.0035 U/mg.<sup>283</sup> In the IR laser ablation study a different breed of rat was used, which may explain the higher catalase activity measured. In addition, catalase activity was measured using laser ablated extract from consecutive sections of the same rat brain whereas the published literature reports activity from multiple animals. The catalase activity obtained from ablated and captured sample replicates was measured with relative standard deviation ranging from 1 to 2.5% which demonstrates the high reproducibility of the method.

#### **4.4. SUMMARY**

The results above demonstrate that enzymes can be IR laser ablated and captured from solid samples and from tissue while maintaining activity. The transfer efficiency of total protein was approximately 75±8% with about 2.5 µg protein obtained from 4 mm<sup>2</sup> of rat brain tissue, results which are consistent with previous studies of laser ablation transfer of proteins.<sup>266</sup> Approximately one-third of the captured trypsin and one-half of the captured catalase retained

enzyme activity as determined by fluorescence assay. The enzyme catalase was ablated and captured from rat brain tissue and the absolute activity measured was consistent with that anticipated for the different regions of the brain, suggesting that active enzymes can be efficiently ablated and captured from tissue. Due to the fast sampling speed, measurement of laser ablated and captured endoproteases and oxidoreductases can be used as a complementary tool to pathohistological evaluation of tissue in application such as surgery and tissue classification.

Future work will combine enzyme assays with liquid chromatography and mass spectrometry for protein identification<sup>266</sup> and with polymerase chain reaction for DNA analysis<sup>267</sup> of laser ablated and captured tissue. Whereas the current speed of both laser and translation allows for fast sampling for off-line analyses of mm<sup>2</sup> sized ROI, compatibility of the laser ablation system with mass spectrometry imaging will require a faster repetition rate laser as well as a smaller spot size to increase the lateral resolution.

## CHAPTER 5 INFRARED LASER ABLATION SAMPLE TRANSFER OF TISSUE DNA FOR GENOMIC ANALYSIS\*

This chapter describes the work using infrared (IR) laser ablation to remove DNA material from tissue sections mounted on microscope slides with subsequent capture in a solvent-containing microcentrifuge tube. Experiments conducted with a 3200-bp double-stranded plasmid DNA template demonstrated IR-laser ablation transfer of intact DNA. The transfer efficiency and the molecular integrity of the captured DNA were evaluated using Sanger sequencing, gel electrophoresis, and fluorimetric analysis. The plasmid DNA was reproducibly transferred with an efficiency of  $59\pm 3\%$  at laser fluences between 10 and 20 kJ/m<sup>2</sup> at 3  $\mu\text{m}$  wavelength. IR laser ablation sample transfer was then used to ablate and capture DNA from 50- $\mu\text{m}$  thick rat brain and kidney tissue sections. DNA was extracted from the captured material using five commercial DNA extraction kits that use significantly divergent methodologies, with all kits recovering sufficient DNA for successful amplification by the polymerase chain reaction (PCR). Four sets of primers were used, targeting one region of the *CYP 11b2* gene (376 bp) and three different regions of the *Snn1g* gene (298 bp, 168 bp and 281 bp). The PCR results were not consistently reliable when using un-purified ablation samples; however, after extraction, all samples produced PCR products of the expected size. This work expands the sampling capabilities of IR laser ablation, demonstrating that DNA can be isolated from tissue samples for genomic assays. Due to the small size of the ablated regions (1 mm<sup>2</sup>), this technique is useful in sampling discrete cell populations from tissue sections.

---

\* Some portions of the work reported in this chapter previously appeared as Wang, K., Donnarumma, F., Herke, S. W., Herke, P. F., & Murray, K. K. (2017). Infrared laser ablation sample transfer of tissue DNA for genomic analysis. *Analytical and bioanalytical chemistry*.<sup>267</sup> Reprinted by permission of Springer.

## 5.1. INTRODUCTION

Collecting informative DNA and RNA from heterogeneous bulk tissue sections is challenging due to the sampling of non-target cells, which can make it difficult to interpret molecular profiling data.<sup>11-12</sup> Sampling populations of target cells from selected regions of interest in the section is a strategy that can address this problem.<sup>284-288</sup> For example, cells can be isolated by manual microdissection<sup>34</sup> where a small portion of the section is removed using a modified Pasteur pipette or needle under an optical microscope or stereomicroscope.<sup>54, 289</sup> For many molecular analysis applications, sufficiently pure population of cells can be provided by manual microdissection;<sup>63</sup> however, the technique is labor intensive and has limited reproducibility.<sup>54, 62</sup>

Laser capture microdissection (LCM) has become a routine method for small-scale tissue sampling for extraction of homogeneous cell populations from tissue samples.<sup>65-68</sup> LCM can be performed with two basic configurations: IR capture; and, ultraviolet (UV) cutting.<sup>72</sup> The IR-LCM system was developed in 1996 and uses a thin thermoplastic film that covers the tissue section or cells on a microscope slide in a modified optical microscope.<sup>71</sup> A near-IR laser is focused onto the film, which melts and fuses with the cells and tissue. When the film is removed from the slide, the cells adhere with a strength that exceeds their adhesion to the slide; thus, the isolated region remains with the film and can be extracted for further analysis. UV-LCM was developed in 1998 and uses a UV laser to cut the boundary of a region of interest; detachment is accomplished by applying a pulse with the same laser to the center of the region.<sup>72</sup> The microdissected tissue is collected in a microcentrifuge tube cap containing a capture solvent or an adhesive substrate. Biomolecules are then extracted from the captured material.

For localized sampling of genomic material from heterogeneous tissue sections, both UV and IR laser microdissection are effective techniques for analysis of DNA and RNA.<sup>65, 68, 83</sup> Nonetheless, several limitations of LCM have been noted,<sup>77, 290</sup> such as the inability to completely remove the selected cells from the tissue section.<sup>91</sup> This may result from improper tissue mounting on slides<sup>75</sup> or incomplete dehydration.<sup>77</sup> Tissue sections must typically be limited to a maximum thickness of 15  $\mu\text{m}$ , and it is difficult to prevent cross-contamination between the collected samples and neighboring regions.<sup>75, 83</sup> Finally, expert manual operation and specialized consumables (e.g., coated microscope slides) are required.<sup>76, 82</sup>

An alternative to both IR and UV laser microdissection is laser ablation sampling of localized areas in tissue sections.<sup>41</sup> By continuous pulsed IR irradiation of an area of interest with a focused laser beam, it is possible to efficiently remove biomolecules from a surface for on-line and off-line analysis of peptides and proteins.<sup>100, 291-292</sup> Mid-IR lasers are highly efficient at ablating biomolecules from tissue sections.<sup>41, 98, 266, 293</sup> because mid-IR lasers can break up tissue and cellular structures (e.g., connective tissue, cellular membranes, and organelle membranes) while preserving biomolecule integrity, samples collected through IR laser ablation do not require cell lysis for downstream analysis.<sup>41</sup>

In this chapter, ablation of intact plasmid DNA using a 3  $\mu\text{m}$  wavelength mid-IR laser is described. After capture, the DNA was both sequenced directly and amplified by PCR. IR laser ablation sample transfer was performed with rat kidney and brain tissue sections and the genetic material was amplified with PCR.

## 5.2. EXPERIMENTAL

The commercially-supplied plasmid pGEM DNA template (3197 bp) was provided in TE buffer (10 mM Tris, 1 mM EDTA, pH 7.5) at ~200 ng/ $\mu$ L. Aliquots of 2  $\mu$ L were deposited onto a plain microscope slide (pre-cleaned with ethanol) and allowed to dry for 2 min under vacuum before ablation. Before sampling, tissue sections were dehydrated with a series of ethanol and chloroform washes to remove lipids and salts: 70% ethanol for 1 min; 95% ethanol for 1 min; and, 100% chloroform for 1 min. Slides were dried under vacuum for 30 min prior to sampling.

pGEM DNA concentrations after laser ablation were determined using fluorometric quantitation. Prior to measurement, plasmid DNA templates (control and ablated samples) were linearized by a restriction enzyme double-digest to eliminate interference by supercoiling. Digested DNA fragment sizes were confirmed by gel electrophoresis (sodium borate running buffer and 2% agarose gels).<sup>294-295</sup> Data from the Qubit assay were tested for statistical significance ( $p < 0.05$ ) with an analysis of variance (ANOVA) test in SAS 9.4. Genomic DNA samples from rat tissue were extracted with commercial DNA extraction kits.

To purify the captured genomic DNA from material obtained from tissue sections, five commercial DNA isolation kits (representing a wide array of methodologies) were used according to the protocols of the manufacturers. Briefly, three kits bind DNA to spin-columns, where two kits use either magnetic or non-magnetic beads. The kits differ as to whether they use proteinase K, DTT, or beta-mercapta-ethanol. Other differences include special digestion buffers and the use of pre-wash as well as wash buffers prior to elution of the DNA.

DNA material collected from rat kidney and brain tissue was PCR-amplified (using four sets of primers; Table 5.1) on a thermal cycler using either the raw ablated samples or ablated

samples that were subsequently processed with a commercial DNA extraction kit. PCR reactions used 10  $\mu$ L of DNA template and 15  $\mu$ L of a master-mix for a final concentration of 2.5 mM MgCl<sub>2</sub>, 1X buffer, 200  $\mu$ M each dNTP, and 1  $\mu$ M each of forward and reverse primers, with 1.25 units of polymerase (AmpliTaq Gold). PCR cycling conditions: [initial denaturation, 1X] 95°C (1 min); [polymerase activation, 9X] 95°C (1 min), 60°C (30 s), 72°C (1 min); and, [amplification, 32X] 95°C (20 s), 60°C (30 s), 72°C (1 min). PCR products were electrophoresed in 2% agarose sodium-borate gels (stained with ethidium bromide) and visualized on the BioRad ChemiDoc XRS+ system. Amplicon sizes were determined by comparison with the EZ Load 100-bp PCR Molecular Ruler.

Table 5.1 Primer information. CYP11b2 indicates gene *Rattus norvegicus* hydroxysteroid 11-beta dehydrogenase 2 gene; Snn1g indicates gene amiloride-sensitive sodium channel subunit gamma gene.

Gene Name	Sequence	Product
CYP11b2	Forward: TTC TTT CCA ACG GTC ACT CC Reverse: TAC CAC AAC CAC CCA GTC CT	376 bp
Snn1g set 1	Forward: AAA TCT TAC GGA GGC CCT TG Reverse: CTC TGG CTT CCC AAG AGA TG	298 bp
Snn1g set 2	Forward: CAA TAC CCC AGT CCC TGG TA Reverse: GCC TGG ATT CTG CTA TGC TC	168 bp
Snn1g set 3	Forward: CCA AAC CTG ACG ACC TGA GT Reverse: AGT CAG ATG AGG AGG GCA TC	281 bp

### 5.3. RESULTS AND DISCUSSION

Initial tests were conducted at laser fluences of 18, 24 and 36 kJ/m<sup>2</sup> (in duplicate) to assess the ability of the IR laser to transfer DNA without fragmentation. A double-stranded, 3197-bp plasmid DNA template (2  $\mu$ L, ~400 ng) was deposited on a microscope slide and vacuum-dried.

The dried residue was entirely ablated, transferring it to PCR tubes containing 200  $\mu\text{L}$  of TVLE buffer. For a control, 2  $\mu\text{L}$  of the same template was directly added to a PCR tube with 200  $\mu\text{L}$  of TVLE buffer. After sequencing, chromatograms of the ablated samples and control were compared with regard to the per-base quality value scores (QV20) and contiguous read length (CRL). Figure 5.1 shows representative regions of the chromatograms.

DNA sequencing results were not distinguishable between the control and ablated samples obtained at 18  $\text{kJ}/\text{m}^2$  or 24  $\text{kJ}/\text{m}^2$ ; however, data quality was lower for samples ablated at 36  $\text{kJ}/\text{m}^2$ . For example, the QV20 values for samples obtained at fluences of 18  $\text{kJ}/\text{m}^2$  ( $922\pm 4$  bp) and 24  $\text{kJ}/\text{m}^2$  ( $895\pm 21$  bp) were comparable to those of the control ( $898\pm 7$  bp). By contrast, samples taken at 36  $\text{kJ}/\text{m}^2$  ( $468\pm 39$  bp) had QV20 values that were nearly 50% lower than the control, resulting in much shorter reads with the QV scores falling to  $<10$  (90% accuracy) after only 600 bp (Fig. 1b). Similarly, CRL values obtained at fluences of 18  $\text{kJ}/\text{m}^2$  ( $916\pm 12$  bp) and 24  $\text{kJ}/\text{m}^2$  ( $915\pm 5$  bp) were comparable to the control ( $915\pm 5$  bp), whereas those for samples obtained at 36  $\text{kJ}/\text{m}^2$  ( $485\pm 53$  bp) were nearly 50% lower than for the control.

Based on the Sanger sequencing results, laser fluences  $\leq 24 \text{ kJ}/\text{m}^2$  had no discernible effect on the integrity of the plasmid DNA and its individual nucleotides. However, the sequencing results with samples obtained at 36  $\text{kJ}/\text{m}^2$  suggest that the higher laser fluence may have either fragmented the DNA or damaged individual nucleotides. These effects are most likely due to thermal or mechanical processes because the mid-IR wavelength used in this experiment does not provide sufficient energy to a single photon to trigger photochemical dissociation.<sup>202, 296-297</sup>

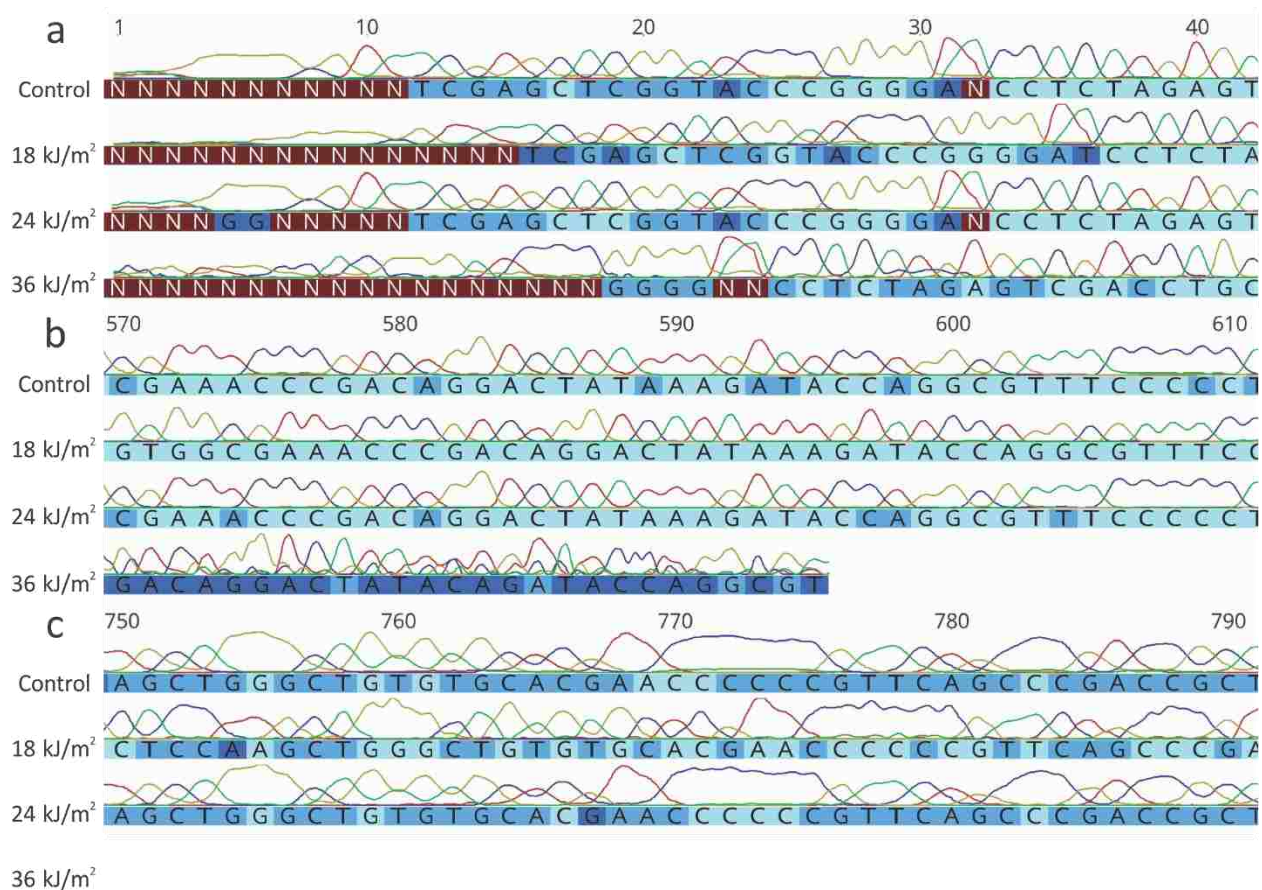


Figure 5.1 Segments of Sanger sequencing chromatograms of pGEM plasmid: a) 1 to 40 bp; b) 570 to 610 bp; c) 750 to 790 bp. Control indicates DNA without the laser ablation. Dark blue indicates  $QV < 20$ , blue indicates  $20 < QV < 40$  and light blue indicates  $QV > 40$ .

The transfer efficiency of the ablation process was assessed, using pGEM plasmid DNA and three laser fluences. Preliminary work demonstrated that laser fluences below  $10 \text{ kJ/m}^2$  were not able to completely ablate dried DNA samples, and the sequencing results showed that laser fluences in excess of  $24 \text{ kJ/m}^2$  could be damaging; hence, laser fluences of 10, 15 and  $20 \text{ kJ/m}^2$  (in triplicate) were used to measure transfer efficiency. Control and ablated samples were first double-digested (to minimize bias in the concentration estimates due to supercoiling<sup>298</sup> and then concentrations were estimated with the Qubit dsDNA HS Assay Kit. To verify that samples were not otherwise degraded, digested samples were also electrophoretically separated in a 2% agarose

gel (Figure 5.2), with all samples displaying fragments of the expected lengths (379 bp, 1150 bp and 1668 bp). Molecular ladders include the BioRad EZ Load 100-bp PCR Molecular Ruler (outside lanes) and the NEB Quick-Load Purple 2-Log DNA Ladder (center). Fluorimetric quantification yielded an average of 123 ng of DNA for the three energies tested: 10 kJ/m<sup>2</sup>, 120±9 ng; 15 kJ/m<sup>2</sup>, 129±13 ng; 20 kJ/m<sup>2</sup>, 120±13 ng and 209±3 ng for the control. Analysis of variance yielded a p-value of 0.88, which indicates that the difference in DNA yield was not statistically significant among the runs. Defining the transfer efficiency as the ratio of the recovered material to the control, an average transfer efficiency of 59±3% was obtained.

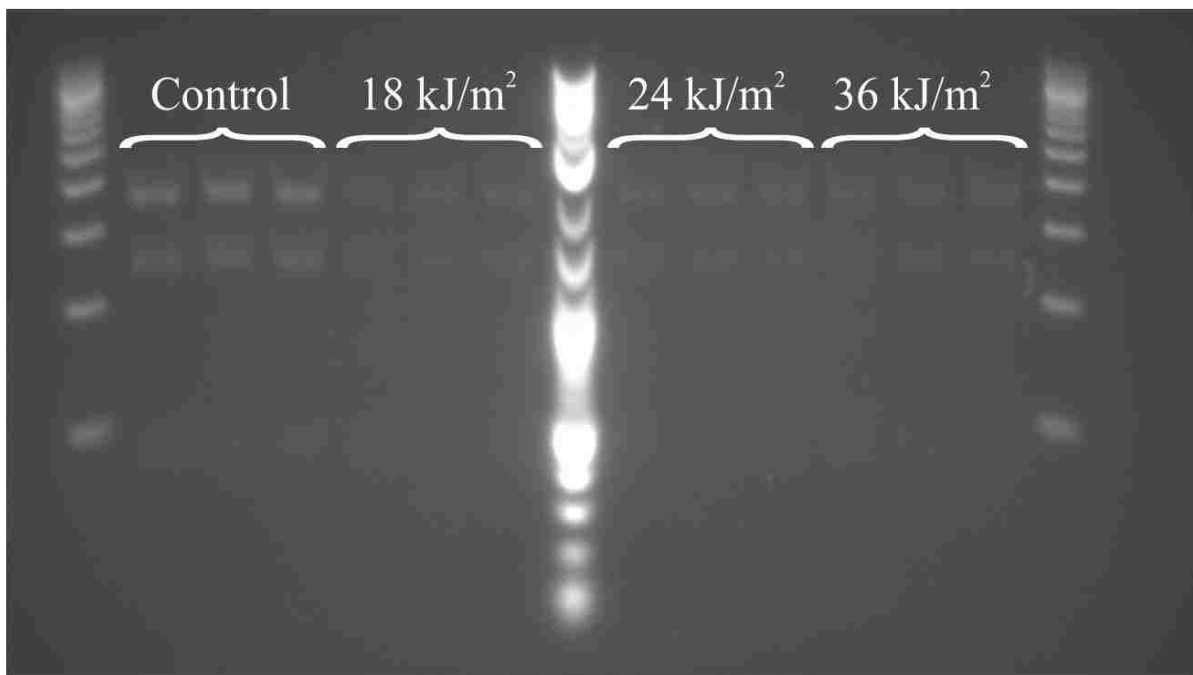


Figure 5.2 Agarose gel electrophoresis image of digested DNA template samples obtained from three different laser fluences and control. All samples were double-digested into three fragments: 379 bp, 1150 bp and 1668 bp.

The initial experiments with pGEM plasmid DNA provided proof-of-concept results but represent an ideal situation in which only DNA was present on the slide. To confirm the effectiveness of IR-laser ablation for the transfer of genomic material from tissue, rat brain tissue

sections mounted on a microscope slide as a test sample were used. To monitor potential contamination, negative controls (blank microscope slides) were included in the experimental design. IR laser ablation samples and negative controls were amplified using four sets of primers targeting two different genes. One primer was designed for the *hydroxysteroid 11-beta dehydrogenase 2* gene (CYP 11b2), producing an amplicon of 376 bp. The other three primers targeted the *amiloride-sensitive sodium channel subunit gamma* gene (Snn1g), producing three amplicons of different sizes: 298 bp (Snn1g 1), 168 bp (Snn1g 2) and 281 bp (Snn1g 3). Snn1g Set 1 and Set 2 are 600 base pairs apart, and Snn1g Set 2 and Set 3 are 2400 base pairs apart.

Ten spots of 4 mm<sup>2</sup> area were ablated and captured using TVLE buffer. These samples were amplified without further purification, and the PCR products were loaded on a 2% agarose gel (Figure 5.3). Overall, amplification of the un-purified ablation products was moderately successful. For instance, only Snn1g (set 2) generated the expected bands for all samples (Fig. 3d); by contrast, fewer than half of all other reactions generated a well-defined band and many non-specific amplification products were seen as well. These results were consistent with the fact that, although IR laser ablation produces highly homogenized samples, the captured material includes not only DNA, but also proteins, extracellular matrix, and RNA. All of these additional cellular components can inhibit a PCR reaction.<sup>299</sup> Therefore, the experiments were repeated with a DNA purification step to increase the specificity and effectiveness of the PCR amplification.

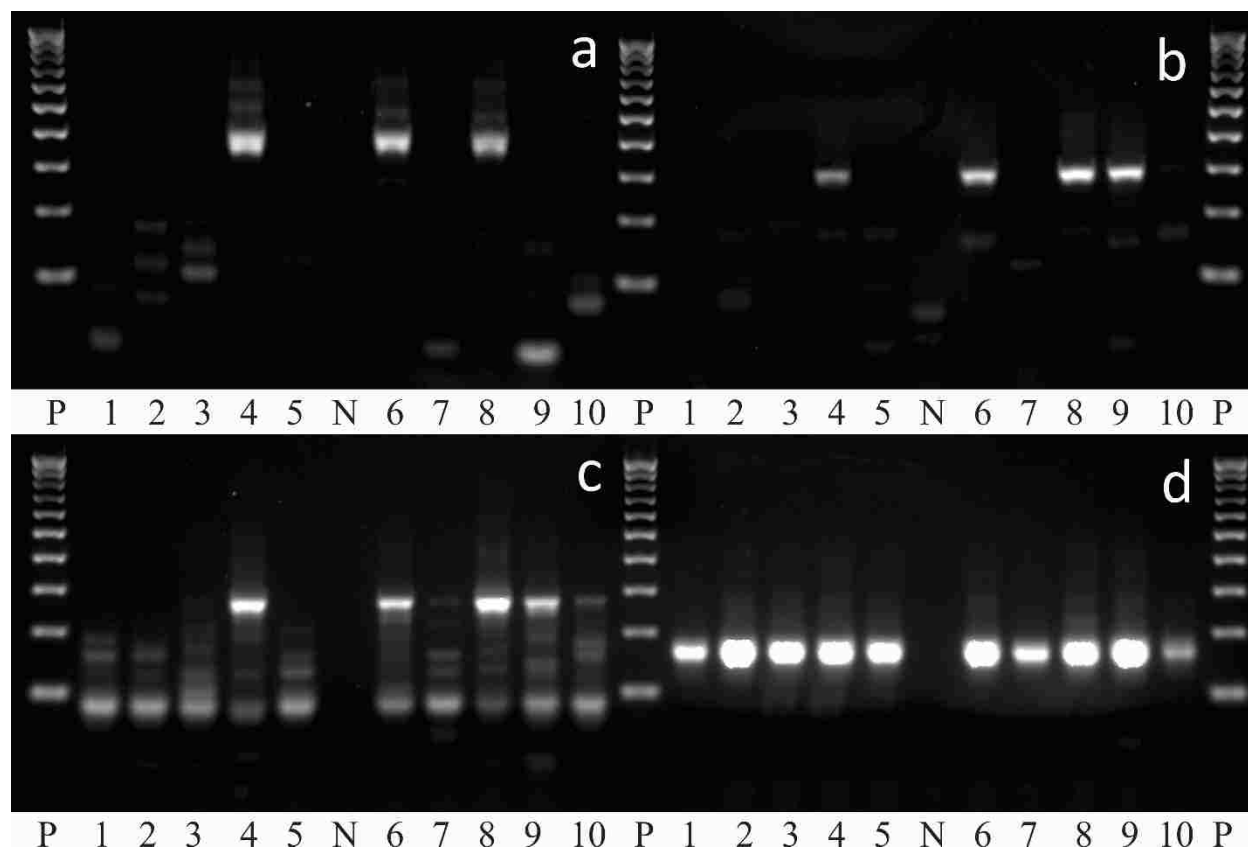


Figure 5.3 Agarose gel image of PCR products from rat brain tissue sections. Four primers: a) CYP 11b2 (376 bp); b) Snn1g 1 (298 bp); c) Snn1g 3 (281 bp); d) Snn1g 2 (168 bp). Numbers 1-10 indicate samples; P indicates PCR Molecular Ruler; N indicates negative control.

The number of cells ablated in these experiments was relatively low; thus, the small quantity of DNA captured (~1-12 ng) presented a challenge for extraction. It was unclear initially whether commercial DNA extraction kits had the capability to process such low levels of DNA. Thus, the efficiency of five commercial kits with laser-ablated samples was tested: two bead-based methods (ZymoBead Genomic DNA kit<sup>300</sup> and MagneSil Genomic Fixed Tissue System<sup>301</sup>); and three column-based methods (ZR Genomic DNA,<sup>302</sup> Quick Universal Miniprep,<sup>303</sup> and Quick-gDNA Microprep<sup>304</sup>). Spots with an area of 1 mm<sup>2</sup> were collected from five consecutive rat kidney tissue sections at a fluence of 20 kJ/m<sup>2</sup>. The samples were pooled to create a master sample, which was mixed and divided into aliquots. Five aliquots per kit were used as technical replicates to test

the ability of each kit to yield purified DNA material from laser ablated and captured samples. DNA was quantified using a fluorometer and the same protocol used for the transfer efficiency experiments.

All five kits provided usable amounts of DNA from the ablated samples, indicating that a specialized DNA extraction method is not needed to process such samples. However, the three column-based kits provided higher recoveries, averaging ~1.7 ng (ZR Genomic DNA kit,  $1.5 \pm 0.1$  ng; Quick-gDNA Microprep,  $1.6 \pm 0.2$  ng ( $n=4$ ); and, Quick Universal Miniprep,  $2.0 \pm 0.3$  ng), than the two bead-based approaches, which averaged only ~0.45 ng (ZymoBead,  $0.3 \pm 0.1$  ng; MagneSil,  $0.6 \pm 0.2$  ng). With regard to the bead-based kits, the results for the MagneSil kit could be substantially improved if the protocol included the use of a rotator during the bead-incubation; using the manufacture's protocol, the magnetic MagneSil beads immediately sank to the bottom of the assay tube, limiting their contact with the suspended DNA. By contrast, improvements are less obvious for the non-magnetic ZymoBeads because they tended to slide down the tube wall during pipetting steps, which necessitated leaving more supernatant behind.

For each kit, the variance in DNA recovered from nearby spots on the same tissue section was also assessed. Here, from the same five sections noted above, 15 different areas on each section were ablated and captured at  $20 \text{ kJ/m}^2$ . All kits showed a similar pattern of varying DNA recoveries across the tissue section, even though the technical replicates (see above) indicated fairly high precision for recovery from each kit. For example, Figure 5.4 shows that the quantity of purified DNA obtained by the Quick Universal Miniprep from each location ranged from 1 to 12 ng. These data show that the ablation-capture technique is robust with regard to obtaining usable quantities of DNA regardless of where ablation occurs on the tissue section.

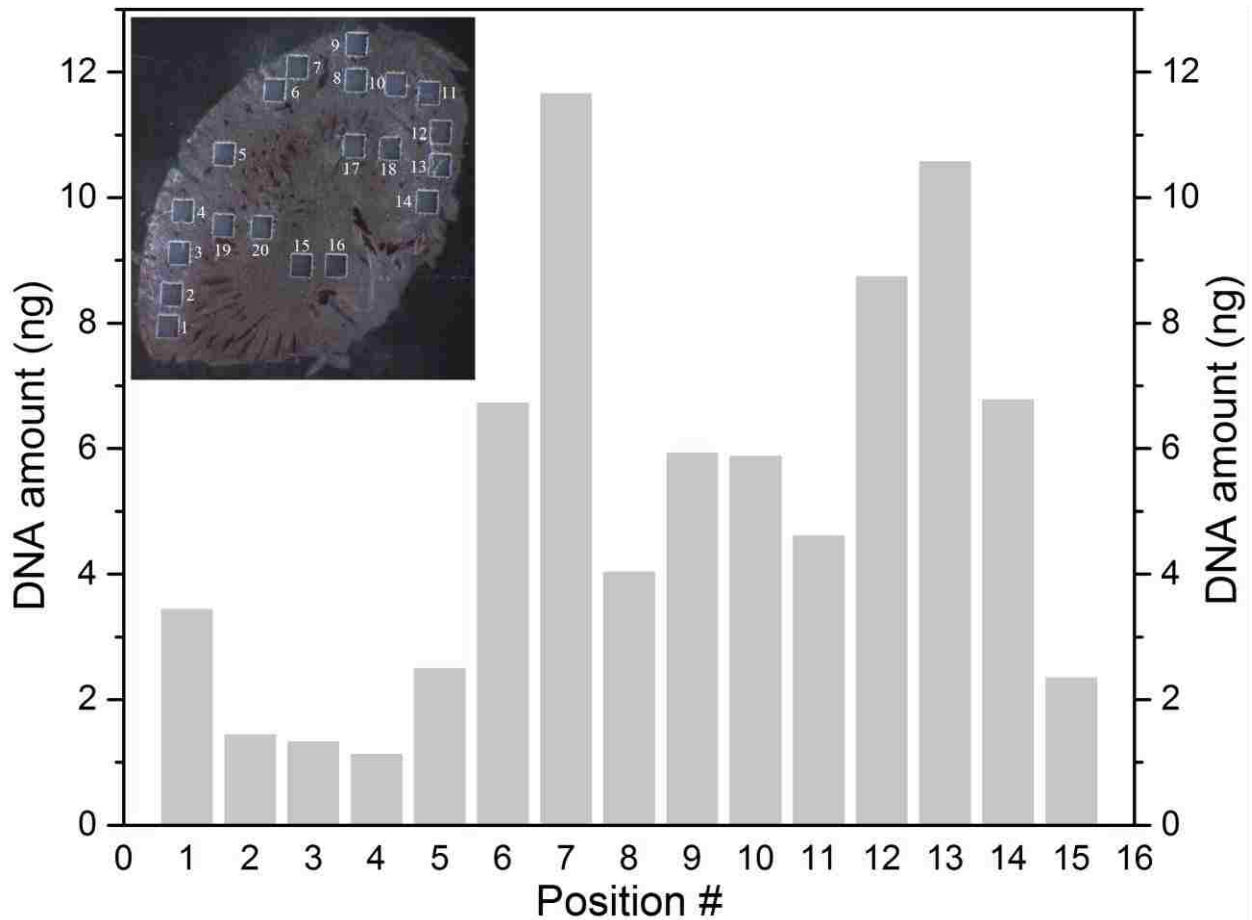


Figure 5.4 DNA recovered with the Quick Universal Miniprep kit. Top insert is an image of the rat kidney section after laser ablation. Positions 16 to 20 were used for the multiple kit evaluation experiments.

Finally, four samples ablated from consecutive rat kidney tissue sections at 20 kJ/m<sup>2</sup> were PCR-amplified before and after extraction with the Quick Universal Miniprep kit (Figure 5.5). Prior to DNA extraction, none of the samples produced detectable PCR product (left lane in each bracket); however, after DNA extraction, all samples displayed bands of the expected size. This result is consistent with the prior PCR results for rat brain tissue (Figure 5.3) because these samples were obtained from much smaller areas (1 mm<sup>2</sup> vs. 4 mm<sup>2</sup> areas). Again, the PCR results with ablated tissue indicates that PCR assays will benefit from further purification of the DNA in the ablated sample.

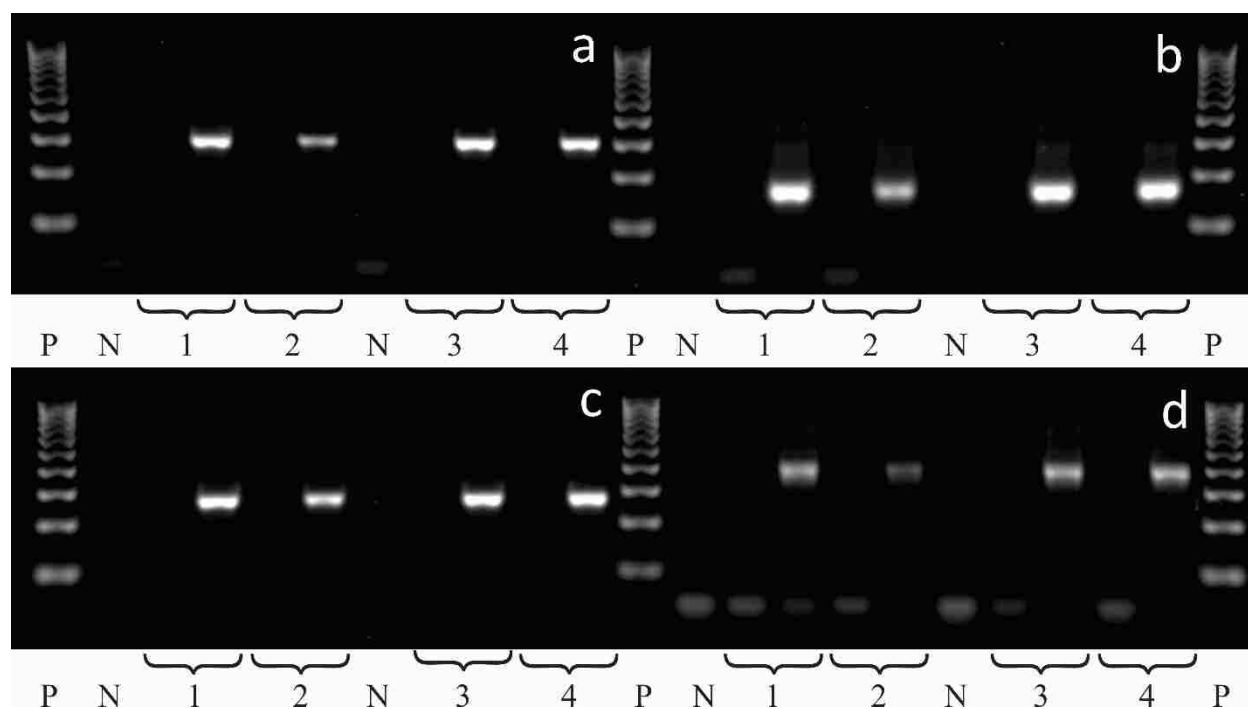


Figure 5.5 Agarose gel image of PCR products from rat kidney sections. Lane pairs 1-4 indicate samples. The left lane indicates sample without extraction and the right lane indicates sample with extraction. P indicates PCR Molecular Ruler; N indicates negative control.

#### 5.4. SUMMARY

IR laser ablation sample transfer of DNA was evaluated using Sanger sequencing and PCR amplification. To determine the optimum ablation fluence, the 3  $\mu\text{m}$  mid-IR laser was used to ablate plasmid DNA template. At high laser fluences (36  $\text{kJ}/\text{m}^2$ ), the ablation resulted in damage of the recovered DNA, whereas the DNA was transferred intact and undamaged at lower fluences ( $\leq 24 \text{ kJ}/\text{m}^2$ ). For the plasmid DNA, the transfer efficiency was estimated to be  $59 \pm 3\%$ .

Ablation and transfer of intact DNA from rat tissue samples was achieved. PCR experiments demonstrated that further purification of DNA from laser ablated and captured samples is required to ensure consistent PCR results. However, experiments with five different commercial DNA extraction kits, with yields of  $\sim 1\text{-}12 \text{ ng}$  from  $1 \text{ mm}^2$  areas, demonstrated that no

special extraction method is required. Following purification, four regions on two different genes for all the tested samples were amplified.

This work expands the sampling capabilities of IR laser ablation, demonstrating that DNA, as well as proteins, can be isolated from tissue samples for further assays. Future experiments will be directed at providing a comprehensive tool for localized “-omics” investigations.

## CHAPTER 6 RNA SAMPLING FROM TISSUE SECTIONS USING IR LASER ABLATION FOR QUANTITATIVE PCR\*

This chapter describes the work to remove RNA material from discrete locations of frozen rat brain tissue sections using an IR laser at a wavelength at 3- $\mu\text{m}$  in transmission geometry. The ablated plume was captured in a microcentrifuge tube containing RNase-free buffer and processed using a commercial RNA purification kit. RNA transfer efficiency and integrity were evaluated based on automated electrophoresis in microfluidic chips. Using purified RNA, reproducible IR-laser ablation of intact RNA was demonstrated with a transfer efficiency of  $72\pm 12\%$  at laser fluences of 3-5  $\text{kJ}/\text{m}^2$ . For tissue sections, RNA was transferred with an efficiency of  $79\pm 14\%$  using a laser fluence of 13  $\text{kJ}/\text{m}^2$ . RNA integrity was  $>90\%$  of its original RIN value ( $\sim 7$ ) and the purified RNA could be used for a qPCR assay.

### 6.1. INTRODUCTION

Ribonucleic acid (RNA) is the link between the transcription of DNA and the expression of proteins,<sup>305-306</sup> and can reveal or modify biological function throughout the protein synthesis process.<sup>307-308</sup> As such, RNA biomarkers can be used for detection of a disease even before expression of the associated proteins. RNA-based therapeutics can alter the production of aberrantly expressed proteins. With the increasing availability of high-throughput RNA analysis techniques such as quantitative polymerase chain reaction (qPCR),<sup>309-310</sup> microarray assays,<sup>311</sup> and

---

\* Some portions of the work reported in this chapter previously appeared as Wang, K., Donnarumma, F., Herke, S. W., Dong, C., Herke, P. F., & Murray, K. K. (2019). RNA Sampling from Tissue Sections using Infrared Laser Ablation. *Analytica Chimica Acta*. Reprinted by permission of Elsevier.

next generation sequencing,<sup>4, 312-314</sup> analyzing RNA extracted from tissue is becoming more valuable in disease diagnosis, prognosis, and drug development.<sup>315-318</sup>

Analyte extraction and purification influences both the quantity and the integrity of RNA and plays a critical role in the accuracy and reproducibility of high throughput RNA analysis.<sup>163-171</sup> Isolation and purification of RNA generally starts with tissue homogenization and cell lysis. For instance, tissue samples may be snap-frozen, pulverized into powder, and extracted with guanidinium thiocyanate and phenol-chloroform mixtures.<sup>319-320</sup> Alternatively, fresh or frozen tissue may be immersed in an RNA-stabilizing buffer and homogenized by vortexing or bead-beating.<sup>321-322</sup> The RNA can then be purified using a variety of in-house developed protocols or commercial RNA extraction kits.<sup>323-329</sup>

Frozen or formalin-fixed paraffin embedded (FFPE) tissue is a common clinical sample type, and it is often critical to obtain RNA from a particular region of cells within a block. In this context, analysis of RNA presents challenges in maintaining analyte integrity as well as spatial localization.<sup>39</sup> First, the sampling method must overcome the usual obstacles to the extraction of high-quality RNA such as tissue types recalcitrant to homogenization or rich in co-purifying biomolecules (lipids, proteins, DNA) as well as degradation by ribonucleases (RNase).<sup>323-324, 330-331</sup> RNases are of particular concern because they can rapidly digest the RNA and are ubiquitous in tissue and the environment; therefore, fast sample processing and an RNase-free work area are critical.<sup>170-171, 332</sup> Second, the sampling method must permit analysis of multiple RNA targets from a limited number of cells in the specific region of interest.<sup>13, 39</sup> To date, most sampling methods cannot fully resolve these issues simultaneously. For instance, nuclease-integrity can be assured by immediately immersing an entire tissue section in an RNA-stabilizing buffer and then

homogenizing the tissue by bead-beating, but this merges the transcriptomes from all cells in the section.<sup>171</sup> Alternatively, single cell technologies can prevent the merging of transcriptomes, but each cell's original location within the tissue section is unknown.<sup>13, 87, 333-334</sup> Finally, techniques such as *in situ* hybridization<sup>28</sup> and *in situ* sequencing<sup>29</sup> can sample specific cells, but are limited in the number of RNA targets that can be assessed at one time.<sup>28, 39</sup>

Laser capture microdissection (LCM) is an established method for excising localized regions of interest (ROI) from tissue sections for RNA extraction from as little as a few cells.<sup>67, 335</sup> With infrared LCM, the laser melts a thermoplastic film in contact with the tissue, causing it to stick to the film and allowing separation of the ROI from the remaining tissue.<sup>80</sup> With ultraviolet LCM, the laser ablates the border of the ROI and the tissue is detached from the slide with a defocused pulse.<sup>80</sup> The dissected material can be captured in a microfuge tube either cooled or containing a buffer for RNA stabilization or extraction.<sup>78-81</sup> Sampling time for LCM varies from 20 minutes to 1 h, depending on number of cells, tissue type, and type of microscope slide used.<sup>41, 67, 89-90</sup>

Infrared (IR) laser ablation can be used to excise ROI from tissue sections with direct collection in an appropriate biomolecule-stabilizing buffer. IR lasers operating at a 3- $\mu\text{m}$  wavelength ablate tissue efficiently due to the overlap with the OH-stretch of abundant biomolecule (e.g.,  $\text{H}_2\text{O}$ ),<sup>95, 102, 336</sup> and the method was used to sample tissues for large biomolecules such as proteins,<sup>41, 98, 266</sup> biologically active enzymes,<sup>336-337</sup> and DNA.<sup>338</sup> Several characteristics of IR laser ablation may be particularly useful for RNA analysis of clinical samples: disruption of connective tissue and membranes permits RNA purification without a separate cell lysis step;<sup>41,</sup>

<sup>337-338</sup> and, 1 mm<sup>2</sup> regions can be sampled in under 60 s.<sup>41</sup> Thus, IR laser ablation combines sample localization with rapid sampling of the ROI.

In this work, IR laser ablation and capture was used to collect RNA from tissue. Thin fresh-frozen tissue sections of rat brain were ablated at various laser fluences, and the RNA integrity, total RNA recovery, and sample transfer efficiency for the collected material was determined. Finally, RNA obtained by IR laser ablation was analyzed with a simple qPCR assay.

## **6.2. EXPERIMENTAL**

For ablation of purified RNA, 1  $\mu$ l (1  $\mu$ g/ $\mu$ l) of human kidney total RNA was deposited on a microscope slide and vacuum-dried (1 min) prior to laser ablation. The ablated material was captured in RNA storage solution (1 mM sodium citrate, pH 6.4 $\pm$ 0.2), and the samples were stored at -80°C prior to analysis. For tissue sections, the ablated material was captured in DNA/RNA Shield solution for stabilization of nucleic acids at room temperature; samples were stored at room temperature for up to one week until further analysis.

Human kidney RNA samples were loaded on the Bioanalyzer chip with no further purification. The tissue samples (ablated and positive control) were first purified using the Direct-zol RNA MicroPrep kit. The purification procedure was modified to minimize salt-carryover into the eluted sample. Without these modifications, the salt concentration exceeded the maximum allowed for the RNA 6000 Pico kit due to the relatively large sample volume.

Briefly, the ablated tissue was captured in 200  $\mu$ l of DNA/RNA Shield solution and transferred to a 0.5-ml tube and digested with Proteinase K (30 min, 55°C). Following centrifugation to pellet cellular debris, the cleared supernatant was transferred to a 2.0-ml tube containing ~800  $\mu$ l of TRI-reagent and rotated in a 30°C oven (5 min). Following the addition of

1 mL of 100% ethanol, the tubes were briefly rotated in the oven to ensure thorough mixing. For each sample, a spin-column (Zymo IC, designed for low elution volumes) was loaded and centrifuged three times to filter the entire 2000  $\mu$ l of RNA extraction reagents. Unless otherwise noted, centrifugation was performed at 15,000 rcf and limited to 15 s to prevent column drying, which can increase the salt in the final elution. Following the application of RNA wash buffer (400  $\mu$ l, 30 s), an in-column DNase I digestion was performed (30°C, 15 min). After two applications of pre-wash buffer (400  $\mu$ l), RNA wash buffer was applied three times (350  $\mu$ l, 700  $\mu$ l, and 350  $\mu$ l) to completely remove salt from the samples. After discarding the final flow-through, columns were centrifuged for 60 s to fully remove the RNA wash buffer. Finally, samples were eluted in 15  $\mu$ l nuclease-free water (60 s, 10,000 rcf) and stored at -80°C.

Positive controls were generated by directly placing a frozen rat tissue section (~1 mg) into 200  $\mu$ L of DNA/RNA Shield solution. These samples were initially homogenized by brief vortexing and then completely homogenized in ZR BashingBead lysis tubes. Following centrifugation, the supernatants was transferred to 0.5 mL tubes and processed with the same workflow as the ablated samples.

For choosing the optional capture buffers, RNA integrity was assessed by comparing the relative heights for the peaks associated with the ribosomal subunit 18S and 28S in control vs. laser ablated samples. However, the 28S:18S peak ratio can be a highly variable metric.<sup>150-151</sup> Thus, RNA concentration and integrity for all other experiments were assessed using an Agilent Bioanalyzer 2100 with a RNA 6000 Pico Kit.

Captured and purified RNA was reverse transcribed (SuperScript III) into cDNA. Samples were analyzed in triplicate by qPCR on a real-time PCR system (QuantStudio 6 Flex) using 22- $\mu$ l

reaction volumes: 10  $\mu$ l of 1X SYBR Select Master Mix; 1  $\mu$ L each forward and reverse primer (10  $\mu$ M, Table 6.1); and, 10  $\mu$ l of cDNA template. Cycling parameters were: 1 cycle at 50°C (2 min); 1 cycle at 95°C (10 min); and, 40 amplification cycles of 95°C (15 s) and 60°C (1 min). The specificity of the amplified product was assessed by a melt curve analysis.

Table 6.1 Primer information

Name	Forward (upper)	Reverse (lower)
glyceraldehyde-3-phosphate dehydrogenase (GPDH)	GAAGGTCGGTGTGAACGGATT	TGGAACATGTAGACCATGTA GTTGAG
myelin basic protein (MBP)	AAG TCG CAG AGG ACC CAA GA [1]	GGG TGT ACG AGG TGT CAC AAT GT

### 6.3. RESULTS

Initial experiments were performed to determine whether RNA could be captured intact using IR laser ablation and to quantify the ablation and capture efficiency. To assess RNA integrity, a commercially-purified stock of RNA (isolated from human kidney) was ablated at laser fluences ranging from 3 to 11 kJ/m<sup>2</sup>. For the positive control, a 1  $\mu$ l aliquot of the RNA was added to 200  $\mu$ l of RNA storage solution. Bioanalyzer data for the ablated and control RNA samples were compared with regard to their RNA integrity number (RIN) and their electrophoretic traces. Representative electropherograms are shown in Figure 6.1. 5S ribosomal RNA peaks present from 23-28 s, 18S peak presents at 40 s and 28S present at 48 s of the electropherograms.

Initially, a tris-EDTA buffer (10 mM Tris, 0.05 mM EDTA, ~pH 8) was used as the capture buffer; however, the 28S peaks were consistently smaller than the 18S peaks when these samples were processed on the Bioanalyzer. By contrast, ablated samples captured in RNA storage solution

typically displayed 28S peaks of equal or greater intensity than the 18S peaks, indicating that this buffer promotes greater RNA stability than does the tris-EDTA buffer.

RIN values were comparable between the positive control (RIN  $8.8 \pm 0.4$ ) and RNA ablated at low fluences ( $3 \text{ kJ/m}^2$ , RIN  $8.6 \pm 0.2$ ; and,  $5 \text{ kJ/m}^2$ , RIN  $8.1 \pm 0.2$ ); however, RIN values were ~30% lower for samples ablated at 7 and  $9 \text{ kJ/m}^2$  (RIN  $6.8 \pm 0.1$  and  $6.3 \pm 0.4$ , respectively). At  $11 \text{ kJ/m}^2$ , fluorescence readings from the small RNA region of the electropherogram were extremely high, resulting in a RIN estimate of “N.A.” (not available). Manually increasing the threshold value<sup>151, 339</sup> for the “5S Region Anomaly Threshold” from 0.5 (default setting) to 0.62 resulted in a RIN of  $4.5 \pm 0.4$ , which was ~50% lower than RIN for the positive control.

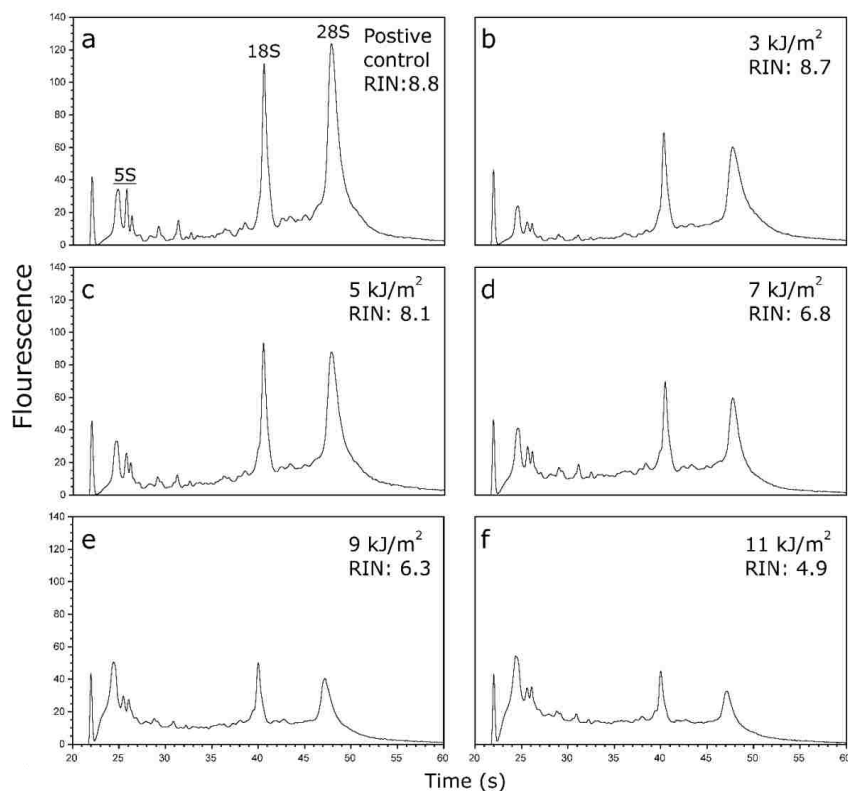


Figure 6.1 Agilent Bioanalyzer electropherograms of purified human kidney total RNA comparing RNA integrity number (RIN) values for a positive control (a) with RNA collected by infrared laser ablation at five different fluences (b-f: 3, 5, 7, 9, &  $11 \text{ kJ/m}^2$ ).

To summarize, with purified RNA, laser fluences of  $\leq 5$  kJ/m<sup>2</sup> generated RIN and electropherograms similar to those of the positive control sample. By contrast, corresponding data for RNA obtained at laser fluences  $\geq 7$  kJ/m<sup>2</sup> demonstrated that higher laser fluences caused degradation (i.e. fragmentation) of the purified RNA, although the RIN estimates ( $>5$ ) indicated that the RNA could still be used for qPCR.<sup>194-195</sup> As such, RNA appears to be more sensitive to IR laser ablation than was found for DNA, where a laser fluence of 24 kJ/m<sup>2</sup> did not influence purified plasmid DNA integrity.<sup>338</sup> These results may reflect the greater stability of double-stranded DNA compared to single-stranded RNA.<sup>340</sup>

As assessed with the Bioanalyzer, recovery of high-quality purified RNA was the highest at 5 kJ/m<sup>2</sup>, and then progressively decreased with increasing fluences. Here, fluorescence readings from the entire electrophoretic trace (full trace) were compared with those from just the 18S and 28S subunit (Figure 6.2). Both metrics indicated that increasing the laser fluence from 3 to 5 kJ/m<sup>2</sup> resulted in higher RNA recovery. By contrast, as the fluence increased from 7 to 11 kJ/m<sup>2</sup>, RNA recovery appeared to increase by the full trace metric whereas it decreased by the 18S/28S peak metric. These results reflect the fact that, upon degradation, 18S and 28S ribosomal RNA shifts towards the 5S region (Figure 6.1(d, f)) where the degraded fragments are retained in the calculation of total RNA.

Table 6.2 RNA recovery as a function of laser fluence

Laser Fluence (kJ/m <sup>2</sup> )	RNA (μg), full trace	RNA (μg), 18S & 28S peaks
3	0.50±0.09	0.17±0.02
5	0.67±0.06	0.19±0.02
7	0.72±0.11	0.11±0.02
9	0.77±0.01	0.10±0.01
11	0.88±0.06	0.07±0.01
Positive control	0.83±0.19	0.30±0.02

Transfer efficiency can be defined as the ratio of the quantity of material captured to the quantity originally deposited. To assess the capture efficiency, a 1 μg quantity of RNA in 1 μL of sodium citrate (pH 6.8) was deposited on a microscope slide and completely ablated into 200 μl of capture buffer. For the control, 1 μg of RNA was added to 200 μl of capture buffer. Transfer efficiency was quantified using Bioanalyzer data for samples ablated at fluences of 3 and 5 kJ/m<sup>2</sup> because they produced RIN similar to those of controls. The average transfer efficiency for purified RNA ranged from 72±12% (full trace) to 60±6% (18S/28S subunits). The RNA transfer efficiency determined here is similar to the IR laser ablation transfer efficiency determined for DNA (59±3)<sup>338</sup> and enzymes (75±8).<sup>337</sup>

After demonstrating that RNA can be ablated and captured intact, IR-laser ablation and capture of RNA from tissue was tested. Consecutive rat brain tissue sections were used to evaluate the quality of the total RNA after laser ablation. A rat brain was sectioned along the frontal plane at a thickness of 50 μm, and consecutive sections were thaw-mounted on microscope slides for laser-ablation (samples) or placed in tubes immersed in dry ice (controls); all slides and controls were then stored at -80°C. For the ablation experiments, TRI-Reagent was initially used as the

capture buffer; however, the 28S peaks were consistently smaller than the 18S peaks. Ultimately, DNA/RNA Shield solution was used as the capture buffer because it maintained a more intense 28S peak (vs. the 18S peak), which indicates better preservation of RNA. Tissue sections (~20 mm<sup>2</sup> each, estimated in ~1 mg) mounted on microscope slides were ablated in their entirety using a laser fluence of 13 kJ/m<sup>2</sup>; visual inspection of the slides indicated that 13 kJ/m<sup>2</sup> was the minimum laser fluence required for complete tissue ablation. Concurrently with the ablated samples, control samples were homogenized in DNA/RNA Shield solution using a bead-beating protocol (Section 2.3).

The entire volume of each ablated and control sample was purified with the Direct-zol RNA MicroPrep kit. Prior to analysis, the purified samples were diluted in nuclease-free water to bring them into the Bioanalyzer quantitation range. Control samples processed with the bead-beating method had a RIN of  $7.4 \pm 0.3$ , whereas ablated and captured RNA had a RIN of  $6.8 \pm 0.3$  (Figure 6.2). RNA concentrations were calculated with the area under the curve method using both the full electrophoretic trace as well as the signal only for 18S and 28S subunits. Transfer efficiencies ranged from  $79 \pm 14\%$  for the full trace ( $649 \pm 100$  ng vs.  $515 \pm 93$  ng) to  $71 \pm 7\%$  for the 18S-28S peaks ( $245 \pm 8.6$  ng vs.  $174 \pm 18$  ng).

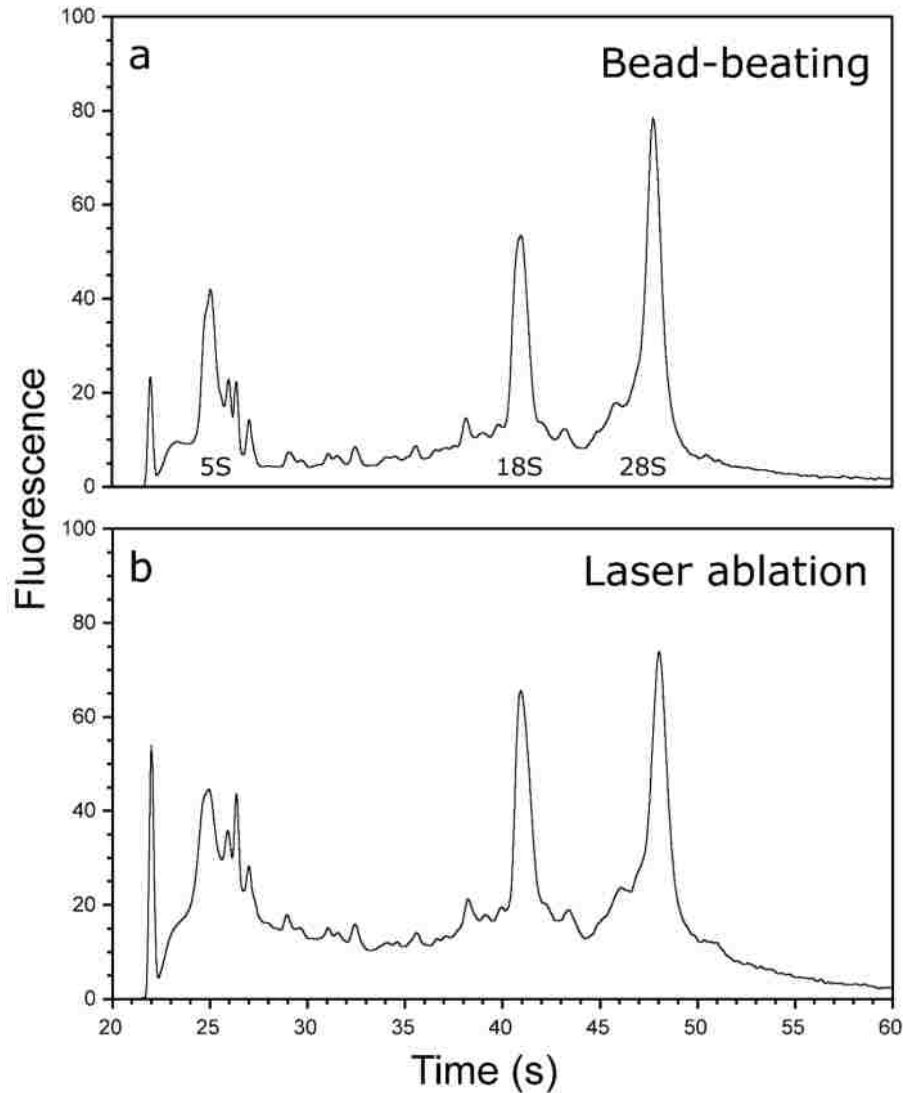


Figure 6.2 Representative electropherograms of RNA from 20-mm<sup>2</sup> regions of paired consecutive 50  $\mu$ m tissue sections. (a) Positive control (RIN  $7.4 \pm 0.3$ ): purified RNA was diluted ~15-fold. (b) Infrared laser ablation (RIN  $6.8 \pm 0.3$ ): purified RNA was diluted ~8-fold.

RNA samples with RIN > 5 have been analyzed with microarray assays, qPCR, and RNA sequencing.<sup>194-195, 197-199, 341</sup> In the results described above, RNA from ablated tissue sections had a RIN of ~7, representing only an 8% decrease compared with results for the conventional bead-beating method. This RIN is generally consistent with RIN values reported previously for LCM, although results for LCM vary greatly depending on sampling conditions.<sup>78, 89, 335, 342-353</sup> Complete

ablation occurred with 3-5 kJ/m<sup>2</sup> for purified RNA; however, 13 kJ/m<sup>2</sup> was required to completely ablate rat brain tissue sections. Nevertheless, at their respective laser energies, the captured RNA for both sample types had RIN values of ~7 and the associated electropherograms were similar (Fig. 1). It is possible that the higher amount of water present in the tissue allows the use of higher laser energies, which are required to overcome the tensile strength of the tissue itself, without compromising the stability of the RNA.<sup>202</sup>

Finally, to augment the Bioanalyzer results, qPCR was used to assess the compatibility of laser-ablated RNA with downstream assays. RNA was laser-ablated from two discrete regions of rat brain tissue sections (Figure 6.3). Location 1 comprised two 4-mm<sup>2</sup> crescents covering the corpus callosum region and location 2 comprised a 3-mm<sup>2</sup> circle in the hypothalamus region. Following purification, the ablated RNA had intense 18S/28S peaks and good overall integrity (Location 1, RIN 7.4; Location 2, RIN 7.3). For qPCR, two sets of primers targeting two different genes were used. One primer was designed for the house-keeping gene glyceraldehyde-3-phosphate dehydrogenase. The other primer targeted myelin basic protein (MBP), an important protein in the process of myelination of nerves in the nervous system. For both locations and both genes, the cDNA produced from the RNA generated Ct values between ~22-28 cycles (Figure 6.3a) and melt curves which indicated that each primer pair produced a single, specific final product (Figure 6.3b).

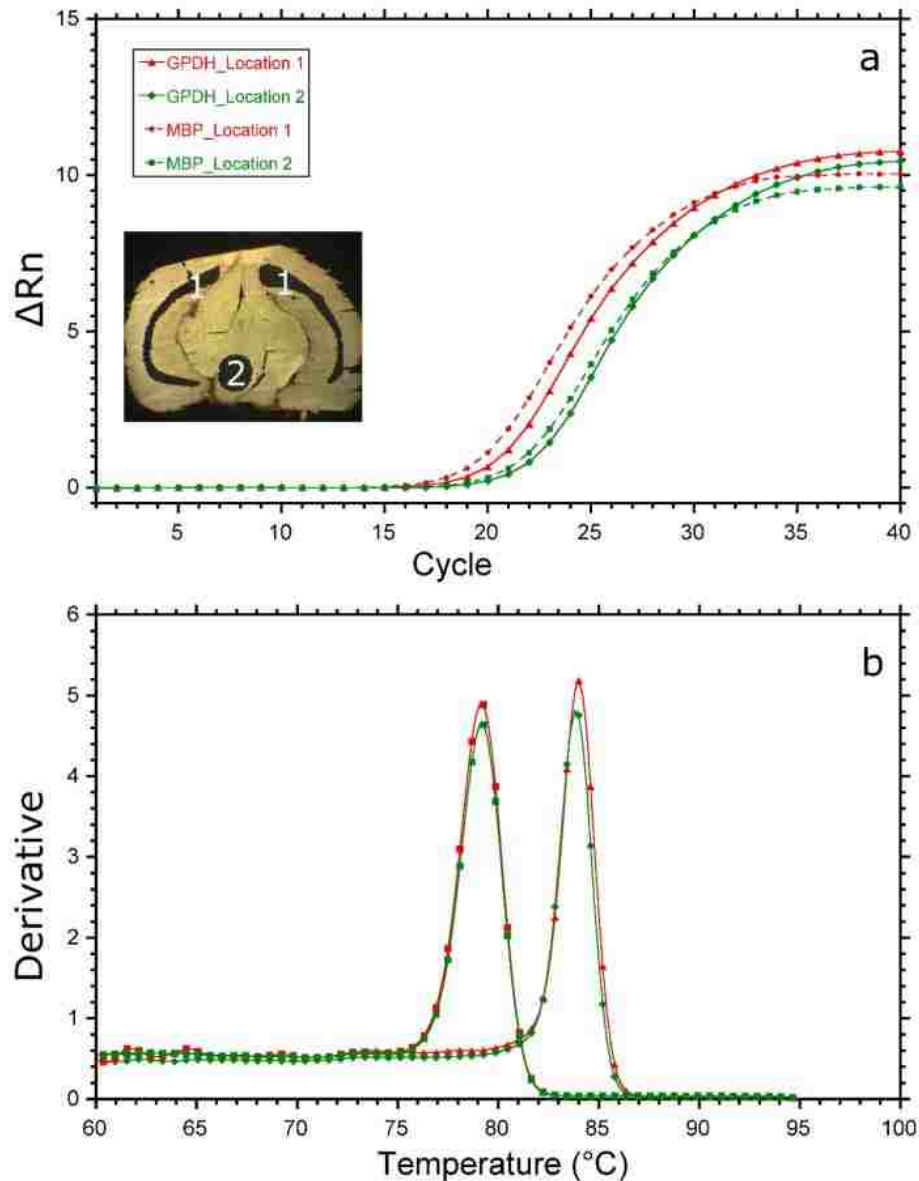


Figure 6.3 Analysis by qPCR of RNA derived from two locations (a, insert): Location 1, two 4-mm<sup>2</sup> crescents; Location 2, 3-mm<sup>2</sup> circle. a – amplification curves; b – melt curves for two genes (MBP; GPDH).

#### 6.4. SUMMARY

IR laser ablation was used to sample RNA from rat tissue sections. Using a fluence of 13 kJ/m<sup>2</sup>, the transfer efficiency of RNA from rat tissue sections was 79%. the RNA integrity was >90%

of its original RIN value (~7) and the RNA performed well in a qPCR assay. Finally, RNA samples were acquired from discrete sample locations at a sub-mm scale laser precision.

These findings add RNA to the list of biomolecules, such as proteins, active enzymes, and DNA, that are amenable to sampling by IR laser ablation. Because the method combines micron spatial resolution with rapid sampling that completely disrupts tissue, IR laser ablation is particularly suitable for the molecular analysis of clinical tissue samples. Thus, when sampling at a sub-millimeter spatial resolution is sufficient, IR laser ablation may be a desirable option. Future experiments will be directed at integrating transcriptomics, genomics and proteomics from the same sample using laser-ablation.

## CHAPTER 7: CONCLUSIONS AND FUTURE DIRECTIONS

In this dissertation, the development of IR laser ablation for sampling material from tissue sections for biomolecule analysis was described. The significance of this work lies on the ability of IR laser to ablate proteins, enzymes, DNA and RNA intact at sub-millimeter resolution from tissue sections. An IR OPO system at a wavelength of 3  $\mu\text{m}$  was focused on samples mounted on a microscope slide for laser ablation. The ablated material was captured by a microcentrifuge tube mounted 5 mm below the microscope slide and analyzed by mass spectrometry, Sanger sequencing, electrophoresis, PCR and qPCR.

In the work described Chapter 1, tissue sections were imaged using a MALDI TOF MS to identify ROI based on localized signal intensity. Mid-infrared laser ablation sampling was used to sample the ROI on the same section. After determining the ROI by overlaying the MS imaging generated heat-map, the section is sampled using IR laser ablation and custom stage-control software. The ability of sampling arbitrary shapes from tissue sections using IR laser sampling was demonstrated. The IR sampling process can be guided by imaging. Masses of identified proteins and the corresponding sampling location were used to improve identification of MALDI imaging peaks. Comparison of cellular localization and activity of the proteins from the different regions was performed using GO ontology analysis.

The ability of IR laser sampling of enzymes from tissue while maintaining enzyme activity was demonstrated in the work described in Chapter 4. Initial experiments were performed on trypsin and catalase thin film to qualitatively assess the presence of enzymatic activity after IR laser ablation using fluorimetric analysis. Around 75% transfer efficiency was achieved.

Approximately one-third of the captured trypsin and one-half of the captured catalase retained enzyme activity. The effect of IR laser ablation on the activity of enzymes captured from tissue was studied using thin tissue sections. The enzyme catalase was ablated and captured from rat brain tissue and the measured activity was consistent with that anticipated for the different regions of the brain.

In the work described in Chapter 5, an IR laser was used to ablate DNA from tissue section. The transfer efficiency and the molecular integrity of the captured DNA was evaluated using Sanger sequencing, gel electrophoresis, and fluorimetric analysis. Initial experiments were performed on a 3200-bp double-stranded plasmid DNA template. It was found that intact DNA was reproducibly transferred with an efficiency of  $59\pm 3\%$  at laser fluences below  $20 \text{ kJ/m}^2$ . However, when the laser fluence was  $36 \text{ kJ/m}^2$ , DNA may have either fragmented the DNA or damaged individual nucleotides. IR laser ablation was used to ablate and capture DNA from rat tissue sections and the extracted DNA was amplified by PCR. All samples produced PCR products of the expected size.

Previously, IR laser ablation and transfer at  $3 \mu\text{m}$  was used to isolate proteins, enzymes, and DNA from rat tissue sections. In the work described in Chapter 6, it was shown that the technique is also suitable for RNA analysis. Initial experiments were performed using human kidney RNA to determine whether RNA could be captured intact using IR laser ablation and to quantify the ablation and capture efficiency. A laser fluence of  $\leq 5 \text{ kJ/m}^2$  had no discernible effect on the integrity of the RNA. RNA obtained from laser fluences between 5 to  $7 \text{ kJ/m}^2$  showed degradation, but still can be used for qPCR. A laser fluence of  $13 \text{ kJ/m}^2$  was used to sample RNA

from tissue. 79% transfer efficiency was obtained. RNA integrity obtained from laser ablation was comparable to that derived from positive controls and mRNA was quantified using qPCR.

One of the future directions is improving the spatial resolution of material transfer using a reflective objective with a high numerical aperture and long working distance. The reflective objective contains a 100 mm diameter concave mirror and 25 mm diameter convex mirror. The Schwarzschild objective has only reflective elements, so it is achromatic and focuses all wavelengths equivalently. Using this system, a laser spot 10  $\mu\text{m}$  in diameter was achieved from tissue sections at thickness of 5  $\mu\text{m}$ , which allow the borders of ROI to be selected at single cell level. The Schwarzschild objective has a working distance of 98 mm. The system can be used for transmission geometry or reflectron geometry.

A second direction will focus on utility of this technique to formalin-fixed paraffin-embedded (FFPE) tissue specimens for protein, enzyme, DNA and RNA analysis. This has the potential to make tissue archival libraries more accessible to molecular biomarkers analysis.

A third direction will focus on multi-omics analysis. MALD MSI is used to determine the ROI from tissue sections. The ROI from same or consecutive tissue sections are ablated and transferred. The proteins, metabolites, enzymes, DNA and RNA from single samples are analyzed and bioinformatics analysis can be achieved.

## REFERENCES

1. Mamas, M.; Dunn, W. B.; Neyses, L.; Goodacre, R., The role of metabolites and metabolomics in clinically applicable biomarkers of disease. *Arch. Toxicol.* **2011**, *85*, 5-17.
2. Zen, K.; Zhang, C. Y., Circulating microRNAs: a novel class of biomarkers to diagnose and monitor human cancers. *Med. Res. Rev.* **2012**, *32*, 326-348.
3. Lee, S.; Xie, J.; Chen, X., Peptides and peptide hormones for molecular imaging and disease diagnosis. *Chem. Rev.* **2010**, *110*, 3087-3111.
4. Byron, S. A.; Van Keuren-Jensen, K. R.; Engelthaler, D. M.; Carpten, J. D.; Craig, D. W., Translating RNA sequencing into clinical diagnostics: opportunities and challenges. *Nat. Rev. Genet.* **2016**, *17*, 257-271.
5. Dasari, S.; Wudayagiri, R.; Valluru, L., Cervical cancer: Biomarkers for diagnosis and treatment. *Clin. Chim. Acta* **2015**, *445*, 7-11.
6. Ziegler, A.; Koch, A.; Krockenberger, K.; Großhennig, A., Personalized medicine using DNA biomarkers: a review. *Hum. Genet.* **2012**, *131*, 1627-1638.
7. Nilsson, A.; Fehniger, T. E.; Gustavsson, L.; Andersson, M.; Kenne, K.; Marko-Varga, G.; Andrén, P. E., Fine mapping the spatial distribution and concentration of unlabeled drugs within tissue micro-compartments using imaging mass spectrometry. *PLoS One* **2010**, *5*, e11411.
8. Oppenheimer, S. R.; Mi, D.; Sanders, M. E.; Caprioli, R. M., Molecular analysis of tumor margins by MALDI mass spectrometry in renal carcinoma. *J. Proteome Res.* **2010**, *9*, 2182-2190.
9. Balluff, B.; Rauser, S.; Meding, S.; Elsner, M.; Schöne, C.; Feuchtinger, A.; Schuhmacher, C.; Novotny, A.; Jütting, U.; Maccarrone, G., MALDI imaging identifies prognostic seven-protein signature of novel tissue markers in intestinal-type gastric cancer. *Am. J. Pathol.* **2011**, *179*, 2720-2729.
10. Jones, E. E.; Powers, T. W.; Neely, B. A.; Cazares, L. H.; Troyer, D. A.; Parker, A. S.; Drake, R. R., MALDI imaging mass spectrometry profiling of proteins and lipids in clear cell renal cell carcinoma. *Proteomics* **2014**, *14*, 924-935.
11. Rodriguez-Canales, J.; Hanson, J. C.; Hipp, J. D.; Balis, U. J.; Tangrea, M. A.; Emmert-Buck, M. R.; Bova, G. S., Optimal molecular profiling of tissue and tissue components: defining the best processing and microdissection methods for biomedical applications. *Pancreatic Cancer: Methods and Protocols* **2013**, 61-120.
12. Hanahan, D.; Weinberg, R. A., Hallmarks of cancer: the next generation. *Cell* **2011**, *144*, 646-674.

13. Strell, C.; Hilscher, M. M.; Laxman, N.; Svedlund, J.; Wu, C.; Yokota, C.; Nilsson, M., Placing RNA in context and space—methods for spatially resolved transcriptomics. *FEBS. J.* **2018**.
14. Chen, J.; Suo, S.; Tam, P. P.; Han, J.-D. J.; Peng, G.; Jing, N., Spatial transcriptomic analysis of cryosectioned tissue samples with Geo-seq. *Nat. Protoc.* **2017**, *12*, 566.
15. Lee, J. H., Quantitative approaches for investigating the spatial context of gene expression. *Wiley Interdiscip. Rev. Syst. Biol. Med.* **2017**, *9*.
16. Ståhl, P. L.; Salmén, F.; Vickovic, S.; Lundmark, A.; Navarro, J. F.; Magnusson, J.; Giacomello, S.; Asp, M.; Westholm, J. O.; Huss, M., Visualization and analysis of gene expression in tissue sections by spatial transcriptomics. *Science* **2016**, *353*, 78-82.
17. Kherlopian, A. R.; Song, T.; Duan, Q.; Neimark, M. A.; Po, M. J.; Gohagan, J. K.; Laine, A. F., A review of imaging techniques for systems biology. *BMC Syst. Biol.* **2008**, *2*, 74.
18. Gutiérrez, Y.; Ott, D.; Töpferwien, M.; Salditt, T.; Scherber, C., X-ray computed tomography and its potential in ecological research: A review of studies and optimization of specimen preparation. *Ecol. Evol.* **2018**.
19. Slomka, P. J.; Pan, T.; Germano, G. In *Recent Advances and Future Progress in PET Instrumentation*, Semin. Nucl. Med., Elsevier: 2016; pp 5-19.
20. Krishna, V.; Sammartino, F.; Rezai, A., A review of the current therapies, challenges, and future directions of transcranial focused ultrasound technology: advances in diagnosis and treatment. *JAMA. Neurol.* **2018**, *75*, 246-254.
21. Carril, M., Activatable probes for diagnosis and biomarker detection by MRI. *J. Mater. Chem. B* **2017**, *5*, 4332-4347.
22. Dale, B. M.; Brown, M. A.; Semelka, R. C., *MRI: Basic Principles and Applications*. John Wiley & Sons: 2015.
23. Phelps, M. E., Positron emission tomography provides molecular imaging of biological processes. *Proc. Natl. Acad. Sci. U.S.A.* **2000**, *97*, 9226-9233.
24. Bagade, S.; Fowler, K. J.; Schwarz, J. K.; Grigsby, P. W.; Dehdashti, F. In *PET/MRI evaluation of gynecologic malignancies and prostate cancer*, Semin. Nucl. Med., Elsevier: 2015; pp 293-303.
25. Hussain, T.; Nguyen, Q. T., Molecular imaging for cancer diagnosis and surgery. *Adv. Drug Deliv. Rev.* **2014**, *66*, 90-100.
26. Zhou, Z.; Lu, Z.-R., Molecular imaging of the tumor microenvironment. *Adv. Drug Deliv. Rev.* **2017**, *113*, 24-48.
27. Weissleder, R., Molecular imaging in cancer. *Science* **2006**, *312*, 1168-1171.

28. Cui, C.; Shu, W.; Li, P., Fluorescence in situ hybridization: cell-based genetic diagnostic and research applications. *Front. Cell Dev. Biol.* **2016**, *4*, 89.
29. Nawy, T., In situ sequencing. *Nat. Methods.* **2013**, *11*, 29.
30. Vandooren, J.; Geurts, N.; Martens, E.; Van den Steen, P. E.; Opdenakker, G., Zymography methods for visualizing hydrolytic enzymes. *Nat. Methods.* **2013**, *10*, 211-220.
31. Frederiks, W. M.; Mook, O. R., Metabolic mapping of proteinase activity with emphasis on in situ zymography of gelatinases: review and protocols. *J. Histochem. Cytochem.* **2004**, *52*, 711-722.
32. Bock, C.; Farlik, M.; Sheffield, N. C., Multi-omics of single cells: strategies and applications. *Trends Biotechnol.* **2016**, *34*, 605-608.
33. Niehörster, T.; Löscherger, A.; Gregor, I.; Krämer, B.; Rahn, H.-J.; Patting, M.; Koberling, F.; Enderlein, J.; Sauer, M., Multi-target spectrally resolved fluorescence lifetime imaging microscopy. *Nat. Methods.* **2016**, *13*, 257-362.
34. Goelz, S. E.; Hamilton, S. R.; Vogelstein, B., Purification of DNA from formaldehyde fixed and paraffin embedded human tissue. *Biochem. Biophys. Res. Commun.* **1985**, *130*, 118-126.
35. Sylwestrak, E. L.; Rajasethupathy, P.; Wright, M. A.; Jaffe, A.; Deisseroth, K., Multiplexed intact-tissue transcriptional analysis at cellular resolution. *Cell* **2016**, *164*, 792-804.
36. Aichler, M.; Walch, A., MALDI Imaging mass spectrometry: current frontiers and perspectives in pathology research and practice. *Lab. Invest.* **2015**, *95*, 422-431.
37. Giesen, C.; Wang, H. A.; Schapiro, D.; Zivanovic, N.; Jacobs, A.; Hattendorf, B.; Schüffler, P. J.; Grolimund, D.; Buhmann, J. M.; Brandt, S., Highly multiplexed imaging of tumor tissues with subcellular resolution by mass cytometry. *Nat. Methods.* **2014**, *11*, 417.
38. van de Ven, S. M.; Bemis, K. D.; Lau, K.; Adusumilli, R.; Kota, U.; Stolowitz, M.; Vitek, O.; Mallick, P.; Gambhir, S. S., Protein biomarkers on tissue as imaged via MALDI mass spectrometry: A systematic approach to study the limits of detection. *Proteomics* **2016**, *16*, 1660-1669.
39. Crosetto, N.; Bienko, M.; Van Oudenaarden, A., Spatially resolved transcriptomics and beyond. *Nat. Rev. Genet.* **2015**, *16*, 57.
40. Donnarumma, F.; Camp, E. E.; Cao, F.; Murray, K. K., Infrared Laser Ablation with Vacuum Capture for Fingerprint Sampling. *J. Am. Soc. Mass Spectrom.* **2017**, *28*, 1-7.
41. Donnarumma, F.; Murray, K. K., Laser ablation sample transfer for localized LC-MS/MS proteomic analysis of tissue. *J. Mass Spectrom.* **2016**, *51*, 261-268.

42. Schey, K. L.; Anderson, D. M.; Rose, K. L., Spatially-directed protein identification from tissue sections by top-down LC-MS/MS with electron transfer dissociation. *Anal. Chem.* **2013**, *85*, 6767-6774.
43. Quanico, J.; Franck, J.; Cardon, T.; Leblanc, E.; Wisztorski, M.; Salzet, M.; Fournier, I., NanoLC-MS coupling of liquid microjunction microextraction for on-tissue proteomic analysis. *Biochim. Biophys. Acta, Proteins Proteomics* **2017**, *1865*, 891-900.
44. Laskin, J.; Lanekoff, I., Ambient Mass Spectrometry Imaging Using Direct Liquid Extraction Techniques. *Anal. Chem.* **2016**, *88*, 52-73.
45. Sarsby, J.; Martin, N. J.; Lalor, P. F.; Bunch, J.; Cooper, H. J., Top-down and bottom-up identification of proteins by liquid extraction surface analysis mass spectrometry of healthy and diseased human liver tissue. *J. Am. Soc. Mass Spectrom.* **2014**, *25*, 1953-1961.
46. Van Berkel, G. J.; Kertesz, V.; Koeplinger, K. A.; Vavrek, M.; Kong, A. N. T., Liquid microjunction surface sampling probe electrospray mass spectrometry for detection of drugs and metabolites in thin tissue sections. *J. Mass Spectrom.* **2008**, *43*, 500-508.
47. Wisztorski, M.; Desmons, A.; Quanico, J.; Fatou, B.; Gimeno, J. P.; Franck, J.; Salzet, M.; Fournier, I., Spatially-resolved protein surface microsampling from tissue sections using liquid extraction surface analysis. *Proteomics* **2016**, *16*, 1622-1632.
48. Delcourt, V.; Franck, J.; Leblanc, E.; Narducci, F.; Robin, Y.-M.; Gimeno, J.-P.; Quanico, J.; Wisztorski, M.; Kobeissy, F.; Jacques, J.-F., Combined mass spectrometry imaging and top-down microproteomics reveals evidence of a hidden proteome in ovarian cancer. *Ebiomedicine* **2017**, *21*, 55-64.
49. Le Rhun, E.; Duhamel, M.; Wisztorski, M.; Gimeno, J.-P.; Zairi, F.; Escande, F.; Reyns, N.; Kobeissy, F.; Maurage, C.-A.; Salzet, M., Evaluation of non-supervised MALDI mass spectrometry imaging combined with microproteomics for glioma grade III classification. *Biochim. Biophys. Acta, Proteins Proteomics* **2017**, *1865*, 875-890.
50. Quanico, J.; Franck, J.; Dauly, C.; Strupat, K.; Dupuy, J.; Day, R.; Salzet, M.; Fournier, I.; Wisztorski, M., Development of liquid microjunction extraction strategy for improving protein identification from tissue sections. *J. Proteomics* **2013**, *79*, 200-218.
51. Hayama, T.; Ohyama, K., Recent development and trends in sample extraction and preparation for mass spectrometric analysis of nucleotides, nucleosides, and proteins. *J. Pharm. Biomed. Anal.* **2018**, *161*, 51-60.
52. Lamont, L.; Baumert, M.; Ogrinc Potočnik, N.; Allen, M.; Vreeken, R.; Heeren, R. M.; Porta, T., Integration of ion mobility MSE after fully automated, online, high-resolution liquid extraction surface analysis micro-liquid chromatography. *Anal. Chem.* **2017**, *89*, 11143-11150.
53. Van Berkel, G. J.; Kertesz, V., Continuous-flow liquid microjunction surface sampling probe connected on-line with high-performance liquid chromatography/mass spectrometry for spatially

resolved analysis of small molecules and proteins. *Rapid Commun. Mass Spectrom.* **2013**, *27*, 1329-1334.

54. Hunt, J. L.; Finkelstein, S. D., Microdissection techniques for molecular testing in surgical pathology. *Arch. Pathol. Lab. Med.* **2004**, *128*, 1372-1378.

55. Franck, J.; Quanico, J.; Wisztorski, M.; Day, R.; Salzet, M.; Fournier, I., Quantification-based mass spectrometry imaging of proteins by parafilm assisted microdissection. *Anal. Chem.* **2013**, *85*, 8127-8134.

56. Kristiansen, G., Manual microdissection. In *Cancer Gene Profiling*, Springer: 2009; pp 31-38.

57. Adey, N.; Emery, D.; Bosh, D.; Callahan, S.; Schreiner, J.; Chen, Y.; Greig, A.; Geiersbach, K.; Parry, R., A mill based instrument and software system for dissecting slide-mounted tissue that provides digital guidance and documentation. *BMC Clin. Pathol.* **2013**, *13*, 29.

58. Geiersbach, K.; Adey, N.; Welker, N.; Elsberry, D.; Malmberg, E.; Edwards, S.; Downs-Kelly, E.; Salama, M.; Bronner, M., Digitally guided microdissection aids somatic mutation detection in difficult to dissect tumors. *Cancer Genet.* **2016**, *209*, 42-49.

59. Quanico, J.; Franck, J.; Wisztorski, M.; Salzet, M.; Fournier, I., Combined MALDI Mass Spectrometry Imaging and Parafilm-Assisted Microdissection-Based LC-MS/MS Workflows in the Study of the Brain. *Neuroproteomics: Methods and Protocols* **2017**, 269-283.

60. Quanico, J.; Franck, J.; Gimeno, J.; Sabbagh, R.; Salzet, M.; Day, R.; Fournier, I., Parafilm-assisted microdissection: a sampling method for mass spectrometry-based identification of differentially expressed prostate cancer protein biomarkers. *Chem. Commun.* **2015**, *51*, 4564-4567.

61. Quanico, J.; Franck, J.; Wisztorski, M.; Salzet, M.; Fournier, I., Integrated mass spectrometry imaging and omics workflows on the same tissue section using grid-aided, parafilm-assisted microdissection. *Biochim. Biophys. Acta, Gen. Subj.* **2017**, *1861*, 1702-1714.

62. Hoffman, D.; Chaffins, M.; Cankovic, M.; Maeda, K.; Meehan, S., Manual microdissection technique in a case of subcutaneous panniculitis-like T-cell lymphoma: a case report and review. *J. Cutan. Pathol.* **2012**, *39*, 769-772.

63. Ma, C.; Gocke, C. D.; Hruban, R. H.; Belchis, D. A., Mutational spectrum of intraepithelial neoplasia in pancreatic heterotopia. *Hum. Pathol.* **2016**, *48*, 117-121.

64. Maier, S. K.; Hahne, H.; Gholami, A. M.; Balluff, B.; Meding, S.; Schoene, C.; Walch, A. K.; Kuster, B., Comprehensive identification of proteins from MALDI imaging. *Mol. Cell. Proteomics* **2013**, *12*, 2901-2910.

65. Legres, L. G.; Janin, A.; Masselon, C.; Bertheau, P., Beyond laser microdissection technology: follow the yellow brick road for cancer research. *Am. J. Cancer Res.* **2014**, *4*, 1-28.

66. Bertos, N. R.; Park, M., Laser Capture Microdissection as a Tool to Study Tumor Stroma. *The Tumor Microenvironment: Methods and Protocols* **2016**, 13-25.
67. Datta, S.; Malhotra, L.; Dickerson, R.; Chaffee, S.; Sen, C. K.; Roy, S., Laser capture microdissection: Big data from small samples. *Histol. Histopathol.* **2015**, *30*, 1255.
68. Bidarimath, M.; Edwards, A. K.; Tayade, C., Laser capture microdissection for gene expression analysis. *Apoptosis and Cancer: Methods and Protocols* **2015**, 115-137.
69. Jensen, E., Laser-Capture Microdissection. *Anat. Rec.* **2013**, *296*, 1683-1687.
70. Tayade, C.; Edwards, A. K.; Bidarimath, M., Laser capture microdissection. In *The guide to investigation of mouse pregnancy*, Elsevier: 2014; pp 567-575.
71. Emmert-Buck, M. R.; Bonner, R. F.; Smith, P. D.; Chuaqui, R. F., Laser Capture Microdissection. *Science* **1996**, *274*, 998-1001.
72. Schütze, K.; Lahr, G., Identification of expressed genes by laser-mediated manipulation of single cells. *Nat. Biotechnol.* **1998**, *16*, 737-742.
73. AHMED, F. E., Laser microdissection: application to carcinogenesis. *Cancer Genomics-Proteomics* **2006**, *3*, 217-225.
74. Schütze, K.; Posl, H.; Lahr, G., Laser micromanipulation systems as universal tools in cellular and molecular biology and in medicine. *Cell. Mol. Biol.* **1998**, *44*, 735-746.
75. Erickson, H. S.; Albert, P. S.; Gillespie, J. W.; Rodriguez-Canales, J.; Linehan, W. M.; Pinto, P. A.; Chuaqui, R. F.; Emmert-Buck, M. R., Quantitative RT-PCR gene expression analysis of laser microdissected tissue samples. *Nat. Protoc.* **2009**, *4*, 902-922.
76. Shapiro, E.; Biezuner, T.; Linnarsson, S., Single-cell sequencing-based technologies will revolutionize whole-organism science. *Nat. Rev. Genet.* **2013**, *14*, 618-630.
77. Fend, F.; Raffeld, M., Laser capture microdissection in pathology. *J. Clin. Pathol.* **2000**, *53*, 666-672.
78. Koliijn, K.; Leenders, G. J., Comparison of RNA extraction kits and histological stains for laser capture microdissected prostate tissue. *BMC Res. Notes* **2016**, *9*, 17.
79. Lugli, G.; Kataria, Y.; Richards, Z.; Gann, P.; Zhou, X.; Nonn, L., Laser-capture microdissection of human prostatic epithelium for RNA analysis. *J. Vis. Exp.* **2015**, *105*, 53405.
80. Vandewoestyne, M.; Goossens, K.; Burvenich, C.; Van Soom, A.; Peelman, L.; Deforce, D., Laser capture microdissection: should an ultraviolet or infrared laser be used? *Anal. Biochem.* **2013**, *439*, 88-98.

81. Wang, W.-Z.; Oeschger, F. M.; Lee, S.; Molnár, Z., High quality RNA from multiple brain regions simultaneously acquired by laser capture microdissection. *BMC Mol. Biol.* **2009**, *10*, 69.
82. Chung, S. H.; Shen, W., Laser capture microdissection: from its principle to applications in research on neurodegeneration. *Neural Regen. Res.* **2015**, *10*, 897.
83. Cheng, L.; Zhang, S.; Davidson, D. D.; Kuhar, M.; Wang, M.; Williamson, S. R.; Zhang, D. Y.; MacLennan, G. T., Laser capture microdissection in molecular diagnostics. In *Molecular Genetic Pathology*, Springer: 2013; pp 465-482.
84. Braakman, R. B.; Luider, T. M.; Martens, J. W.; Foekens, J. A.; Umar, A., Laser capture microdissection applications in breast cancer proteomics. In *Laser Capture Microdissection*, Springer: 2011; pp 143-154.
85. Mukherjee, S.; Rodriguez-Canales, J.; Hanson, J.; Emmert-Buck, M. R.; Tangrea, M. A.; Prieto, D. A.; Blonder, J.; Johann, D. J., Proteomic analysis of frozen tissue samples using laser capture microdissection. In *Proteomics for Biomarker Discovery*, Springer: 2013; pp 71-83.
86. Bidarimath, M.; Edwards, A. K.; Tayade, C., Laser capture microdissection for gene expression analysis. In *Apoptosis and Cancer*, Springer: 2015; pp 115-137.
87. Kolodziejczyk, A. A.; Kim, J. K.; Svensson, V.; Marioni, J. C.; Teichmann, S. A., The technology and biology of single-cell RNA sequencing. *Mol. Cell* **2015**, *58*, 610-620.
88. Gross, A.; Schoendube, J.; Zimmermann, S.; Steeb, M.; Zengerle, R.; Koltay, P., Technologies for single-cell isolation. *Int. J. Mol. Sci.* **2015**, *16*, 16897-16919.
89. Rudloff, U.; Bhanot, U.; Gerald, W.; Klimstra, D. S.; Jarnagin, W. R.; Brennan, M. F.; Allen, P. J., Biobanking of human pancreas cancer tissue: impact of ex-vivo procurement times on RNA quality. *Ann. Surg. Oncol.* **2010**, *17*, 2229-2236.
90. Kube, D. M.; Savci-Heijink, C. D.; Lamblin, A.-F.; Kosari, F.; Vasmatzis, G.; Cheville, J. C.; Connelly, D. P.; Klee, G. G., Optimization of laser capture microdissection and RNA amplification for gene expression profiling of prostate cancer. *BMC Mol. Biol.* **2007**, *8*, 25.
91. Cheng, L.; Zhang, S.; MacLennan, G. T.; Williamson, S. R.; Davidson, D. D.; Wang, M.; Jones, T. D.; Lopez-Beltran, A.; Montironi, R., Laser-assisted microdissection in translational research: theory, technical considerations, and future applications. *Appl. Immunohistochem. Mol. Morphol.* **2013**, *21*, 31-47.
92. Lorenz, M.; Ovchinnikova, O. S.; Van Berkel, G. J., Fully automated laser ablation liquid capture surface analysis using nanoelectrospray ionization mass spectrometry. *Rapid Commun. Mass Spectrom.* **2014**, *28*, 1312-1320.
93. Cahill, J. F.; Kertesz, V.; Van Berkel, G. J., Characterization and application of a hybrid optical microscopy/laser ablation liquid vortex capture/electrospray ionization system for mass spectrometry imaging with sub-micrometer spatial resolution. *Anal. Chem.* **2015**, *87*, 11113-11121.

94. Ovchinnikova, O. S.; Kertesz, V.; Van Berkel, G. J., Combining laser ablation/liquid phase collection surface sampling and high-performance liquid chromatography– electrospray ionization-mass spectrometry. *Anal. Chem.* **2011**, *83*, 1874-1878.
95. Park, S.-G.; Murray, K. K., Infrared laser ablation sample transfer for MALDI imaging. *Anal. Chem.* **2012**, *84*, 3240-3245.
96. Donnarumma, F.; Cao, F.; Murray, K. K., Laser ablation with vacuum capture for MALDI mass spectrometry of tissue. *J. Am. Soc. Mass Spectrom.* **2016**, *27*, 108-116.
97. O'Brien, J. T.; Williams, E. R.; Holman, H.-Y. N., Ambient infrared laser ablation mass spectrometry (AIRLAB-MS) of live plant tissue with plume capture by continuous flow solvent probe. *Anal. Chem.* **2015**, *87*, 2631-2638.
98. Ren, L.; Robertson, W.; Reimer, R.; Heinze, C.; Schneider, C.; Eggert, D.; Truschow, P.; Hansen, N.-O.; Kroetz, P.; Zou, J.; Miller, R., Towards instantaneous cellular level bio diagnosis: laser extraction and imaging of biological entities with conserved integrity and activity. *Nanotechnology* **2015**, *26*, 284001.
99. Park, S.-G.; Murray, K. K., Laser ablation sample transfer for mass spectrometry imaging. In *Mass Spectrometry Imaging of Small Molecules*, Springer: 2015; pp 129-139.
100. Park, S. G.; Murray, K. K., Ambient laser ablation sampling for capillary electrophoresis mass spectrometry. *Rapid Commun. Mass Spectrom.* **2013**, *27*, 1673-1680.
101. Park, S. G.; Murray, K. K., Infrared laser ablation sample transfer for on-line liquid chromatography electrospray ionization mass spectrometry. *J. Mass Spectrom.* **2012**, *47*, 1322-1326.
102. Park, S.-G.; Murray, K. K., Infrared laser ablation sample transfer for MALDI and electrospray. *J. Am. Soc. Mass Spectrom.* **2011**, *22*, 1352-1362.
103. Ovchinnikova, O. S.; Bhandari, D.; Lorenz, M.; Van Berkel, G. J., Transmission geometry laser ablation into a non-contact liquid vortex capture probe for mass spectrometry imaging. *Rapid Commun. Mass Spectrom.* **2014**, *28*, 1665-1673.
104. Brauer, J. I.; Beech, I. B.; Sunner, J., Mass Spectrometric Imaging Using Laser Ablation and Solvent Capture by Aspiration (LASCA). *J. Am. Soc. Mass Spectrom.* **2015**, *26*, 1538-1547.
105. Brauer, J. I.; Makama, Z.; Bonifay, V.; Aydin, E.; Kaufman, E. D.; Beech, I. B.; Sunner, J., Mass spectrometric metabolomic imaging of biofilms on corroding steel surfaces using laser ablation and solvent capture by aspiration. *Biointerphases* **2015**, *10*, 019003.
106. Kaufman, E.; Smith, W.; Kowalski, M.; Beech, I.; Sunner, J., Electric-field-enhanced collection of laser-ablated materials onto a solvent bridge for electrospray ionization mass spectrometry. *Rapid Commun. Mass Spectrom.* **2013**, *27*, 1567-1572.

107. Ovchinnikova, O. S.; Kertesz, V.; Van Berkel, G. J., Combining transmission geometry laser ablation and a non-contact continuous flow surface sampling probe/electrospray emitter for mass spectrometry based chemical imaging. *Rapid Commun. Mass Spectrom.* **2011**, *25*, 3735-3740.
108. Ovchinnikova, O. S.; Lorenz, M.; Kertesz, V.; Van Berkel, G. J., Laser ablation sampling of materials directly into the formed liquid microjunction of a continuous flow surface sampling probe/electrospray ionization emitter for mass spectral analysis and imaging. *Anal. Chem.* **2013**, *85*, 10211-10217.
109. Hernández, F.; Sancho, J.; Ibáñez, M.; Abad, E.; Portolés, T.; Mattioli, L., Current use of high-resolution mass spectrometry in the environmental sciences. *Anal. Bioanal. Chem.* **2012**, *403*, 1251-1264.
110. Harrison, A. G., *Chemical Ionization Mass Spectrometry*. Routledge: 2018.
111. Thomas, R., *Practical guide to ICP-MS: a tutorial for beginners*. CRC press: 2013.
112. El-Aneed, A.; Cohen, A.; Banoub, J., Mass spectrometry, review of the basics: electrospray, MALDI, and commonly used mass analyzers. *Appl. Spectrosc. Rev.* **2009**, *44*, 210-230.
113. Banerjee, S.; Mazumdar, S., Electrospray ionization mass spectrometry: a technique to access the information beyond the molecular weight of the analyte. *Int. J. Anal. Chem.* **2012**, *2012*.
114. Meng, D.; Yongjun, C.; Wenjun, S.; Meiru, G.; Lian, C.; Huzhong, Z.; Gang, L.; Xiaoqiang, P., Newly developed compact magnetic sector mass spectrometer. *Meas. Sci. Technol.* **2017**, *28*, 125901.
115. Opota, O.; Prod'hom, G.; Greub, G., Applications of MALDI-TOF Mass Spectrometry in Clinical Diagnostic Microbiology. *MALDI-TOF and Tandem MS for Clinical Microbiology* **2017**, 55-92.
116. Nikolaev, E. N.; Kostyukevich, Y. I.; Vladimirov, G. N., Fourier transform ion cyclotron resonance (FT ICR) mass spectrometry: Theory and simulations. *Mass Spectrom. Rev.* **2016**, *35*, 219-258.
117. Zubarev, R. A.; Makarov, A., Orbitrap mass spectrometry. ACS Publications: 2013; Vol. 85.
118. Dawson, P. H., *Quadrupole mass spectrometry and its applications*. Elsevier: 2013.
119. Erickson, B. K.; Jedrychowski, M. P.; McAlister, G. C.; Everley, R. A.; Kunz, R.; Gygi, S. P., Evaluating multiplexed quantitative phosphopeptide analysis on a hybrid quadrupole mass filter/linear ion trap/orbitrap mass spectrometer. *Anal. Chem.* **2015**, *87*, 1241-1249.
120. Hillenkamp, F.; Karas, M., Matrix-assisted laser desorption/ionisation, an experience. *Int. J. Mass spectrom.* **2000**, *200*, 71-77.

121. Meetani, M. A.; Voorhees, K. J., MALDI mass spectrometry analysis of high molecular weight proteins from whole bacterial cells: pretreatment of samples with surfactants. *J. Am. Soc. Mass Spectrom.* **2005**, *16*, 1422-1426.
122. Caprioli, R. M.; Farmer, T. B.; Gile, J., Molecular Imaging of Biological Samples: Localization of Peptides and Proteins Using MALDI-TOF MS. *Anal. Chem.* **1997**, *69*, 4751-4760.
123. Bodzon - Kulakowska, A.; Suder, P., Imaging mass spectrometry: instrumentation, applications, and combination with other visualization techniques. *Mass Spectrom. Rev.* **2016**, *35*, 147-169.
124. Chang, Q.; Ornatsky, O. I.; Siddiqui, I.; Loboda, A.; Baranov, V. I.; Hedley, D. W., Imaging mass cytometry. *Cytom. A* **2017**.
125. Chatterji, B.; Pich, A., MALDI imaging mass spectrometry and analysis of endogenous peptides. *Expert Rev. Proteomics* **2013**, *10*, 381-388.
126. Thomas, A.; Chaurand, P., Advances in tissue section preparation for MALDI imaging MS. *Bioanalysis* **2014**, *6*, 967-982.
127. Caprioli, R. M., Imaging mass spectrometry: Molecular microscopy for the new age of biology and medicine. *Proteomics* **2016**, *16*, 1607-1612.
128. van de Ven, S. M. W. Y.; Bemis, K. D.; Lau, K.; Adusumilli, R.; Kota, U.; Stolowitz, M.; Vitek, O.; Mallick, P.; Gambhir, S. S., Protein biomarkers on tissue as imaged via MALDI mass spectrometry: A systematic approach to study the limits of detection. *Proteomics* **2016**, *16*, 1660-1669.
129. Dilillo, M.; Pellegrini, D.; Ait-Belkacem, R.; de Graaf, E. L.; Caleo, M.; McDonnell, L. A., Mass spectrometry imaging, laser capture microdissection, and LC-MS/MS of the same tissue section. *J. Proteome Res.* **2017**, *16*, 2993-3001.
130. Fenn, J. B.; Mann, M.; Meng, C. K.; Wong, S. F.; Whitehouse, C. M., Electrospray ionization for mass spectrometry of large biomolecules. *Science* **1989**, *246*, 64-71.
131. Gross, J. H., Tandem mass spectrometry. In *Mass Spectrometry*, Springer: 2017; pp 539-612.
132. McLafferty, F. W., Tandem mass spectrometric analysis of complex biological mixtures. *Int. J. Mass spectrom.* **2001**, *212*, 81-87.
133. Gross, J. H., Hyphenated Methods. In *Mass Spectrometry*, Springer: 2017; pp 831-887.
134. Williams, J. D.; Burinsky, D. J., Mass spectrometric analysis of complex mixtures then and now: the impact of linking liquid chromatography and mass spectrometry. *Int. J. Mass spectrom.* **2001**, *212*, 111-133.

135. Helm, D.; Vissers, J. P.; Hughes, C. J.; Hahne, H.; Ruprecht, B.; Pachi, F.; Grzyb, A.; Richardson, K.; Wildgoose, J.; Maier, S. K., Ion mobility tandem mass spectrometry enhances performance of bottom-up proteomics. *Mol. Cell. Proteomics* **2014**, *13*, 3709-3715.
136. Moradian, A.; Kalli, A.; Sweredoski, M. J.; Hess, S., The top-down, middle-down, and bottom-up mass spectrometry approaches for characterization of histone variants and their post-translational modifications. *Proteomics* **2014**, *14*, 489-497.
137. Gillet, L. C.; Leitner, A.; Aebersold, R., Mass spectrometry applied to bottom-up proteomics: entering the high-throughput era for hypothesis testing. *Annu. Rev. Anal. Chem.* **2016**, *9*, 449-472.
138. Hustoft, H. K.; Malerod, H.; Wilson, S. R.; Reubsæet, L.; Lundanes, E.; Greibrokk, T., A critical review of trypsin digestion for LC-MS based proteomics. In *Integrative Proteomics*, InTech: 2012.
139. Dunn, M. J., *Gel Electrophoresis of Proteins*. Elsevier: 2014.
140. Rabilloud, T.; Chevallet, M.; Luche, S.; Lelong, C., Two-dimensional gel electrophoresis in proteomics: past, present and future. *J. Proteomics* **2010**, *73*, 2064-2077.
141. Lee, P. Y.; Costumbrado, J.; Hsu, C.-Y.; Kim, Y. H., Agarose gel electrophoresis for the separation of DNA fragments. *J. Vis. Exp.* **2012**.
142. Westermeier, R., *Electrophoresis in Practice: A Guide to Methods and Applications of DNA and Protein Separations*. John Wiley & Sons: 2016.
143. Rio, D. C.; Ares, M.; Hannon, G. J.; Nilsen, T. W., Polyacrylamide gel electrophoresis of RNA. *Cold Spring Harb. Protoc.* **2010**, *2010*, pdb. prot5444.
144. Craven, R. A.; Totty, N.; Harnden, P.; Selby, P. J.; Banks, R. E., Laser capture microdissection and two-dimensional polyacrylamide gel electrophoresis: evaluation of tissue preparation and sample limitations. *Am. J. Pathol.* **2002**, *160*, 815-822.
145. Ornstein, D. K.; Gillespie, J. W.; Paweletz, C. P.; Duray, P. H.; Herring, J.; Vocke, C. D.; Topalian, S. L.; Bostwick, D. G.; Linehan, W. M.; Petricoin III, E. F., Proteomic analysis of laser capture microdissected human prostate cancer and in vitro prostate cell lines. *Electrophoresis* **2000**, *21*, 2235-2242.
146. Medicine, P. C. o. t. A. S. f. R., The clinical utility of sperm DNA integrity testing: a guideline. *Fertil. Steril.* **2013**, *99*, 673-677.
147. Fariello, R. M.; Pariz, J. R.; Spaine, D. M.; Cedenho, A. P.; Bertolla, R. P.; Fraietta, R., Association between obesity and alteration of sperm DNA integrity and mitochondrial activity. *BJU Int.* **2012**, *110*, 863-867.
148. Aranda, P. S.; LaJoie, D. M.; Jorcyk, C. L., Bleach gel: a simple agarose gel for analyzing RNA quality. *Electrophoresis* **2012**, *33*, 366-369.

149. Kirchner, B.; Paul, V.; Riedmaier, I.; Pfaffl, M. W., mRNA and microRNA purity and integrity: the key to success in expression profiling. In *Quantitative Real-Time PCR*, Springer: 2014; pp 43-53.
150. Copois, V.; Bibeau, F.; Bascoul-Mollevis, C.; Salvétat, N.; Chalbos, P.; Bareil, C.; Candeil, L.; Fraslon, C.; Conseiller, E.; Granci, V., Impact of RNA degradation on gene expression profiles: assessment of different methods to reliably determine RNA quality. *J. Biotechnol.* **2007**, *127*, 549-559.
151. Schroeder, A.; Mueller, O.; Stocker, S.; Salowsky, R.; Leiber, M.; Gassmann, M.; Lightfoot, S.; Menzel, W.; Granzow, M.; Ragg, T., The RIN: an RNA integrity number for assigning integrity values to RNA measurements. *BMC Mol. Biol.* **2006**, *7*, 3.
152. Legres, L. G.; Janin, A.; Masselon, C.; Bertheau, P., Beyond laser microdissection technology: follow the yellow brick road for cancer research. *Am. J. Cancer Res.* **2014**, *4*, 1.
153. Dada, R.; Mishra, S.; Mohanty, K.; Kumar, M.; Vemprala, K., Polymerase chain reaction. *Manual of Cytogenetics in Reproductive Biology* **2014**, 59.
154. Julin, D., Polymerase Chain Reaction. *Molecular Life Sciences: An Encyclopedic Reference* **2014**, 1-3.
155. Rio, D. C., Reverse transcription–polymerase chain reaction. *Cold Spring Harb. Protoc.* **2014**, *2014*, pdb. prot080887.
156. Miller, J. R.; Andre, R., Quantitative polymerase chain reaction. *Br. J. Hosp. Med.* **2014**, *75*, C188-C192.
157. Overbergh, L.; Vig, S.; Coun, F.; Mathieu, C., Quantitative Polymerase Chain Reaction. In *Molecular Diagnostics (Third Edition)*, Elsevier: 2017; pp 41-58.
158. Watson, J. D., *The polymerase chain reaction*. Springer Science & Business Media: 2012.
159. Pfaffl, M. W., Quantification strategies in real-time polymerase chain reaction. *Quantitative real-time PCR. Appl Microbiol* **2012**, 53-62.
160. Navarro, E.; Serrano-Heras, G.; Castaño, M.; Solera, J., Real-time PCR detection chemistry. *Clin. Chim. Acta* **2015**, *439*, 231-250.
161. Domazet, B.; MacLennan, G. T.; Lopez-Beltran, A.; Montironi, R.; Cheng, L., Laser capture microdissection in the genomic and proteomic era: targeting the genetic basis of cancer. *Int. J. Clin. Exp. Pathol.* **2008**, *1*, 475.
162. Singh, R. K.; Sivabalakrishnan, M., Feature selection of gene expression data for cancer classification: a review. *Procedia Comput. Sci.* **2015**, *50*, 52-57.

163. Vermeulen, J.; De Preter, K.; Lefever, S.; Nuytens, J.; De Vloed, F.; Derveaux, S.; Hellemans, J.; Speleman, F.; Vandesompele, J., Measurable impact of RNA quality on gene expression results from quantitative PCR. *Nucleic Acids Res.* **2011**, *39*, e63-e63.
164. Derveaux, S.; Vandesompele, J.; Hellemans, J., How to do successful gene expression analysis using real-time PCR. *Methods* **2010**, *50*, 227-230.
165. Opitz, L.; Salinas-Riester, G.; Grade, M.; Jung, K.; Jo, P.; Emons, G.; Ghadimi, B. M.; Beißbarth, T.; Gaedcke, J., Impact of RNA degradation on gene expression profiling. *BMC Med. Genomics* **2010**, *3*, 36.
166. Cepollaro, S.; Della Bella, E.; de Biase, D.; Visani, M.; Fini, M., Evaluation of RNA from human trabecular bone and identification of stable reference genes. *J. Cell. Physiol.* **2018**, *233*, 4401-4407.
167. Taylor, J. M., The isolation of eukaryotic messenger RNA. *Annu. Rev. Biochem* **1979**, *48*, 681-717.
168. Walker, D. G.; Whetzel, A. M.; Serrano, G.; Sue, L. I.; Lue, L.-F.; Beach, T. G., Characterization of RNA isolated from eighteen different human tissues: results from a rapid human autopsy program. *Cell Tissue Bank* **2016**, *17*, 361-375.
169. Sirakov, I. N., Nucleic Acid Isolation and Downstream Applications. In *Nucleic Acids-From Basic Aspects to Laboratory Tools*, InTech: 2016.
170. Kap, M.; Sieuwerts, A. M.; Kubista, M.; Oomen, M.; Arshad, S.; Riegman, P., The influence of tissue procurement procedures on RNA integrity, gene expression, and morphology in porcine and human liver tissue. *Biopreserv. Biobank.* **2015**, *13*, 200-206.
171. Salehi, Z.; Najafi, M., RNA Preservation and Stabilization. *Biochem Physiol* **2014**, *3*, 2-5.
172. Xu, X.; Hou, Y.; Yin, X.; Bao, L.; Tang, A.; Song, L.; Li, F.; Tsang, S.; Wu, K.; Wu, H., Single-cell exome sequencing reveals single-nucleotide mutation characteristics of a kidney tumor. *Cell* **2012**, *148*, 886-895.
173. Keays, K. M.; Owens, G. P.; Ritchie, A. M.; Gilden, D. H.; Burgoon, M. P., Laser capture microdissection and single-cell RT-PCR without RNA purification. *J. Immunol. Methods* **2005**, *302*, 90-98.
174. Green, E. D.; Rubin, E. M.; Olson, M. V., The Future of DNA Sequencing equencing. *Nature News* **2017**, *550*, 179-181.
175. Mardis, E. R., DNA sequencing technologies: 2006–2016. *Nat. Protoc.* **2017**, *12*, 213.
176. Shendure, J.; Balasubramanian, S.; Church, G. M.; Gilbert, W.; Rogers, J.; Schloss, J. A.; Waterston, R. H., DNA Sequencing at 40: Past, Present and Future. *Nature* **2017**, *550*, 345-353.

177. Moorthie, S.; Mattocks, C. J.; Wright, C. F., Review of massively parallel DNA sequencing technologies. *Hugo J.* **2011**, *5*, 1-12.
178. Chiu, C.; Miller, S., Next-generation sequencing. In *Mol. Microbiol.*, American Society of Microbiology: 2016; pp 68-79.
179. Grada, A.; Weinbrecht, K., Next-generation sequencing: methodology and application. *J. Invest. Dermatol.* **2013**, *133*, e11.
180. Green, E. D.; Rubin, E. M.; Olson, M. V., The Future of DNA Sequencing. *Nature News* **2017**, *550*, 179-181.
181. Offermann, A.; Perner, S., Next-Generation Sequencing. In *Precision Molecular Pathology of Prostate Cancer*, Springer: 2018; pp 169-192.
182. Kircher, M.; Kelso, J., High-throughput DNA sequencing—concepts and limitations. *Bioessays* **2010**, *32*, 524-536.
183. Baudhuin, L. M.; Lagerstedt, S. A.; Klee, E. W.; Fadra, N.; Oglesbee, D.; Ferber, M. J., Confirming variants in next-generation sequencing panel testing by Sanger sequencing. *J. Mol. Diagn.* **2015**, *17*, 456-461.
184. Santoro, S.; Lopez, I. D.; Lombardi, R.; Zauli, A.; Osiceanu, A. M.; Sorosina, M.; Clarelli, F.; Peroni, S.; Cazzato, D.; Marchi, M., Laser capture microdissection for transcriptomic profiles in human skin biopsies. *BMC Mol. Biol.* **2018**, *19*, 7.
185. Siniard, A. L.; Corneveaux, J. J.; De Both, M.; Chawla, M. K.; Barnes, C. A.; Huentelman, M. J., RNA sequencing from laser capture microdissected brain tissue to study normal aging and Alzheimer's disease. In *Applied Neurogenomics*, Springer: 2015; pp 111-120.
186. Rohlfing, A.; Menzel, C.; Kukreja, L. M.; Hillenkamp, F.; Dreisewerd, K., Photoacoustic analysis of matrix-assisted laser desorption/ionization processes with pulsed infrared lasers. *J. Phys. Chem. B* **2003**, *107*, 12275-12286.
187. Cao, F.; Donnarumma, F.; Murray, K. K., Particle size measurement from infrared laser ablation of tissue. *Analyst* **2016**, *141*, 183-190.
188. Musapelo, T.; Murray, K. K., Particle formation by infrared laser ablation of MALDI matrix compounds. *J. Mass Spectrom.* **2014**, *49*, 543-549.
189. Rauh, M., LC-MS/MS for protein and peptide quantification in clinical chemistry. *J. Chromatogr. B* **2012**, *883*, 59-67.
190. van den Broek, I.; van Dongen, W. D., LC-MS-based quantification of intact proteins: perspective for clinical and bioanalytical applications. *Bioanalysis* **2015**, *7*, 1943-1958.

191. Wu, Q.; Yuan, H.; Zhang, L.; Zhang, Y., Recent advances on multidimensional liquid chromatography–mass spectrometry for proteomics: From qualitative to quantitative analysis—A review. *Anal. Chim. Acta* **2012**, *731*, 1-10.
192. Nelson, R. W.; Rainbow, M. J.; Lohr, D. E.; Williams, P., Volatilization of high molecular weight DNA by pulsed laser ablation of frozen aqueous solutions. *Science* **1989**, *246*, 1585-1587.
193. Romano, L. J.; Levis, R. J., Nondestructive laser vaporization of high molecular weight, single-stranded DNA. *J. Am. Chem. Soc.* **1991**, *113*, 9665-9667.
194. Fleige, S.; Pfaffl, M. W., RNA integrity and the effect on the real-time qRT-PCR performance. *Mol. Aspects Med.* **2006**, *27*, 126-139.
195. Strand, C.; Enell, J.; Hedenfalk, I.; Fernö, M., RNA quality in frozen breast cancer samples and the influence on gene expression analysis—a comparison of three evaluation methods using microcapillary electrophoresis traces. *BMC Mol. Biol.* **2007**, *8*, 38.
196. Bustin, S. A.; Vandesomepele, J.; Pfaffl, M., Standardization of qPCR and RT-qPCR. *Gen Eng Biotechnol News 2009b* **2009**, *29*.
197. Kukurba, K. R.; Montgomery, S. B., RNA Sequencing and Analysis. *Cold Spring Harb. Protoc.* **2015**, *11*, 951-969.
198. Weis, S.; Llenos, I.; Dulay, J.; Elashoff, M.; Martinez-Murillo, F.; Miller, C., Quality control for microarray analysis of human brain samples: the impact of postmortem factors, RNA characteristics, and histopathology. *J. Neurosci. Methods* **2007**, *165*, 198-209.
199. Romero, I. G.; Pai, A. A.; Tung, J.; Gilad, Y., RNA-seq: impact of RNA degradation on transcript quantification. *BMC Biol.* **2014**, *12*, 42.
200. Kuang, J.; Yan, X.; Genders, A. J.; Granata, C.; Bishop, D. J., An overview of technical considerations when using quantitative real-time PCR analysis of gene expression in human exercise research. *PLoS One* **2018**, *13*, e0196438.
201. Harris, S. E., Tunable optical parametric oscillators. *Proc. IEEE* **1969**, *57*, 2096-2113.
202. Vogel, A.; Venugopalan, V., Mechanisms of pulsed laser ablation of biological tissues. *Chem. Rev.* **2003**, *103*, 577-644.
203. Little, M. W.; Laboy, J.; Murray, K. K., Wavelength dependence of soft infrared laser desorption and ionization. *J. Phys. Chem. C* **2007**, *111*, 1412-1416.
204. Paglia, G.; Kliman, M.; Claude, E.; Geromanos, S.; Astarita, G., Applications of ion-mobility mass spectrometry for lipid analysis. *Anal. Bioanal. Chem.* **2015**, *407*, 4995-5007.

205. Vaysse, P.-M.; Heeren, R.; Porta, T.; Balluff, B., Mass Spectrometry Imaging for Clinical Research—Latest Developments, Applications, and Current Limitations. *Analyst* **2017**, *15*, 2690-2712.
206. Domon, B.; Aebersold, R., Mass spectrometry and protein analysis. *Science* **2006**, *312*, 212-217.
207. Gillet, L. C.; Navarro, P.; Tate, S.; Röst, H.; Selevsek, N.; Reiter, L.; Bonner, R.; Aebersold, R., Targeted data extraction of the MS/MS spectra generated by data-independent acquisition: a new concept for consistent and accurate proteome analysis. *Mol. Cell. Proteomics* **2012**, *11*, O111. 016717.
208. Kearse, M.; Moir, R.; Wilson, A.; Stones-Havas, S.; Cheung, M.; Sturrock, S.; Buxton, S.; Cooper, A.; Markowitz, S.; Duran, C., Geneious Basic: an integrated and extendable desktop software platform for the organization and analysis of sequence data. *Bioinformatics* **2012**, *28*, 1647-1649.
209. Blazej, R. G.; Kumaresan, P.; Mathies, R. A., Microfabricated bioprocessor for integrated nanoliter-scale Sanger DNA sequencing. *Proc. Natl. Acad. Sci. U.S.A.* **2006**, *103*, 7240-7245.
210. Ewing, B.; Hillier, L.; Wendl, M. C.; Green, P., Base-calling of automated sequencer traces using Phred. I. Accuracy assessment. *Genome Res.* **1998**, *8*, 175-185.
211. Ewing, B.; Green, P., Base-calling of automated sequencer traces using phred. II. Error probabilities. *Genome Res.* **1998**, *8*, 186-194.
212. Gessel, M. M.; Norris, J. L.; Caprioli, R. M., MALDI imaging mass spectrometry: spatial molecular analysis to enable a new age of discovery. *J. Proteomics* **2014**, *107*, 71-82.
213. Schwamborn, K.; Kriegsmann, M.; Weichert, W., MALDI imaging mass spectrometry—From bench to bedside. *Biochim. Biophys. Acta, Proteins Proteomics* **2017**, *1865*, 776-783.
214. Baker, T. C.; Han, J.; Borchers, C. H., Recent advancements in matrix-assisted laser desorption/ionization mass spectrometry imaging. *Curr. Opin. Biotechnol.* **2017**, *43*, 62-69.
215. Kriegsmann, J.; Kriegsmann, M.; Casadonte, R., MALDI TOF imaging mass spectrometry in clinical pathology: a valuable tool for cancer diagnostics. *Int. J. Oncol.* **2015**, *46*, 893-906.
216. Sparvero, L. J.; Amoscato, A. A.; Dixon, C. E.; Long, J. B.; Kochanek, P. M.; Pitt, B. R.; Bayır, H.; Kagan, V. E., Mapping of phospholipids by MALDI imaging (MALDI-MSI): realities and expectations. *Chem. Phys. Lipids* **2012**, *165*, 545-562.
217. Quanico, J.; Franck, J.; Wisztorski, M.; Salzet, M.; Fournier, I., Progress and Potential of Imaging Mass Spectrometry Applied to Biomarker Discovery. *Neuroproteomics: Methods and Protocols* **2017**, 21-43.

218. Ucal, Y.; Durer, Z. A.; Atak, H.; Kadioglu, E.; Sahin, B.; Coskun, A.; Baykal, A. T.; Ozpinar, A., Clinical applications of MALDI imaging technologies in cancer and neurodegenerative diseases. *Biochim. Biophys. Acta, Proteins Proteomics* **2017**, *1865*, 795-816.
219. Lodén, H.; Shariatgorji, M.; Nilsson, A.; Andrén, P. E., An introduction to MS imaging in drug discovery and development. *Bioanalysis* **2015**, *7*, 2621-2627.
220. Vaysse, P.-M.; Heeren, R. M.; Porta, T.; Balluff, B., Mass spectrometry imaging for clinical research—latest developments, applications, and current limitations. *Analyst* **2017**, *142*, 2690-2712.
221. McDonnell, L.; Angel, P.; Lou, S.; Drake, R., Mass Spectrometry Imaging in Cancer Research: Future Perspectives. In *Adv. Cancer Res.*, Elsevier: 2017; Vol. 134, pp 283-290.
222. Laskin, J.; Lanekoff, I., Ambient mass spectrometry imaging using direct liquid extraction techniques. *Anal. Chem.* **2015**, *88*, 52-73.
223. Emmert-Buck, M. R.; Bonner, R. F.; Smith, P. D.; Chuaqui, R. F.; Zhuang, Z.; Goldstein, S. R.; Weiss, R. A.; Liotta, L. A., Laser Capture Microdissection. *Science* **1996**, *274*, 998-1001.
224. Murray, G. I.; MARTON., *Laser capture microdissection*. Springer: 2010.
225. Ren, L.; Robertson, W.; Reimer, R.; Heinze, C.; Schneider, C.; Eggert, D.; Truschow, P.; Hansen, N.-O.; Kroetz, P.; Zou, J., Towards instantaneous cellular level bio diagnosis: laser extraction and imaging of biological entities with conserved integrity and activity. *Nanotechnology* **2015**, *26*, 284001.
226. Banstola, B.; Grodner, E. T.; Cao, F.; Donnarumma, F.; Murray, K. K., Systematic assessment of surfactants for matrix-assisted laser desorption/ionization mass spectrometry imaging. *Anal. Chim. Acta* **2017**, *963*, 76-82.
227. Hughes, C. S.; Foehr, S.; Garfield, D. A.; Furlong, E. E.; Steinmetz, L. M.; Krijgsveld, J., Ultrasensitive proteome analysis using paramagnetic bead technology. *Mol. Syst. Biol.* **2014**, *10*, 757.
228. Pettit, M. E.; Donnarumma, F.; Murray, K. K.; Solouki, T., Infrared laser ablation sampling coupled with data independent high resolution UPLC-IM-MS/MS for tissue analysis. *Anal. Chim. Acta* **2018**, *1034*, 102-109.
229. Huang, D. W.; Sherman, B. T.; Lempicki, R. A., Systematic and integrative analysis of large gene lists using DAVID bioinformatics resources. *Nat. Protoc.* **2008**, *4*, 44-57.
230. Huang, D. W.; Sherman, B. T.; Lempicki, R. A., Bioinformatics enrichment tools: paths toward the comprehensive functional analysis of large gene lists. *Nucleic Acids Res.* **2008**, *37*, 1-13.

231. Szklarczyk, D.; Franceschini, A.; Wyder, S.; Forslund, K.; Heller, D.; Huerta-Cepas, J.; Simonovic, M.; Roth, A.; Santos, A.; Tsafou, K. P., STRING v10: protein–protein interaction networks, integrated over the tree of life. *Nucleic Acids Res.* **2014**, *43*, D447-D452.
232. Zavalin, A.; Yang, J.; Hayden, K.; Vestal, M.; Caprioli, R. M., Tissue protein imaging at 1  $\mu\text{m}$  laser spot diameter for high spatial resolution and high imaging speed using transmission geometry MALDI TOF MS. *Anal. Bioanal. Chem.* **2015**, *407*, 2337-2342.
233. Lin, L.-E.; Su, P.-R.; Wu, H.-Y.; Hsu, C.-C., A Simple Sonication Improves Protein Signal in Matrix-Assisted Laser Desorption Ionization Imaging. *J. Am. Soc. Mass Spectrom.* **2018**, *29*, 796-799.
234. Distler, U.; Kuharev, J.; Navarro, P.; Tenzer, S., Label-free quantification in ion mobility–enhanced data-independent acquisition proteomics. *Nat. Protoc.* **2016**, *11*, 795-812.
235. Dilillo, M.; Ait-Belkacem, R.; Esteve, C.; Pellegrini, D.; Nicolardi, S.; Costa, M.; Vannini, E.; de Graaf, E.; Caleo, M.; McDonnell, L., Ultra-high mass resolution MALDI imaging mass spectrometry of proteins and metabolites in a mouse model of glioblastoma. *Sci. Rep.* **2017**, *7*, 603-613.
236. Zhan, X.; Jickling, G. C.; Ander, B. P.; Stamova, B.; Liu, D.; Kao, P. F.; Zelin, M. A.; Jin, L.-W.; DeCarli, C.; Sharp, F. R., Myelin Basic Protein Associates with A $\beta$ PP, A $\beta$  1-42, and Amyloid Plaques in Cortex of Alzheimer's Disease Brain. *J. Alzheimers Dis.* **2015**, *44*, 1213-1229.
237. Liao, M.-C.; Ahmed, M.; Smith, S. O.; Van Nostrand, W. E., Degradation of amyloid  $\beta$  protein by purified myelin basic protein. *J. Biol. Chem.* **2009**, *284*, 28917-28925.
238. Ou-Yang, M.-H.; Van Nostrand, W. E., The absence of myelin basic protein promotes neuroinflammation and reduces amyloid  $\beta$ -protein accumulation in Tg-5xFAD mice. *J. Neuroinflammation* **2013**, *10*, 901-912.
239. Kim, S. H.; Vlkolinsky, R.; Cairns, N.; Fountoulakis, M.; Lubec, G., The reduction of NADH: Ubiquinone oxidoreductase 24-and 75-kDa subunits in brains of patients with Down syndrome and Alzheimer's disease. *Life Sci.* **2001**, *68*, 2741-2750.
240. Munoz, L.; Ammit, A. J., Targeting p38 MAPK pathway for the treatment of Alzheimer's disease. *Neuropharmacology* **2010**, *58*, 561-568.
241. Estabel, J., 3 Enzyme Histochemistry Methods. *Histochemical and Cytochemical Methods of Visualization* **2013**, 139.
242. Meier-Ruge, W. A.; Bruder, E., Current concepts of enzyme histochemistry in modern pathology. *Pathobiology* **2008**, *75*, 233-243.
243. Bogoy, M.; Cravatt, B. F., Genomics and proteomics: from genes to function: advances in applications of chemical and systems biology. *Curr. Opin. Chem. Biol.* **2007**, *11*, 1-3.

244. Van Noorden, C. J., Metabolic mapping by enzyme histochemistry in living animals, tissues and cells. *J. Physiol. Pharmacol.* **2009**, *60*, 125-129.
245. Van Noorden, C. J., Imaging enzymes at work: metabolic mapping by enzyme histochemistry. *J. Histochem. Cytochem.* **2010**, *58*, 481-497.
246. Withana, N. P.; Garland, M.; Verdoes, M.; Ofori, L. O.; Segal, E.; Bogoyo, M., Labeling of active proteases in fresh-frozen tissues by topical application of quenched activity-based probes. *Nat. Protoc.* **2016**, *11*, 184-191.
247. Pampalakis, G.; Zingkou, E.; Vekrellis, K.; Sotiropoulou, G., "Activography": a novel, versatile and easily adaptable method for monitoring enzymatic activities in situ. *Chem. Commun. (Camb.)* **2017**, *53*, 3246-3248.
248. Langton, A. K.; Griffiths, C. E.; Sherratt, M. J.; Watson, R. E., Cross-linking of structural proteins in ageing skin: an in situ assay for the detection of amine oxidase activity. *Biogerontology* **2013**, *14*, 89-97.
249. van Smeden, J.; Dijkhoff, I. M.; Helder, R. W.; Al-Khakany, H.; Boer, D. E.; Schreuder, A.; Kallemeijn, W. W.; Absalah, S.; Overkleeft, H. S.; Aerts, J. M., In-situ visualization of glucocerebrosidase in human skin tissue: Zymography vs activity-based probe labeling. *J. Lipid Res.* **2017**, jlr. M079376.
250. Wilkesman, J.; Kurz, L., Zymography Principles. *Methods Mol. Biol.* **2017**, *1626*, 3-10.
251. Yang, P.; Liu, K., Activity-Based Protein Profiling: Recent Advances in Probe Development and Applications. *ChemBiochem* **2015**, *16*, 712-724.
252. Krysiak, J. M.; Kreuzer, J.; Macheroux, P.; Hermetter, A.; Sieber, S. A.; Breinbauer, R., Activity-Based Probes for Studying the Activity of Flavin-Dependent Oxidases and for the Protein Target Profiling of Monoamine Oxidase Inhibitors. *Angew. Chem. Int. Ed. Engl.* **2012**, *51*, 7035-7040.
253. Yan, S.; Blomme, E., In situ zymography: a molecular pathology technique to localize endogenous protease activity in tissue sections. *Vet. Pathol.* **2003**, *40*, 227-236.
254. Wilkesman, J.; Kurz, L., Protease analysis by zymography: a review on techniques and patents. *Recent Pat. Biotechnol.* **2009**, *3*, 175-184.
255. Scaffa, P. M. C.; Breschi, L.; Mazzoni, A.; Vidal, C. d. M. P.; Curci, R.; Apolonio, F.; Gobbi, P.; Pashley, D.; Tjäderhane, L.; dos Santos Tersariol, I. L., Co-distribution of cysteine cathepsins and matrix metalloproteases in human dentin. *Arch. Oral Biol.* **2017**, *74*, 101-107.
256. Ispas, C. R.; Crivat, G.; Andreescu, S., recent developments in enzyme-based biosensors for biomedical analysis. *Anal. Lett.* **2012**, *45*, 168-186.

257. Sanman, L. E.; Bogyo, M., Activity-based profiling of proteases. *Annu. Rev. Biochem.* **2014**, *83*, 249-273.
258. Abbott, E.; Hall, D.; Hamberger, B.; Bohlmann, J., Laser microdissection of conifer stem tissues: isolation and analysis of high quality RNA, terpene synthase enzyme activity and terpenoid metabolites from resin ducts and cambial zone tissue of white spruce (*Picea glauca*). *BMC Plant Biol.* **2010**, *10*, 106.
259. Lee, J. W.; Chou, C.-L.; Knepper, M. A., Deep sequencing in microdissected renal tubules identifies nephron segment-specific transcriptomes. *J. Am. Soc. Nephrol.* **2015**, ASN. 2014111067.
260. Bisswanger, H., Enzyme assays. *Perspectives in Science* **2014**, *1*, 41-55.
261. Weissleder, R.; Pittet, M. J., Imaging in the era of molecular oncology. *Nature* **2008**, *452*, 580-589.
262. Luker, G. D.; Luker, K. E., Optical imaging: current applications and future directions. *J. Nucl. Med.* **2008**, *49*, 1-4.
263. Bishop, D. P.; Cole, N.; Zhang, T.; Doble, P. A.; Hare, D. J., A guide to integrating immunohistochemistry and chemical imaging. *ChSRv* **2018**.
264. Scherzer, P.; Gal-Moscovici, A.; Sheikh-Hamad, D.; Popovtzer, M. M., Sodium-pump gene-expression, protein abundance and enzyme activity in isolated nephron segments of the aging rat kidney. *Physiol. Rep.* **2015**, *3*, e12369.
265. Eltoum, I. A.; Siegal, G. P.; Frost, A. R., Microdissection of histologic sections: past, present, and future. *Adv. Anat. Pathol.* **2002**, *9*, 316-322.
266. Donnarumma, F.; Cao, F.; Murray, K. K., Laser Ablation with Vacuum Capture for MALDI Mass Spectrometry of Tissue. *J. Am. Soc. Mass Spectrom.* **2016**, *27*, 108-116.
267. Wang, K.; Donnarumma, F.; Herke, S. W.; Herke, P. F.; Murray, K. K., Infrared laser ablation sample transfer of tissue DNA for genomic analysis. *Anal. Bioanal. Chem.* **2017**, 1-8.
268. Cummings, J. P.; Walsh Jr, J. T., Erbium laser ablation: the effect of dynamic optical properties. *Appl. Phys. Lett.* **1993**, *62*, 1988-1990.
269. Apitz, I.; Vogel, A., Material ejection in nanosecond Er: YAG laser ablation of water, liver, and skin. *Appl. Phys. A* **2005**, *81*, 329-338.
270. Fan, X.; Little, M. W.; Murray, K. K., Infrared laser wavelength dependence of particles ablated from glycerol. *Appl. Surf. Sci.* **2008**, *255*, 1699-1704.
271. Cao, F.; Donnarumma, F.; Murray, K. K., Particle size measurement from infrared laser ablation of tissue. *Analyst* **2016**, *141*, 183-190.

272. Murakami, S.; Kashii, M.; Kitano, H.; Adachi, H.; Takano, K.; Matsumura, H.; Inoue, T.; Mori, Y.; Doi, M.; Sugamoto, K., Effect of laser irradiation on enzyme activity. *Jpn. J. Appl. Phys.* **2005**, *44*, 8216.
273. Ren, L.; Robertson, W.; Reimer, R.; Heinze, C.; Schneider, C.; Eggert, D.; Truschow, P.; Hansen, N.-O.; Kroetz, P.; Zou, J.; Miller, R. D., Towards instantaneous cellular level bio diagnosis: laser extraction and imaging of biological entities with conserved integrity and activity. *Nanotechnology* **2015**, *26*, 284001.
274. Franjic, K.; Miller, R. J. D., Vibrationally Excited Ultrafast Thermodynamic Phase Transitions at the Water/Air Interface. *Phys. Chem. Chem. Phys.* **2010**, *12*, 5225-5239.
275. Bradford, M. M., A rapid and sensitive method for the quantitation of microgram quantities of protein utilizing the principle of protein-dye binding. *Anal. Biochem.* **1976**, *72*, 248-254.
276. Kwiatkowski, M.; Wurlitzer, M.; Omid, M.; Ren, L.; Kruber, S.; Nimer, R.; Robertson, W. D.; Horst, A.; Miller, R.; Schlüter, H., Ultrafast extraction of proteins from tissues using desorption by impulsive vibrational excitation. *Angew. Chem. Int. Ed.* **2015**, *54*, 285-288.
277. Zou, J.; Wu, C.; Robertson, W.; Zhigilei, L.; Miller, R., Molecular dynamics investigation of desorption and ion separation following picosecond infrared laser (PIRL) ablation of an ionic aqueous protein solution. *J. Chem. Phys.* **2016**, *145*, 204202.
278. Franjic, K.; Cowan, M. L.; Kraemer, D.; Miller, R. D., Laser selective cutting of biological tissues by impulsive heat deposition through ultrafast vibrational excitations. *Opt. Express* **2009**, *17*, 22937-22959.
279. Siqueira, I. R.; Fochesatto, C.; de Andrade, A.; Santos, M.; Hagen, M.; Bello-Klein, A.; Netto, C. A., Total antioxidant capacity is impaired in different structures from aged rat brain. *Int. J. Dev. Neurosci.* **2005**, *23*, 663-671.
280. Homi, H. I. M.; Freitas, J. J.; Curi, R.; Velasco, I. T.; Junior, B. A., Changes in superoxide dismutase and catalase activities of rat brain regions during early global transient ischemia/reperfusion. *Neurosci. Lett.* **2002**, *333*, 37-40.
281. Jayaraman, T.; Kannappan, S.; Ravichandran, M.; Anuradha, C., Impact of Essentiale L on ethanol-induced changes in rat brain and erythrocytes. *Singapore Med. J.* **2008**, *49*, 320-327.
282. Kazi, A. I.; Oommen, A., Monocrotophos induced oxidative damage associates with severe acetylcholinesterase inhibition in rat brain. *Neurotoxicology* **2012**, *33*, 156-161.
283. Fortunato, J. J.; Feier, G.; Vitali, A. M.; Petronilho, F. C.; Dal-Pizzol, F.; Quevedo, J., Malathion-induced oxidative stress in rat brain regions. *Neurochem. Res.* **2006**, *31*, 671-678.
284. Harrell, J. C.; Dye, W. W.; Harvell, D. M.; Sartorius, C. A.; Horwitz, K. B., Contaminating cells alter gene signatures in whole organ versus laser capture microdissected tumors: a

comparison of experimental breast cancers and their lymph node metastases. *Clin. Exp. Metastasis* **2008**, *25*, 81-88.

285. Klee, E. W.; Erdogan, S.; Tillmans, L.; Kosari, F.; Sun, Z.; Wigle, D. A.; Yang, P.; Aubry, M. C.; Vasmatazis, G., Impact of sample acquisition and linear amplification on gene expression profiling of lung adenocarcinoma: laser capture micro-dissection cell-sampling versus bulk tissue-sampling. *BMC Med. Genomics* **2009**, *2*, 13.

286. Rabien, A.; Kristiansen, G., Tissue Microdissection. *Cancer Gene Profiling: Methods and Protocols* **2016**, 39-52.

287. Moelans, C. B.; de Weger, R. A.; Ezendam, C.; van Diest, P. J., HER-2/neu amplification testing in breast cancer by Multiplex Ligation-dependent Probe Amplification: influence of manual-and laser microdissection. *BMC Cancer* **2009**, *9*, 1.

288. Hoefig, K. P.; Heissmeyer, V., Measuring microRNA expression in size-limited FACS-sorted and microdissected samples. *MicroRNAs and the immune system: methods and protocols* **2010**, 47-63.

289. Kristiansen, G., Manual microdissection. *Cancer Gene Profiling: Methods and Protocols* **2010**, 31-38.

290. Espina, V.; Wulfkuhle, J. D.; Calvert, V. S.; VanMeter, A.; Zhou, W.; Coukos, G.; Geho, D. H.; Petricoin, E. F.; Liotta, L. A., Laser-capture microdissection. *Nat. Protoc.* **2006**, *1*, 586-603.

291. Park, S. G.; Murray, K. K., Infrared laser ablation sample transfer for MALDI and electrospray. *J. Am. Soc. Mass Spectrom.* **2011**, *22*, 1352-1362.

292. Park, S. G.; Murray, K. K., Infrared laser ablation sample transfer for on-line liquid chromatography electrospray ionization mass spectrometry. *J. Mass Spectrom.* **2012**, *47*, 1322-1326.

293. Park, S. G.; Murray, K. K., Infrared Laser Ablation Sample Transfer for MALDI Imaging. *Anal. Chem.* **2012**, *84*, 3240-3245.

294. Brody, J. R.; Kern, S. E., Sodium boric acid: a Tris-free, cooler conductive medium for DNA electrophoresis. *Biotechniques* **2004**, *36*, 214-217.

295. Brody, J. R.; Kern, S. E., History and principles of conductive media for standard DNA electrophoresis. *Anal. Biochem.* **2004**, *333*, 1-13.

296. Quail, M. A., DNA: Mechanical breakage. *eLS* **2010**.

297. Blanksby, S. J.; Ellison, G. B., Bond dissociation energies of organic molecules. *Acc. Chem. Res.* **2003**, *36*, 255-263.

298. Lin, C.-H.; Chen, Y.-C.; Pan, T.-M., Quantification bias caused by plasmid DNA conformation in quantitative real-time PCR assay. *PLoS One* **2011**, *6*, e29101.
299. Demeke, T.; Jenkins, G. R., Influence of DNA extraction methods, PCR inhibitors and quantification methods on real-time PCR assay of biotechnology-derived traits. *Anal. Bioanal. Chem.* **2010**, *396*, 1977-1990.
300. Braakman, R. B.; Bezstarosti, K.; Siewerts, A. M.; de Weerd, V.; van Galen, A. M.; Stingl, C.; Luider, T. M.; Timmermans, M. A.; Smid, M.; Martens, J. W., Integrative analysis of genomics and proteomics data on clinical breast cancer tissue specimens extracted with acid guanidinium thiocyanate–phenol–chloroform. *J. Proteome Res.* **2015**, *14*, 1627-1636.
301. Zmetakova, I.; Danihel, L.; Smolkova, B.; Mego, M.; Kajabova, V.; Krivulcik, T.; Rusnak, I.; Rychly, B.; Danis, D.; Repiska, V., Evaluation of protein expression and DNA methylation profiles detected by pyrosequencing in invasive breast cancer. *Neoplasma* **2013**, *60*, 635-646.
302. Vaitkienė, P.; Skiriutė, D.; Skauminas, K.; Tamašauskas, A., Associations between TFPI-2 methylation and poor prognosis in glioblastomas. *Medicina (Kaunas)* **2012**, *48*, 345-349.
303. Sokolova, Y. Y.; Sakaguchi, K.; Paulsen, D. B., Establishing a New Species *Encephalitozoon pogonae* for the Microsporidian Parasite of Inland Bearded Dragon *Pogona vitticeps* Ahl 1927 (Reptilia, Squamata, Agamidae). *J. Eukaryot. Microbiol.* **2016**, 524-535.
304. Dunham, J. P.; Friesen, M. L., A cost-effective method for high-throughput construction of illumina sequencing libraries. *Cold Spring Harb. Protoc.* **2013**, *2013*, 820-834.
305. Serganov, A.; Nudler, E., A decade of riboswitches. *Cell* **2013**, *152*, 17-24.
306. Breaker, R. R.; Joyce, G. F., The expanding view of RNA and DNA function. *Chem. Biol.* **2014**, *21*, 1059-1065.
307. Connelly, C. M.; Moon, M. H.; Schneekloth Jr, J. S., The emerging role of RNA as a therapeutic target for small molecules. *Cell Chem. Biol.* **2016**, *23*, 1077-1090.
308. Kim, D. H.; Rossi, J. J., Strategies for silencing human disease using RNA interference. *Nat. Rev. Genet.* **2007**, *8*, 173-184.
309. Sanders, R.; Mason, D. J.; Foy, C. A.; Huggett, J. F., Evaluation of digital PCR for absolute RNA quantification. *PLoS One* **2013**, *8*, e75296.
310. Maslove, D. M.; Wong, H. R., Gene expression profiling in sepsis: timing, tissue, and translational considerations. *Trends Mol. Med.* **2014**, *20*, 204-213.
311. Chiskooree, D.; Zhu, K.; Ram, V.; Wu, H. J.; He, Z. J.; Zhang, S., A preliminary microarray assay of the mi RNA expression signatures in buccal mucosa of oral submucous fibrosis patients. *J. Oral Pathol. Med.* **2016**, *45*, 691-697.

312. Chu, Y.; Corey, D. R., RNA sequencing: platform selection, experimental design, and data interpretation. *Nucleic Acid Ther.* **2012**, *22*, 271-274.
313. Liu, L.; Li, Y.; Li, S.; Hu, N.; He, Y.; Pong, R.; Lin, D.; Lu, L.; Law, M., Comparison of next-generation sequencing systems. *Biomed Res. Int.* **2012**, *2012*.
314. Ozsolak, F.; Milos, P. M., RNA sequencing: advances, challenges and opportunities. *Nat. Rev. Genet.* **2011**, *12*, 87-98.
315. Idda, M. L.; Munk, R.; Abdelmohsen, K.; Gorospe, M., Noncoding RNAs in Alzheimer's disease. *Wiley Interdiscip. Rev. RNA* **2018**, *9*, e1463.
316. Teixidó, C.; Giménez-Capitán, A.; Molina-Vila, M. Á.; Peg, V.; Karachaliou, N.; Rodríguez-Capote, A.; Castellví, J.; Rosell, R., RNA Analysis as a Tool to Determine Clinically Relevant Gene Fusions and Splice Variants. *Arch. Pathol. Lab. Med.* **2018**, *142*, 474-479.
317. Quarello, P.; Garelli, E.; Carando, A.; Mancini, C.; Foglia, L.; Botto, C.; Farruggia, P.; De Keersmaecker, K.; Aspesi, A.; Ellis, S. R., Ribosomal RNA analysis in the diagnosis of Diamond-Blackfan Anaemia. *Br. J. Haematol.* **2016**, *172*, 782-785.
318. Serratì, S.; De Summa, S.; Pilato, B.; Petriella, D.; Lacalamita, R.; Tommasi, S.; Pinto, R., Next-generation sequencing: advances and applications in cancer diagnosis. *Onco Targets Ther.* **2016**, *9*, 7355-7365.
319. Cirera, S., Highly efficient method for isolation of total RNA from adipose tissue. *BMC Res. Notes* **2013**, *6*, 472.
320. Caprez, S.; Menzel, U.; Li, Z.; Grad, S.; Alini, M.; Peroglio, M., Isolation of high-quality RNA from intervertebral disc tissue via pronase predigestion and tissue pulverization. *JOR Spine* **2018**, *1*, e1017.
321. Verollet, R., A major step towards efficient sample preparation with bead-beating. *Biotechniques* **2008**, *44*, 832-833.
322. Banneau, G.; Ayadi, M.; Armenoult, L.; Carvalho, E., Homogenization of cartilage tumors to extract total RNA to microarray and sequencing analysis using Precellys bead-beating technology. *Biotechniques* **2012**, *52*, 196-197.
323. Ali, N.; Rampazzo, R. d. C. P.; Costa, A. D. T.; Krieger, M. A., Current nucleic acid extraction methods and their implications to point-of-care diagnostics. *Biomed Res. Int.* **2017**, *2017*.
324. Chirgwin, J. M.; Przybyla, A. E.; MacDonald, R. J.; Rutter, W. J., Isolation of biologically active ribonucleic acid from sources enriched in ribonuclease. *Biochemistry* **1979**, *18*, 5294-5299.
325. Chomczynski, P.; Sacchi, N., The single-step method of RNA isolation by acid guanidinium thiocyanate–phenol–chloroform extraction: twenty-something years on. *Nat. Protoc.* **2006**, *1*, 581-586.

326. Chomczynski, P.; Sacchi, N., Single-step method of RNA isolation by acid guanidinium thiocyanate-phenol-chloroform extraction. *Anal. Biochem.* **1987**, *162*, 156-159.
327. Watermann, C.; Peter Valerius, K.; Wagner, S.; Wittekindt, C.; Peter Klussmann, J.; Baumgart-Vogt, E.; Karnati, S., Step-by-step protocol to perfuse and dissect the mouse parotid gland and isolation of high-quality RNA from murine and human parotid tissue. *Biotechniques* **2016**, *60*, 200-203.
328. Griffin, M.; Abu-El-Haija, M.; Abu-El-Haija, M.; Rokhlina, T.; Uc, A., Simplified and versatile method for isolation of high-quality RNA from pancreas. *Biotechniques* **2012**, *52*, 332-334.
329. Tesena, P.; Korchunjit, W.; Taylor, J.; Wongtawan, T., Comparison of commercial RNA extraction kits and qPCR master mixes for studying gene expression in small biopsy tissue samples from the equine gastric epithelium. *J Equine Sci.* **2017**, *28*, 135-141.
330. Azevedo-Pouly, A. C. P.; Elgamal, O. A.; Schmittgen, T. D., RNA isolation from mouse pancreas: a ribonuclease-rich tissue. *J. Vis. Exp.* **2014**, *90*, e51779.
331. Krieg, P. A., *A laboratory guide to RNA: isolation, analysis, and synthesis*. John Wiley & Sons: 1996.
332. Farrell Jr, R. E., *RNA Methodologies: laboratory guide for isolation and characterization*. Academic Press: 2009.
333. Hou, Y.; Guo, H.; Cao, C.; Li, X.; Hu, B.; Zhu, P.; Wu, X.; Wen, L.; Tang, F.; Huang, Y., Single-cell triple omics sequencing reveals genetic, epigenetic, and transcriptomic heterogeneity in hepatocellular carcinomas. *Cell Res.* **2016**, *26*, 304-319.
334. Moor, A. E.; Itzkovitz, S., Spatial transcriptomics: paving the way for tissue-level systems biology. *Curr. Opin. Biotechnol.* **2017**, *46*, 126-133.
335. Farris, S.; Wang, Y.; Ward, J. M.; Dudek, S. M., Optimized method for robust transcriptome profiling of minute tissues using laser capture microdissection and low-input RNA-Seq. *Front. Mol. Neurosci.* **2017**, *10*, 185.
336. Kwiatkowski, M.; Wurlitzer, M.; Omid, M.; Ren, L.; Kruber, S.; Nimer, R.; Robertson, W. D.; Horst, A.; Miller, R. D.; Schlüter, H., Ultrafast extraction of proteins from tissues using desorption by impulsive vibrational excitation. *Angew. Chem. Int. Ed.* **2015**, *54*, 285-288.
337. Wang, K.; Donnarumma, F.; Baldone, M. D.; Murray, K. K., Infrared laser ablation and capture of enzymes with conserved activity. *Anal. Chim. Acta* **2018**, *1027*, 41-46.
338. Wang, K.; Donnarumma, F.; Herke, S. W.; Herke, P. F.; Murray, K. K., Infrared laser ablation sample transfer of tissue DNA for genomic analysis. *Anal. Bioanal. Chem.* **2017**, *409*, 4119-4126.

339. Terada, M.; Seki, M.; Higashibata, A.; Yamada, S.; Takahashi, R.; Majima, H. J.; Yamazaki, T.; Watanabe-Asaka, T.; Niihori, M.; Mukai, C., Genetic analysis of the human hair roots as a tool for spaceflight experiments. *Adv. Biosci. Biotechnol.* **2013**, *4*, 75-88.
340. Lindahl, T., The intrinsic fragility of DNA (Nobel Lecture). *Angew. Chem. Int. Ed.* **2016**, *55*, 8528-8534.
341. Becker, C.; Hammerle-Fickinger, A.; Riedmaier, I.; Pfaffl, M., mRNA and microRNA quality control for RT-qPCR analysis. *Methods* **2010**, *50*, 237-243.
342. Bevilacqua, C.; Makhzami, S.; Helbling, J.-C.; Defrenaix, P.; Martin, P., Maintaining RNA integrity in a homogeneous population of mammary epithelial cells isolated by Laser Capture Microdissection. *BMC Cell Biol.* **2010**, *11*, 95.
343. Yee, J. Y.; Limenta, L. M. G.; Rogers, K.; Rogers, S. M.; Tay, V. S.; Lee, E. J., Ensuring good quality RNA for quantitative real-time PCR isolated from renal proximal tubular cells using laser capture microdissection. *BMC Res. Notes* **2014**, *7*, 62.
344. Hitzemann, R.; Bottomly, D.; Darakjian, P.; Walter, N.; Iancu, O.; Searles, R.; Wilmot, B.; McWeeney, S., Genes, behavior and next - generation RNA sequencing. *Genes, Brain and Behavior* **2013**, *12*, 1-12.
345. Butler, A. E.; Matveyenko, A. V.; Kirakossian, D.; Park, J.; Gurlo, T.; Butler, P. C., Recovery of high-quality RNA from laser capture microdissected human and rodent pancreas. *J. Histotechnol.* **2016**, *39*, 59-65.
346. Chandley, M. J.; Szebeni, A.; Szebeni, K.; Crawford, J. D.; Stockmeier, C. A.; Turecki, G.; Kostrzewa, R. M.; Ordway, G. A., Elevated gene expression of glutamate receptors in noradrenergic neurons from the locus coeruleus in major depression. *Int. J. Neuropsychopharmacol.* **2014**, *17*, 1569-1578.
347. Jenner, F.; van Osch, G.; Cleary, M.; Ribitsch, I.; Sauer, U.; van Weeren, R.; Brama, P., Laser capture microdissection of murine interzone cells: layer selection and prediction of RNA yield. *J. Stem Cell. Res. Ther* **2014**, *4*, 183-188.
348. Boone, D. R.; Micci, M.-A.; Tagliatela, I. G.; Hellmich, J. L.; Weisz, H. A.; Bi, M.; Prough, D. S.; DeWitt, D. S.; Hellmich, H. L., Pathway-focused PCR array profiling of enriched populations of laser capture microdissected hippocampal cells after traumatic brain injury. *PLoS One* **2015**, *10*, e0127287.
349. Mazurek, N.; Frisk, A.-L.; Beekman, J. M.; Hartwig, A.; Meyer, K., Comparison of progesterin transcriptional profiles in rat mammary gland using Laser Capture Microdissection and whole tissue-sampling. *Exp. Toxicol. Pathol.* **2013**, *65*, 949-960.
350. Braun, A.; Martinez, C.; Schmitteckert, S.; Röth, R.; Lasitschka, F.; Niesler, B., Site-specific gene expression analysis from archived human intestine samples combining laser - capture

microdissection and multiplexed color - coded probes. *Neurogastroenterol. Motil.* **2018**, *30*, e13261.

351. Bojmar, L.; Karlsson, E.; Ellegård, S.; Olsson, H.; Björnsson, B.; Hallböök, O.; Larsson, M.; Stål, O.; Sandström, P., The role of microRNA-200 in progression of human colorectal and breast cancer. *PLoS One* **2013**, *8*, e84815.

352. Gautam, V.; Singh, A.; Singh, S.; Sarkar, A. K., An efficient LCM-based method for tissue specific expression analysis of genes and miRNAs. *Sci. Rep.* **2016**, *6*, 21577.

353. Seelan, R. S.; Warner, D. R.; Mukhopadhyay, P. M.; Andres, S. A.; Smolenkova, I. A.; Wittliff, J. L.; Pisano, M. M.; Greene, R. M., Epigenetic analysis of laser capture microdissected fetal epithelia. *Anal. Biochem.* **2013**, *442*, 68-74.

## APPENDIX. LETTERS OF PERMISSION

Dear kelin wang,

Thank you for placing your order through Copyright Clearance Center's RightsLink® service.

### Order Summary

Licensee: 4445 Alvin Dark  
Order Date: Feb 17, 2019  
Order Number: 4531680375983  
Publication: Analytical and Bioanalytical Chemistry  
Title: Infrared laser ablation sample transfer of tissue DNA for genomic analysis  
Type of Use: Thesis/Dissertation  
Order Ref: 1  
Order Total: 0.00 USD

View or print complete [details](#) of your order and the publisher's terms and conditions.

Sincerely,

Copyright Clearance Center

Home Account Info Help 



**Title:** Infrared laser ablation and capture of enzymes with conserved activity  
**Author:** Kelin Wang, Fabrizio Donnarumma, Matthew D. Baldone, Kermit K. Murray  
**Publication:** Analytica Chimica Acta  
**Publisher:** Elsevier  
**Date:** 16 October 2018  
© 2018 Elsevier B.V. All rights reserved.

Logged in as:  
kelin wang  
LOGOUT

Please note that, as the author of this Elsevier article, you retain the right to include it in a thesis or dissertation, provided it is not published commercially. Permission is not required, but please ensure that you reference the journal as the original source. For more information on this and on your other retained rights, please visit: <https://www.elsevier.com/about/our-business/policies/copyright#Author-rights>

BACK CLOSE WINDOW

Copyright © 2019 Copyright Clearance Center, Inc. All Rights Reserved. [Privacy statement](#). [Terms and Conditions](#).  
Comments? We would like to hear from you. E-mail us at [customercare@copyright.com](mailto:customercare@copyright.com)



**Title:** RNA Sampling from Tissue Sections using Infrared Laser Ablation

**Author:** Kelin Wang, Fabrizio Donnarumma, Scott W. Herke, Chao Dong, Patrick F. Herke, Kermit K. Murray

**Publication:** Analytica Chimica Acta

**Publisher:** Elsevier

**Date:** Available online 7 March 2019

© 2019 Elsevier B.V. All rights reserved.

Logged in as:

kelin wang

Account #:  
3001407877

LOGOUT

Please note that, as the author of this Elsevier article, you retain the right to include it in a thesis or dissertation, provided it is not published commercially. Permission is not required, but please ensure that you reference the journal as the original source. For more information on this and on your other retained rights, please visit: <https://www.elsevier.com/about/our-business/policies/copyright#Author-rights>

BACK

CLOSE WINDOW

Copyright © 2019 [Copyright Clearance Center, Inc.](#) All Rights Reserved. [Privacy statement](#). [Terms and Conditions](#).  
Comments? We would like to hear from you. E-mail us at [customer-care@copyright.com](mailto:customer-care@copyright.com)

## VITA

Kelin Wang was born in Fushun, China in 1986. She received a Bachelor of Engineering in Liaoning University of Petroleum and Chemical Technology, majored in Applied Chemistry. After that, she decided to start her graduate study in USA. She received a Master of Science degree in Western Kentucky University (WKU) under supervision of Wei-ping Pan in 2012. At WKU, she conducted independently on USDA project “Fate of Mercury in Flue Gas Desulfurization Amended Soil”. She also received an average of 4.0 GPA for all the lessons and got a publication from a peer-reviewed journal. Additionally, she performed routine analytical analysis and assisted lab manager with report preparation for outside vendors in Institute for Combustion Science. In Aug. 2013, driven by her interest in biomolecules analysis by mass spectrometry, she joined Dr. Kermit K. Murray’s group in Chemistry department of Louisiana State University (LSU). During her PhD program, she has published two first-author papers and has two other first-author manuscripts in preparation for publishing. She also received Robinson Award in Analytical Chemistry at LSU. Ms. Wang is currently a candidate of Doctor of Philosophy in chemistry, which is planned to be awarded at the Spring 2019 Commencement.